Preparation, Structure and Properties of New Ternary Chalcogenides and Germanides of the Metals from the First Transition Series, Cr, Mn, Fe and Ni

DISSERTATION

zur Erlangung des Grades eines Doktors

der Naturwissenschaften

vorgelegt von

Dipl. Ing. – Chem. Krasimir Aleksandrov

geb. am 03.12.1975 in Vratsa

eingereicht beim Fachbereich 8

der Universität Siegen

Siegen 2005

Acknowledgements

Contents

1 Introduction

The huge demand for new materials in the dawn of the third millennium provides a great challenge for solid state chemistry. Investigating the structure – property relationship is a discipline which has an immense capacity for the development of ultimately new materials or materials with special combination of properties.

One group of compounds which is able to meet many needs of modern technology is the one of the metals from the first transition series, Cr, Mn, Fe and Ni. Known for centuries, in the form of pure metals, different alloys and chemical compounds with many elements from the periodic table they have multiple applications in all spheres of our life. It is by far enough to mention iron only, which gave a name to a whole age of the human history, the steel importance for the industry of our time and the ferrites, without which contemporary computer technology and electronics are unthinkable.

The wide natural abundance of these metals in the form of different oxides and sulphides has triggered the leading role of the investigations concentrated on the properties of their chalcogenides. They not only deal with the oxides and sulphides, but also with the compounds of the other elements of the VIa group of the periodic system, Se and Te, i. e. selenides and tellurides, respectively. Reacting them with elements belonging to the fourth main group, particularly Ge and Si, results in the formation of a variety of ternary compounds, e. g. silicides and germanides. Their crystal structures, in many cases unique, are responsible for exciting chemical, electrical and magnetic properties with great prospectives. Altogether, it makes the ternary systems *transition metal – IVa group element – chalcogen* of special interest for researchers in chemistry.

In the recent years the so – called nanoscience became very popular. The unusual properties of the nanoparticles determined by their intermediate position between the micro– and macrocosmos led to their wide use in different fields – aeroplane and space industry, magnetic memory, high – strength ceramics, computer and military industry, production of solar cells, dyes and lacquers, luminescent materials, ultra pure elements, new semiconductors, pharmaceuticals, etc.

The applications of different inorganic nanoparticles with a high biocompatibility (mainly phosphates of calcium, which have a chemical content similar or identical to that of human bones and teeth) in the preparation of prosthesis and treatment of a number of bone diseases ensures a promising future for nanotechnology in both biochemistry and medicine.

2 Motivation

Natural olivine ((Fe, Mg)$_2$SiO$_4$) forms a substational part of the earth's mantle [1]. Although the olivine structure family is mainly composed of oxides, it also contains sulphides and selenides and has the general formula of A$_2$BX$_4$ (A = alkaliearth or transition metal, B = Si, Ge, X = O, S, Se). The olivine structure [2] is determined by a hexagonal close packing of X ions in which A ions occupy half of the octahedral sites and B ions an eight of the tetrahedral sites is the less dense modification of the cubic spinel structure. Transition metal compounds with olivine structure are well known for their versatile magnetic behaviour. Sulphides and especially selenides of the transition metals which crystallize in the olivine structure – type are rare and less studied in comparison with the oxides. One of the main targets of this work was to investigate the conditions needed to synthesise new olivine compounds of the transition metals from the first transition series, to determine their crystal structure and to study their thermal and magnetic properties.

Thorough studies in the last 100 years of the ternary transition metal chalcogenophosphates (IV), M$_2$P$_2$Y$_6$ (M = V, Mn, Fe, Co, Ni, Pd, Zn, Cd or Hg, Y = S, Se) showed that despite their great diversity they can be divided into two groups. The sulphides of this class crystallize in the CdCl$_2$ structure – type [3], while the selenides crystallize predominantly in the CdI$_2$ structure – type [3]. Common to both groups are the phosphor pairs which occupy half of the octahedral sites in a cubic close packing of Cl$^-$ ions for the CdCl$_2$ – type or in a hexagonal close packing of I$^-$ ions for the CdI$_2$ – type. Over the years it was found that substituting phosphorous with its neighbours in the periodic table namely Si and Ge was possible. Surprisingly, the transition metal chalcogenides which are isostructural to M$_2$P$_2$Y$_6$ and that contain Si or Ge pairs are represented only by three tellurosilicates [4 – 7] and one tellurogermanate [8] with the formula M$_2$X$_2$Te$_6$ (M = transition metal, X = Si, Ge). Since transition metal selenides of that type are not mentioned in the literature at all it was of great interest to investigate whether the synthesis and characterization of such compounds was possible.

Abrikosov et al. investigated the system Fe – Ge – Te and succeeded in detecting the existence of the first ternary compound in this system [9]. Except for its X – ray powder pattern and some electrical measurements nothing else about this compound is reported. The fact that Fe$_3$GeTe$_2$ is the first ternary compound in the Fe – Ge – Te system provoked great interest in studying its crystal structure and properties. The close chemical behaviour of Fe and Ni presumes that if a ternary compound in the system Ni – Ge – Te exists, it could be the

Ni analogue of Fe_3GeTe_2, e. g. Ni_3GeTe_2. Till now knowledge of this system did not extend beyond binary compounds, and such the challenge of synthesising the first ternary compound, to describe its crystal structure and to study its properties was enormous.

In the recent years, nanotechnology found wide use in medicine through the application of artificially synthesised nanoparticles of various calcium phosphates, as materials for preparation of bone- and teeth prosthesis. Because almost all of the reported methods of the synthesis of hydroxylapatite $(Ca_{10}(PO_4)_6(OH)_2)$, which has one of the highest biocompatibilities with human bones and teeth are relatively complicated, as they include many intermediate stages and use different organic subsatnces as size degenerators, the idea of finding a simple synthesis route for nanosize hydroxylapatite particles was of interest.

3 Experimental

3.1 Preparation procedure

For the preparation of the samples, the pure elements were mixed in an agate mortar. Then the prepared mixtures were filled in quartz glass ampoules, which subsequently were evacuated and sealed. The stoichiometric calculations for the educt blends were performed in such a way, that their total weight was between one and two grams.

The heating and cooling of the samples was accomplished in tube furnaces. The temperature was measured using Pt –Pt/Rh – thermocouples and was adjusted with the help of an appropriate control unit. To prevent any eventual separation of the educts as a result of competition between the main reaction, and the transport or sublimation reactions during the heating period, the length of the quartz ampoules was kept as short as possible. The ampoules were heated between 2 and 3 weeks in the temperature range of 600 – 800°C. The exact preparation procedure for each compound is described in the respective contributing chapter.

Nanoscale particles of hydroxyapatite were obtained via titration of aqueous solutions of $CaCl_2 \cdot 2H_2O$ with aqueous solutions of $(NH_4)_2HPO_4$. The concentrations of the solutions for both of the educts were 1 g/l, 2 g/l and 3 g/l. All possible combinations between these concentrations were investigated. The calcination of the samples was realized in a standard tube oven at 650°C, by annealing for six hours.

For all of the implemented syntheses, educts with a high purity were used. The specifications of the commercially available educts are listed in Table 3.1.

Table 3.1: Specifications of the educts used

Element/Compound	Form	Producer	Purity
$CaCl_2 \cdot 2H_2O$	Powder	Merck	99.5%
Chromium	Powder -100 + 325 mesh	Johnson Matthey	99.99%
Germanium	Powder 250 µm	Chempur	99.99%
Iron	Powder	Heraeus	99.9%
Manganese	Powder	Merck	99.5%

Table 3.1 *(continued)*

Element/Compound	Form	Producer	Purity
$(NH_4)_2HPO_4$	Powder	Chempur	> 98%
Nickel	Powder < 100 mesh	Heraeus	99.9%
Selenium	Granules 2 – 4 mm	Heraeus	99.999%
Selenium	Powder < 150 μm	Merck	99.5%
Tellurium	Pieces, low oxygen	Chempur	99.999%

3.2 Vacuum technique

In order to prevent reactions between the starting educt mixtures and air, the quartz glass ampoules were evacuated until the pressure of $5 \cdot 10^{-5}$ mbar inside the ampoule was reached.

3.2.1 Vacuum system outline

The evacuation of the quartz glass ampoules was carried out with the help of the vacuum system shown in Fig. 3.1.
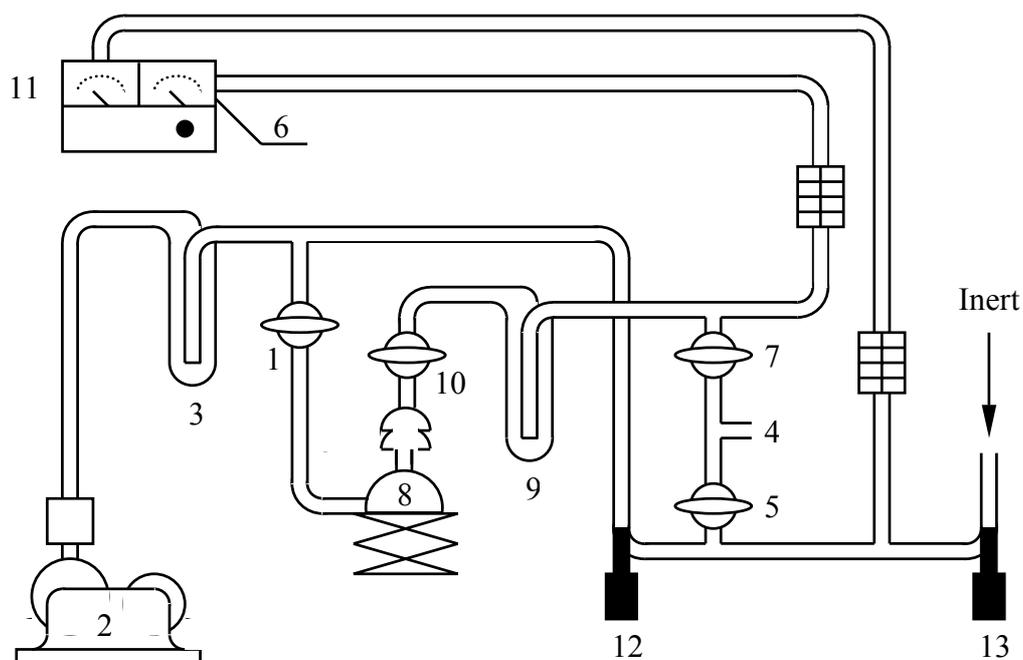
Fig. 3.1: Principle scheme of the vacuum device used for ampoule evacuation

The constituent parts of the system are as follows:

1. *Hollow – plug stopcock*: ensures exhaustion of the gases sucked by the oil – diffusion pump. It consists of a hollow plug and barrel. In order to obtain leak – free seal, the plug and the barrel must be greased.

2. *Oil pump*: it is used for attaining low vacuum (pressure 0.1 mbar) in the system. It employs a rotor which revolves inside a cylindrical stator. The seal between the rotor and stator is obtained by a thin film of oil.

3. *Trap*: prevents contamination of the manifold by accidental loss of oil from the oil pump.

4. *Ampoule outlet*: serves for mounting the quartz glass ampoule which must be evacuated to the vacuum system. The ampoule is mounted to the device via a high – pressure stopcock.

5. *Hollow –plug stopcock*: connects the ampoule to the low vacuum part of the system or the inert gas .

6. *Low – vacuum gauge* : serves for rendering of low vacuum (0,1 mbar) in the manifold.

7. *Hollow – plug stopcock*: connects the quartz glass ampoule with the high vacuum part of the system.

8. *Oil – diffusion pump*: provides pressure of $5 \cdot 10^{-5}$ mbar (high vacuum) in the system. During operation, a low – vapour pressure oil is boiled and the resulting vapour is conducted to a nozzle, where the stream of vapour molecules collides with gas molecules which have diffused into the pump from the ampoule being evacuated. As a result of this collision, the gas molecules are turned in the direction of pumping. After condensation the vapour is returned to the boiler.

9. *Trap*: prevents contamination of the oil – diffusion pump by the accidental loss of reactive compounds from the working manifold.

10. *Hollow – plug stopcock*: allows isolation of the oil – diffusion pump if it is necessary.

11. *High – vacuum gauge*: indicates the attainment of high vacuum (pressure $5 \cdot 10^{-5}$ mbar) within the system.

12. *Needle valve*: disconnects the oil pump from the vacuum manifold. It consists of partially Teflon – covered stem that sits in a glass body. The upper part of the stem is made leak – tight by one or more O – rings.

13. *Needle valve*: ensures flood of the system with inert gas (Argon 99.998%).

A photographic image of the above described vacuum system is presented in Fig. 3.2.

Fig. 3.2: Photo of the vacuum manifold used for ampoule evacuation

3.2.2 Evacuation procedure

Each ampoule is evacuated in two steps. First, preliminary evacuation is performed until a low vacuum (pressure 0.1 mbar) inside the ampoule is achieved. This is followed by evacuation until a high vacuum (pressure of $5 \cdot 10^{-5}$ mbar) is reached.

Before starting the ampoule evacuation, stopcock 1 must be closed. Trap 3 is situated between the oil pump and the main vacuum manifold. The ampoule with the sample inside is mounted to the vacuum system at 4, followed by opening stopcock 5. After rendering a pressure of 0.1 mbar (low vacuum) which is detected by gauge 6, stopcock 5 is closed. Simultaneously stopcocks 1 and 7 are opened. Trap 9 is situated between the oil – diffusion pump 8 and the main vacuum manifold. After approximately 5 minutes, the pressure gauge 11 indicates

pressure of $5 \cdot 10^{-5}$ mbar, i. e. a high vacuum is reached. Closing the ampoule separating tap and stopcock 7 are the final steps of the evacuation process.

In spite of repeated evacuations and floodings of the reaction ampoule with inert gas, a residue of small traces of oxygen and humidity causing unwanted reactions at higher temperatures may still remain. In order to avoid this before starting the evacuation procedure, the vacuum system and the quartz ampoule connected to it must be flushed with inert gas (argon). This is achieved by closing needle valve 12 followed by opening needle valve 13.

3.3 X – ray characterization methods

3.3.1 Introduction

One of the most useful methods for characterizing crystalline materials and determining their crystal structures is X – ray diffraction. X – rays occur in the electromagnetic spectra between γ – rays and ultraviolet and their wavelength is around 1Å (10^{-10} m). X – rays are generated when electrons accelerated through a high voltage strike a metal target. In colliding with the target, the electrons suffer a loss of energy and part of the energy lost is emitted in the form of X – rays. This process gives rise to "white radiation" X – rays with wavelengths varying in certain range.

For the diffraction experiment monochromatic X – rays are needed. If the electrons are accelerated through, say, 30 kV, they have sufficient energy to excite some of the inner shell electrons (K shell electrons) of the target material (Cu, Mo, Ag, Cr, Fe). Immediately an electron from an outer shell fills the vacancy. This transition causes the emission of nearly monochromatic, high intensity radiation, characteristic of the respective electronic transition in the target material (Cu K_{α}: 1.5405 Å). To separate the monochromatic X – rays from the rest, a crystal monochromator consisting of a large single crystal (e. g. germanium) is used.

Ordered crystals are able to diffract radiation with a wavelength comparable to the interatomic distances in the crystal (~ 1Å). In order to explain diffraction by crystals, Bragg regarded them as build of lattice planes (set of parallel planes passing through lattice points) with each plane acting as a semitransparent mirror. When a crystal is irradiated with X – rays, a fraction

of the radiation is reflected by the plane at an angle equal to the angle of incidence. The rest is transmitted to the next plane where it is subsequently reflected and so on (Fig. 3.3).
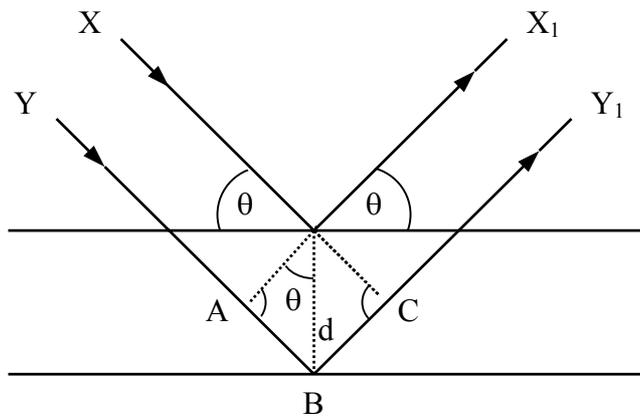
Fig. 3.3: Graphical representation of Bragg's law for X – ray diffraction by real crystals

The beams XX_1 and YY_1 are reflected by adjacent planes. Positive interference (diffraction) occurs only if the reflected beams X_1 and Y_1 are in phase. The condition for diffraction is fulfilled if the distance ABC (optical path difference) is equal to $n\lambda$ (n: integer). The distance between the planes – *d – spacing* and the angle of incidence θ are related to AB by the equation:

$$AB = d \cdot sin\theta$$
$$BC = d \cdot sin\theta$$

Thus
$$AB + BC = 2d \cdot sin\theta$$

But
$$AB + BC = n \cdot \lambda \qquad \text{where } n \text{ is integer}$$

Therefore
$$2d \cdot sin\theta = n \cdot \lambda \qquad \text{Bragg's law}$$

Bragg's law strictly defines the condition at which diffraction in real crystals may occur. A similar result is obtained if the X – ray diffraction is treated in the framework of the *"Laue – equations"* [3, 10 – 12].

3.3.2 Powder X – ray methods

X – ray powder investigations were carried out with the diffractometer D 5000 (Siemens, Karlsruhe), modified Debye – Sherrer transmission geometry (Fig. 3.4). The diffractometer is equipped with a germanium monochromator (type Johanson, lattice plane [111]), which provides a focused, monochromatic X – ray beam. Diffracted X – rays are detected with a position sensitive detector (PSD) 50M (MBraun, Garching). Standard measurements of crystalline samples were carried out in the 2θ – range from 5 to 90° with step size 0,015°. Each sample was prepared in the form of a thin film, which is mounted onto a rotating holder. The applied measurement period is 30 minutes (for phase analysis), and up to 10 hours (for all refinements).
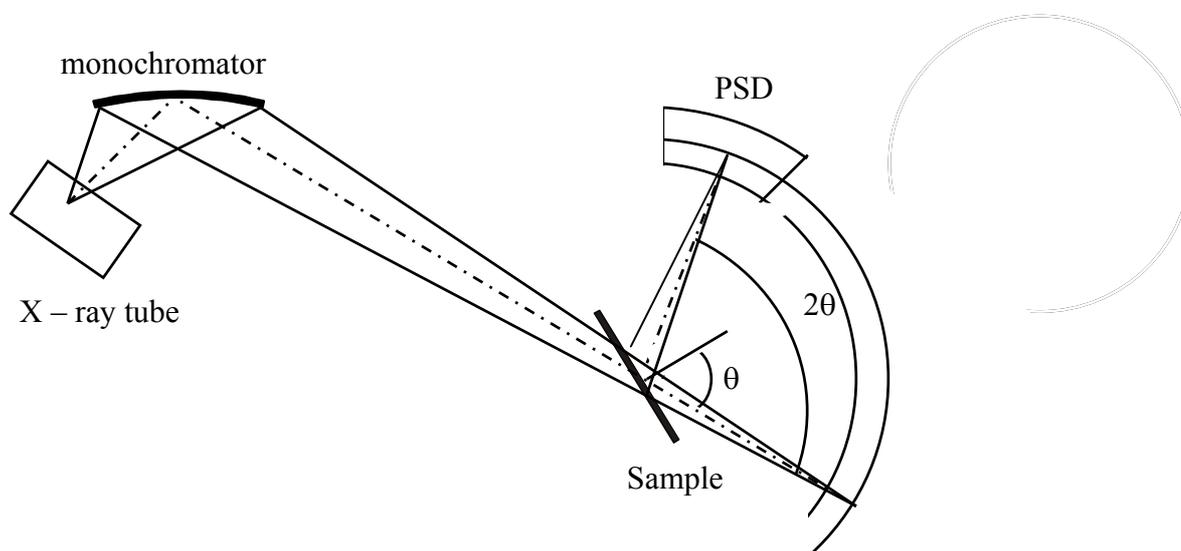
Fig. 3.4: Schematic representation of powder diffraction system D5000

To determine possible phase transformations at high temperatures, a STADI P powder diffractometer (STOE, Darmstadt), with germanium monochromator was used. The samples were filled in quartz glass capillaries. After evacuating and sealing the capillaries, they were measured at different temperatures.

To interpret the measured powder patterns the program WinXPOW (STOE, Darmstadt) was used. This program packet ebnables graphical representations, peak search, profile adjustment and indexing (Werner's, Visser's and Louer' algorithm) of the powder patterns [13].

3.3.3 Single crystal X – ray structure analysis

X – ray single crystal measurements were carried out with the STOE – IPDS (**I**maging **P**late **D**iffraction **S**ystem), with Mo K_α radiation and a graphite monochromator. X – ray crystallography with single crystals is based on a mathematical formalism much more demanding than Bragg's equation [3]. The use of commercial systems, however, does not require the full knowledge of the complete mathematical formalism, but can be used widely as "black box", in particular in "routine structure analysis".

In this work, data collection and evaluation were carried out with the IPDS program packet [14]. Absorption correction, structure solution and refinement of the structures was carried out with the help of the following programs X – prep [15], X – red [16], X – shape [17], SHELXS – 97 [18], and SHELXL – 97 [19].

The visual representation of the structures was carried out using the program DIAMOND [20].

3.4 Thermal analysis

The melting behaviour of the synthesised compounds was ascertained by **D**ifferential **T**hermal **A**nalyses (DTA L – 62, Linseis, Selb). The samples (30 – 50 mg) were filled in small quartz glass ampoules, which subsequently were evacuated, sealed and mounted on the sample holder of the DTA – device. The heating of the samples was carried out in the temperature range 20 – 1000°C with a heating rate of 10°C/min. Al_2O_3 was used as a reference substance. The evaluation of the obtained peaks was achieved by determining the onset temperature with the help of a program called: Linseis Data evaluation [21], which is available for Windows.

3.5 Scanning electron microscopy

For the topological and analytical examination of microcrystalline samples a scanning electron microscope (type CS 44 SEM, CamScan, Cambridge, UK) is available. For qualitative and quantitative analyse the integrated EDX – system (**E**nergy **D**ispersive **X** – ray spectroscopy), type DS – 701 EDAX, Cambridge, UK and WDX – system was used

(**W**avelength **D**ispersive **X** – ray spectroscopy), type WDX – 3PC Microspec, Freemont, USA).

During the EDX – experiment all wavelengths of the measuring range are simultaneously detected, while with the WDX – experiment the intensity of the individual wavelengths are recorded sequentially.

3.6 Infrared spectroscopy

The identification of nanoscale particles of hydroxylapatite was carried out with IR spectroscopy. IR spectroscopy is based on the vibration of atoms in molecules or solids. These vibrations have frequencies in the range $10^{12} - 3 \cdot 10^{14}$ Hz, i. e. in the frequency range of IR radiation [22]. In practice instead of the frequency for description of this vibrations is adopted the *wave number* – $\tilde{v}$, which is connected with the frequency via the expression:

$$\tilde{v} = \frac{v}{c} = \frac{1}{\lambda} \; / \; cm^{-1}$$

Where v is the frequency, c is the speed of light and λ is the wavelength.

IR spectra are widely used for the identification of specific functional groups. In inorganic solids, covalently bonded units such as hydroxyl groups, crystal water and oxyanions – phosphate, carbonate, nitrate, sulphate, etc. give rise to intense IR peaks. Vibration modes of covalently bonded groups (oxyanions), give peaks which occur at relative high frequencies. Since inorganic solid compounds give characteristic vibration spectra this can be used to identify and determine the purity of the compounds.

The infrared spectra of the nanoscale samples of hydroxyapatite were measured with a Fourier – transform spectrometer (IFS 25, Bruker, Karlsruhe). The resolution of the device is 2 cm^{-1}. From each sample pellets with KBr as a filling material were prepared. All the measurements were carried out at room temperature in the middle infrared range (MIR) from 4000 cm^{-1} to 380 cm^{-1}. The evaluation of the measured absorption spectra was attained using the spectroscopic software packet OPUS 2.2 (Bruker, Karlsruhe) [23].

3.7 Magnetic measurement

To characterise the magnetic properties of the newly synthesized compounds a commercial SQUID magnetometer (MPMS, Quantum Design, San Diego, USA) was used.

The magnetometer operates in the temperature range from 2K to 400K and has a sensitivity of $2 \cdot 10^{-8}$ emu. All measurements were performed by Dr. R. Kremer at the Max – Planck – Institute for Solid State Research, Stuttgart.

4 The compound Mn$_2$GeSe$_4$

4.1 Introduction

Compounds of the A$_2$BX$_4$ olivine structure type (A = transition or alkali earth metal, B = Si, Ge, X = O, S, Se) have been of great interest to mineralogists and crystallographers, because of the presence of the mineral olivine in the earth's mantle. The olivine structure consists of a hexagonal close packing of chalcogen atoms in which A atoms occupy half of the octahedral sites and B atoms fill an eighth of the tetrahedra. Their structures and properties have been studied for a long time, as the main subjects of the investigations are the transition metal olivines.

In 1965 Vincent, Bertaut and Qui [24] reported on the crystal structure of Mn$_2$GeS$_4$. Creer and Troup who reported the crystal and magnetic structure of Mn$_2$GeO$_4$ extended the research on the manganese olivines [25]. Fuhrman and Pickardt described the exact crystal structure of Mn$_2$SiS$_4$ in 1989 [26]. Santoro, Newnham and Nomura [27], and Lamarche et al. [28] systematically carried out studies on the magnetic properties of the manganese olivine compounds. All of these compounds are antiferromagnetic at low temperatures, with a spin alignment varying from simple collinear [24], to complex canted antiferro – or ferrimagnetic [25, 27, 28].

Among the transition metal olivines only two selenides: Fe$_2$GeSe$_4$ [29] and Mn$_2$SiSe$_4$ [30], have been mentioned in the literature up to now. As in all compounds with an olivine – type structure, the selenium atoms form a hexagonal close packing in which half of the octahedral sites are occupied by Fe resp. Mn atoms, while the Ge resp. Si atoms occupy 1/8 of the tetrahedra. Their lattice constants are given in Table 4.1.

Table 4.1: Lattice constants of Fe$_2$GeSe$_4$ and Mn$_2$SiSe$_4$

Compound	SG	a / pm	b / pm	c / pm
Mn$_2$SiSe$_4$	*Pnma*	1330.7(8)	777.8(5)	624.5(3)
Fe$_2$GeSe$_4$	*Pnma*	1306.9(1)	755.9(1)	620.4(6)

Bodenan et al.[31] carried out detailed studies of the magnetic properties of Mn_2SiSe_4. It is antiferromagnetic. The neighbouring spins are aligned not exactly antiparallel, but are canted one to another. This leads to a weak magnetic moment and the compound seems to be an intermediate between an antiferromagnet and a ferrimagnet.

In spite the extensive studies on the transition metal olivines, the compound Mn_2GeSe_4 still remains unknown. In this chapter the synthesis, crystal structure and properties of this new member of the olivine family are reported.

4.2 Preparation and properties

Mn_2GeSe_4 was synthesised by a classical solid-state reaction of manganese, germanium and selenium. The pure elements were mixed in stoichiometric proportions (Mn : Ge : Se = 2 : 1 : 4) in an agate mortar for several minutes. The prepared blend was filled in an approximately 5cm long quartz glass ampoule, which subsequently was evacuated, sealed and heated in a furnace at 600°C. The heating was accomplished with a rate of 20°C/h up to the end temperature. After 20 days the furnace was cooled down to room temperature, with a rate of 30°C/h.

The resulting dark grey bulk was homogeneous, formed by metal glimmering crystals, with a polygonal habit (Fig. 4.1). The crystals are water stable and not air sensitive.
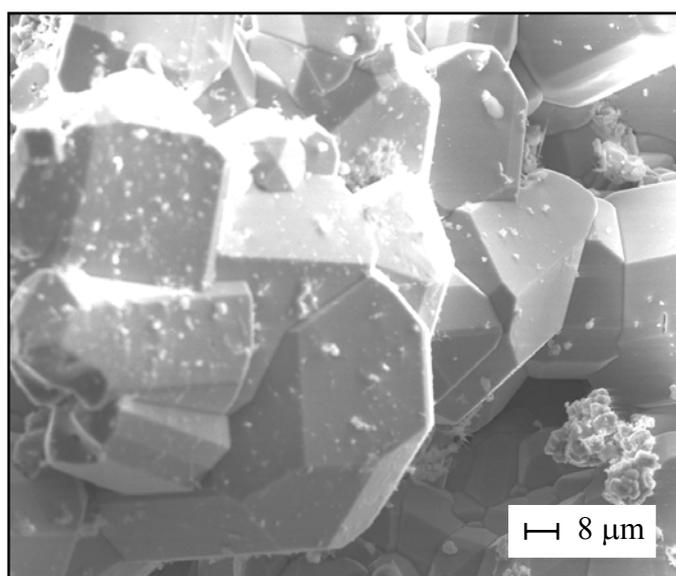
Fig. 4.1: SEM picture of crystals of Mn_2GeSe_4

The melting temperature of 873°C was determined by **D**ifferential **T**hermal **A**nalysis. The DTA curve is represented in Fig. 4.2. Upon cooling two thermal effects at 814°C and 696°C are observed. This suggests that the thermal decomposition of the compound should occur upon heating.
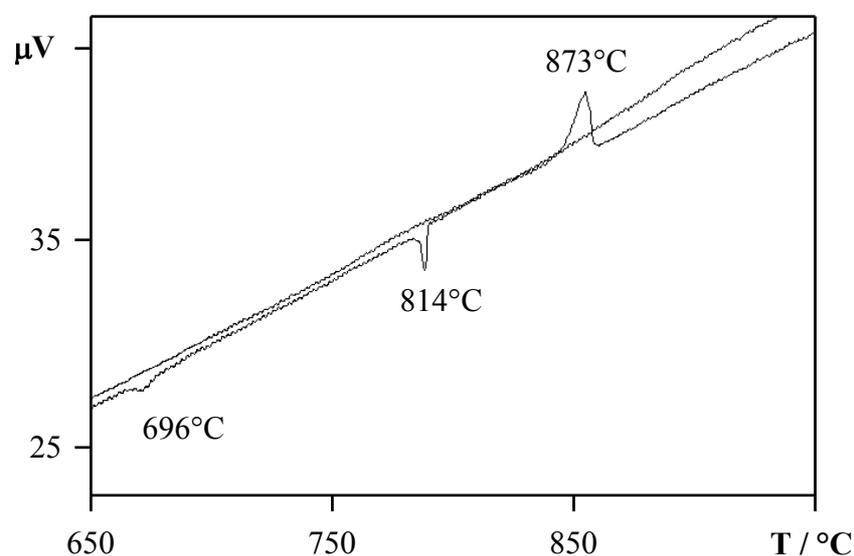
Fig. 4.2: DTA measurement of Mn$_2$GeSe$_4$. The heating curve shows an endothermic effect at 873°C. Upon cooling two exothermic effects are observed

To clarify this problem the substance was investigated after the thermal analysis using X – ray powder diffractometry. In the powder pattern together with the reflections of Mn$_2$GeSe$_4$ some additional reflections are observed (Fig. 4.3). They belong to MnSe and GeSe$_2$, respectively; i. e. by heating Mn$_2$GeSe$_4$ suffers partial decomposition. Thus, the exothermic effect at 814°C observed in the DTA curve has to be the solidification point of Mn$_2$GeSe$_4$. The second exothermic effect observed at 696°C shows the solidification point of GeSe$_2$ (melting point 707°C).

The DTA experiment was carried out up to a temperature of 1000°C. MnSe melts at 1460°C and that is the reason why thermal effects for this compound are not observed in the DTA curve.
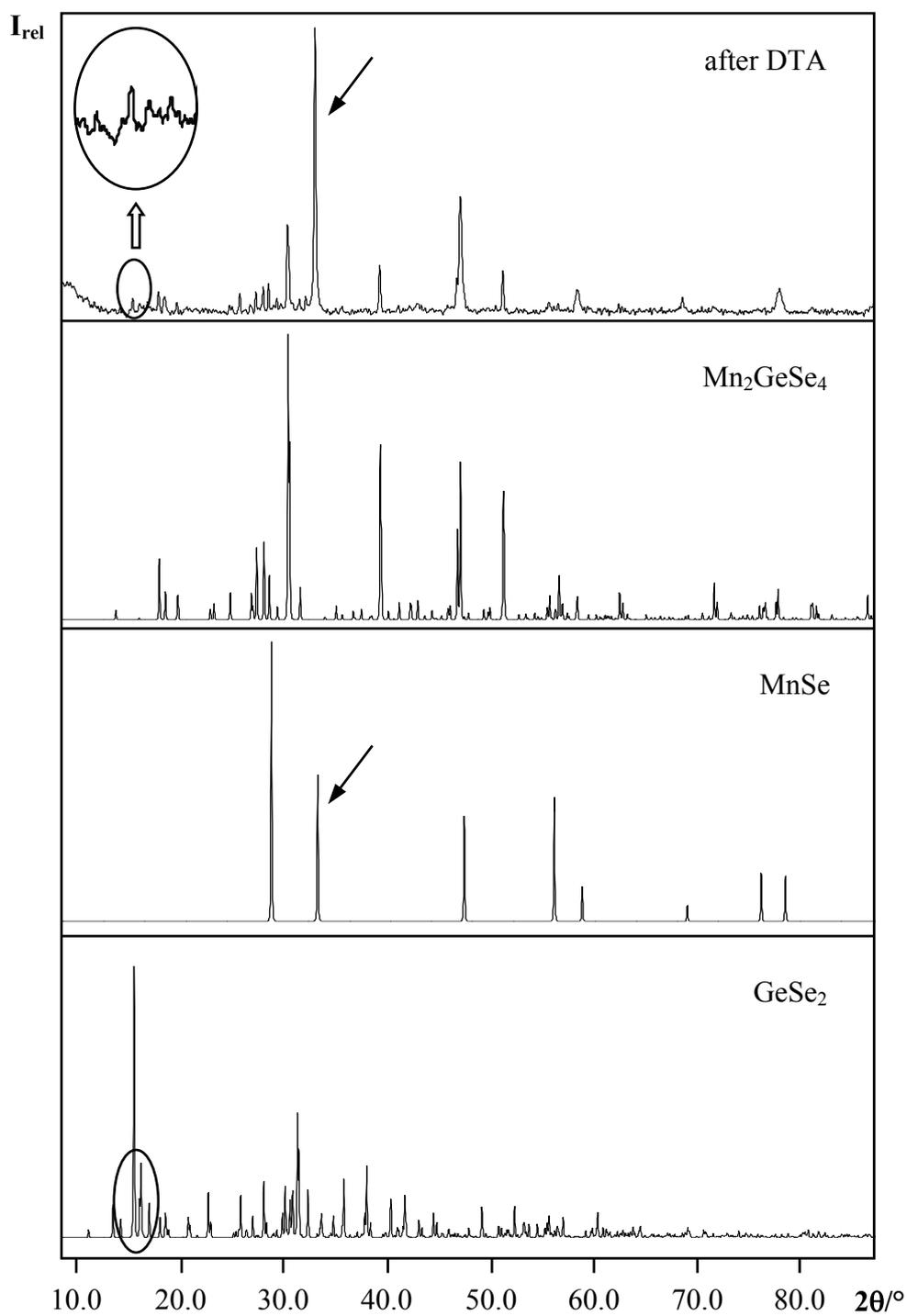
Fig. 4.3: Comparison between the measured powder pattern of "Mn₂GeSe₄" after a DTA experiment (top) and the calculated patterns of Mn₂GeSe₄, MnSe and GeSe₂

4.3 Characterization

The X – ray powder pattern of a powdered sample of Mn_2GeSe_4 is represented in Fig. 4.4. It is in excellent agreement with the pattern calculated on the basis of the lattice constants and atom positions obtained from the structure refinement. No reflections from impurity compounds are observed. The positions of the reflections and their intensities fit excellently.
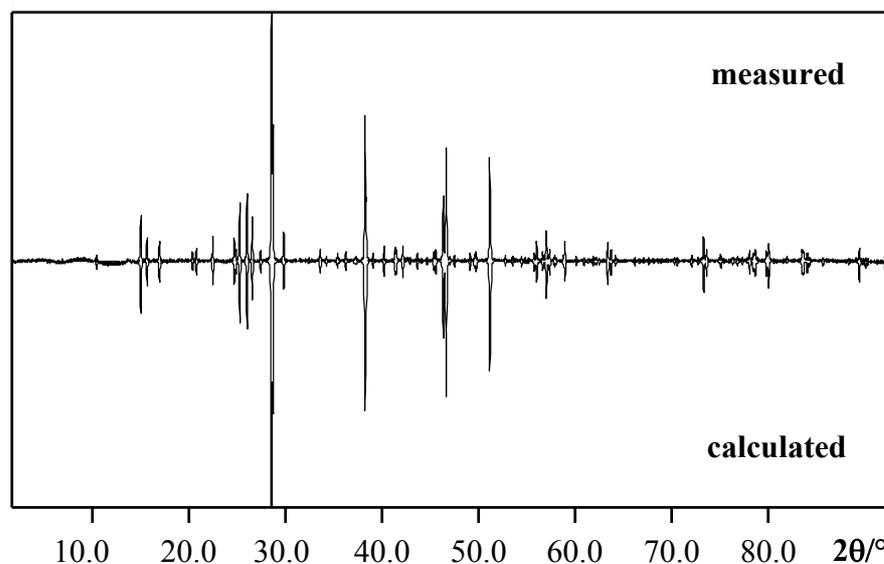
Fig. 4.4: Comparison between the measured powder pattern (top) of Mn_2GeSe_4 and the calculated one (bottom)

Indexing the reflections resulted in an orthorhombic cell. The lattice constants and volume increase in comparison to the one of the isotypic compounds Fe_2GeSe_4 and Mn_2SiSe_4 (Tab. 4.2). A list of the observed reflections for Mn_2GeSe_4 is given in Table 11.1 (see App.).

Table 4.2: Comparison of the lattice constants and volumes of Mn_2SiSe_4, Mn_2GeSe_4 and Fe_2GeSe_4 obtained from powder data

Compound	a / pm	b / pm	c / pm	$V \times 10^6$ / pm^3
Mn_2SiSe_4	1330.7(8)	777.8(5)	624.5(3)	646.4(1)
Mn_2GeSe_4	1339.9(7)	779.5(4)	632.8(3)	661.0(7)
Fe_2GeSe_4	1306.9(1)	755.9(1)	620.4(6)	612.9(2)

The chemical composition of the crystals was additionally analysed using an analytical scanning electron microscope (Fig. 4.5). The EDX – spectra shows no significant difference between the expected and measured stoichiometric proportions (Tab. 4.3).
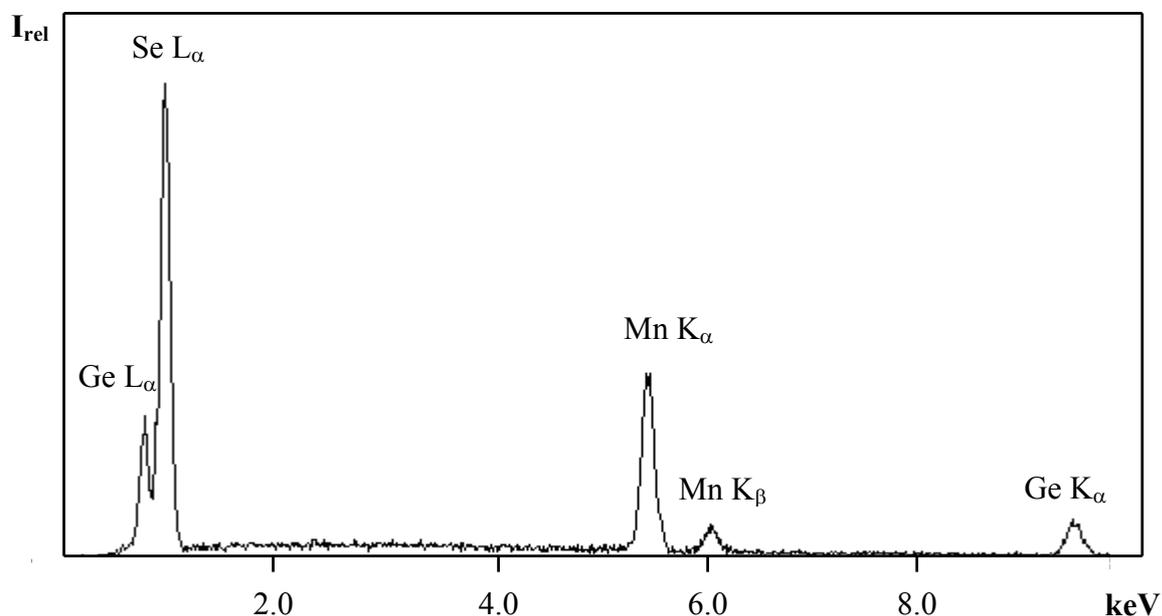
Fig. 4.5: EDX – spectra of Mn₂GeSe₄

Table 4.3: Result of a typical EDX analysis in comparison to the expected values for Mn₂GeSe₄

Element	Measured / atom %	Expected / atom %
Mn	29.46	28.56
Ge	13.89	14.28
Se	56.64	57.12

A possible phase transition of Mn₂GeSe₄ at high temperatures was investigated. The X – ray powder patterns were measured at different temperatures. Fig. 4.6 shows a comparison between the calculated pattern of Mn₂GeSe₄ and the patterns of samples measured at room temperature, 600°C, 700°C and 750°C.
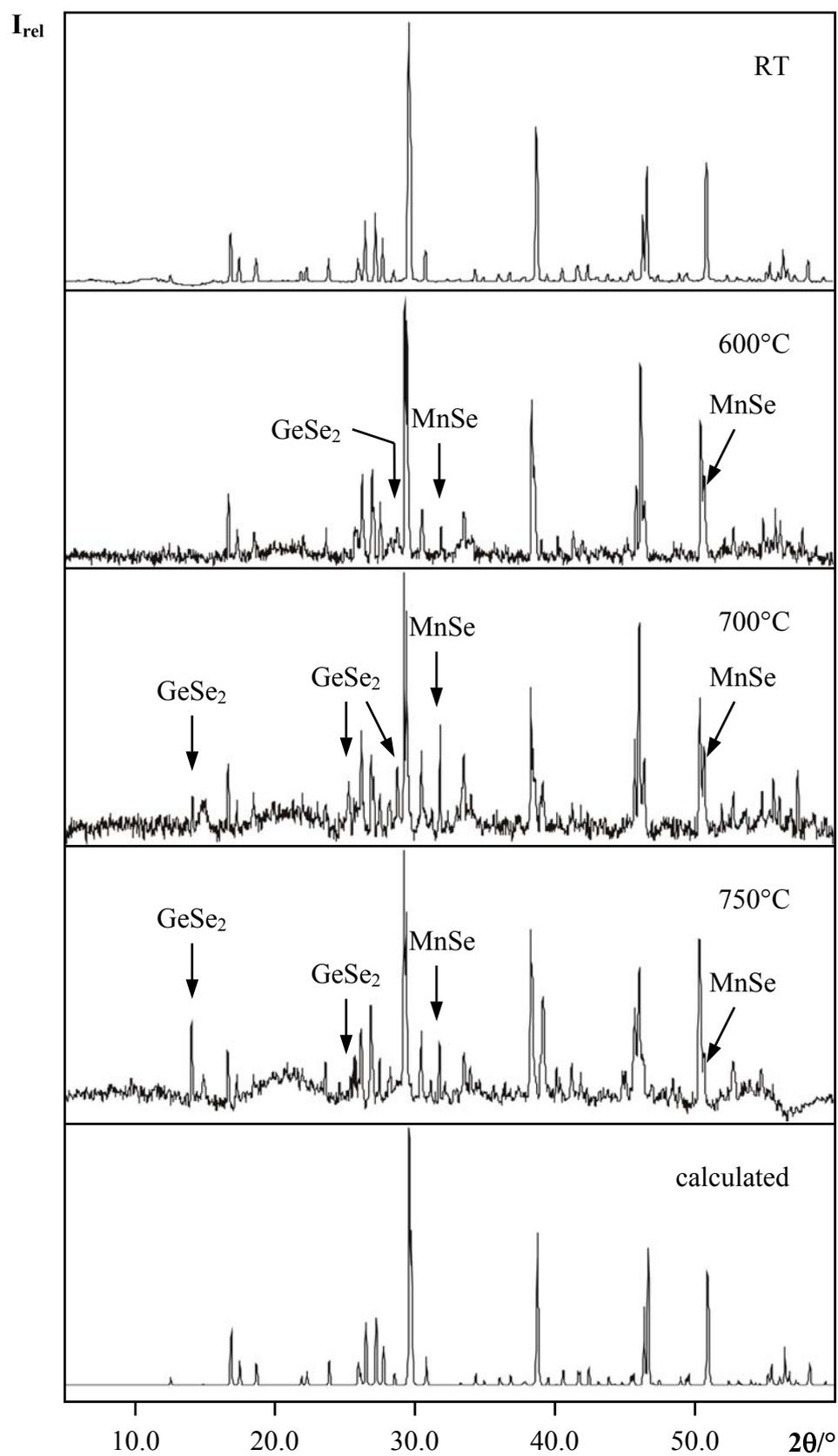
Fig. 4.6: Comparison between the calculated pattern of Mn$_2$GeSe$_4$ and the patterns for different temperatures

The X – ray powder patterns measured at high temperatures are shifted to a lower 2θ angle compared to the pattern measured at room temperature. This is caused by a normal thermal expansion, but not by a phase transition. The increase is significant when the temperature is changed directly from room temperature to 600°C and this explains the relative strong shift in the powder pattern measured at these temperatures. A further increase in the temperature leads to a small change in the lattice constants of Mn_2GeSe_4 and respectively very weak shifts in the powder patterns are observed. Indexing of the patterns proves this fact (Tab. 4.4). The unit cell volume depends almost linear from the temperature (Fig 4.7).

Table 4.4: Comparison between the lattice constants and volumes of Mn_2GeSe_4 obtained by the cell refinement of the powder diffraction data measured at different temperatures

Temperature / °C	a / pm	b / pm	c / pm	$V \times 10^6$ / pm^3
25	1339.89(7)	779.51(4)	632.84(3)	660.97(7)
600	1350.5(4)	786.7(3)	636.8(2)	676.5(5)
700	1353.0(4)	788.4(3)	637.1(2)	679.5(6)
750	1353.8(5)	788.3(3)	637.4(2)	680.2(5)
Δ %	1.03	1.12	0.71	2.87
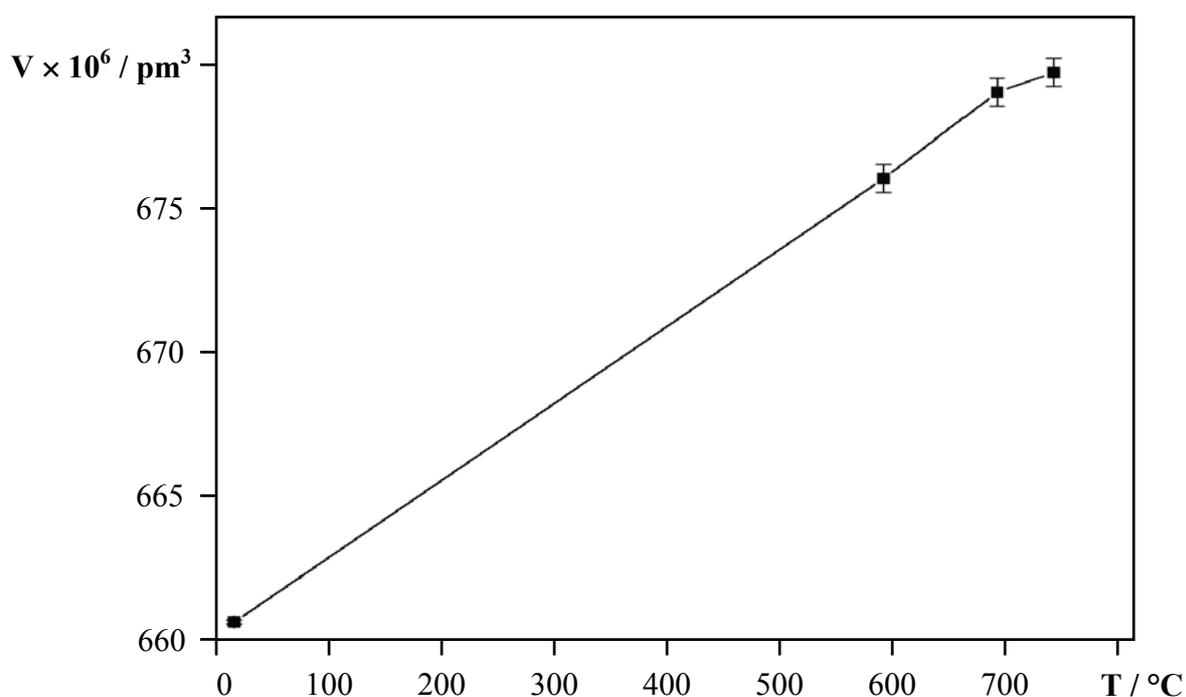
Fig. 4.7: The temperature dependence of Mn_2GeSe_4 unit cell volume

In the patterns measured at high temperatures a "splitting" of some reflections and additional reflections are observed. They are indexed as MnSe and $GeSe_2$, respectively. This implies the beginning of the thermal decomposition still at 600°C (the DTA investigation showed thermal decomposition at about 873°C). Another reason could be the crystallization of MnSe and $GeSe_2$, which were already present, but in an amorphous state. The reflections observed for Mn_2GeSe_4 at 600°C, 700°C and 750°C are given in Tab. 11.2 – 11.4 (see App.).

4.4 Single crystal analysis

For the single crystal analysis, a dark – grey polygonal crystal was selected under a light microscope and fixed on the top of a glass capillary. The most important structure refinement and crystallographic data are summarised in Table 4.5.

Table 4.5: Crystallographic and structure refinement data for Mn_2GeSe_4

Formula	Mn_2GeSe_4
Temperature	293(2) K
Molecular weight	$M = 498.31$ g/mol
Space group	*Pnma* (No. 62)
Cell dimensions	$a = 1335.0(3)$ pm
	$b = 776.5(2)$ pm
	$c = 630.7(1)$ pm
Volume	$V = 653.8(2) \times 10^6$ pm^3
Density (calculated)	$\rho = 5.062$ g/cm^3
Formula units per unit cell	$Z = 4$
Structure solution	SHELXS – 97 [18]
Structure refinement	SHELXL – 97 [19]
Diffractometer	IPDS (Stoe)
Measured θ range	$3.05° \leq \theta \leq 31.62°$
hkl ranges	$-19 \leq h \leq 16$
	$-11 \leq k \leq 10$
	$-9 \leq l \leq 9$
Absorption coefficient	$\mu = 30.505$ mm^{-1}
No. of measured reflections	6097
No. of unique reflections	1172
No. of reflections ($I_0 \geq 2\sigma (I)$)	908
Extinction coefficient	$\varepsilon = 0.00408(5)$
$\Delta\rho_{min}$ / $\Delta\rho_{max}$ / e/pm$^3 \times 10^{-6}$	-1.654 / 1.675
R_1 / wR_2 ($I_0 \geq 2\sigma$ (I))	0.0302 / 0.0771
R_1 / wR_2 (All data)	0.0426 / 0.0828
Goodness – of – Fit on F^2	0.923

The quality factor values after the last refinement cycle are R_1 = 0.0302, respectively wR_2 = 0.0771 (908 reflexes with $I_0 \geq 2\sigma$ (*I*)). The refinement is realized by the "least – squares" method. The positions of the atoms together with the isotropic temperature factors are listed in table 4.6. The anisotropic thermal parameters are given in Table 11.5 in the Appendix.

Table 4.6: Atomic coordinates, Wyckoff notations and isotropic displacement parameters U_{eq}

Atom	Wyck.	*x*	*y*	*z*	$U_{eq} \times 10^4$ / pm^2
Mn1	*4a*	0	0	0	0.0084(1)
Mn2	*4c*	0.26954(4)	¼	0.99516(8)	0.0078(1)
Ge	*4c*	0.08892(3)	¼	0.41079(5)	0.00249(7)
Se1	*4c*	0.09308(3)	¼	0.77812(5)	0.00373(7)
Se2	*4c*	0.92846(2)	¼	0.25331(5)	0.00404(7)
Se3	*8d*	0.16887(2)	0.01459(3)	0.24518(3)	0.00397(5)

The equivalent isotropic atom displacement parameters U_{eq} are calculated as one third of the orthogonal tensors U_{ij}.

4.5 Structure description and discussion

The crystal structure of Mn$_2$GeSe$_4$ can be described as a hexagonal close packing of selenium atoms in which the manganese atoms occupy 1/2 of the octahedral sites, while the germanium atoms occupy 1/8 of the tetrahedral holes. The (MnSe$_6$) octahedra form zigzag chains along [010]. The gap between the chains is occupied by germanium in tetrahedral coordination (Fig. 4.8). The adjacent layers perpendicular to [001] which are formed by similar zigzag chains and (GeSe$_4$) tetrahedra are shifted by ½, 0, ½. According to the olivine structure – type, the MnSe$_6$ octahedra share common edges along [110], [1$\bar{1}$0] and corners along [001]. Such an arrangement of the chalcogen and metal atoms defines two different sites occupied by manganese. Mn1 located at the centre of symmetry (4a) and Mn2 located on a mirror plane perpendicular to [010] (4c). Thus, one edge – sharing octahedra chain along [010] is empty.
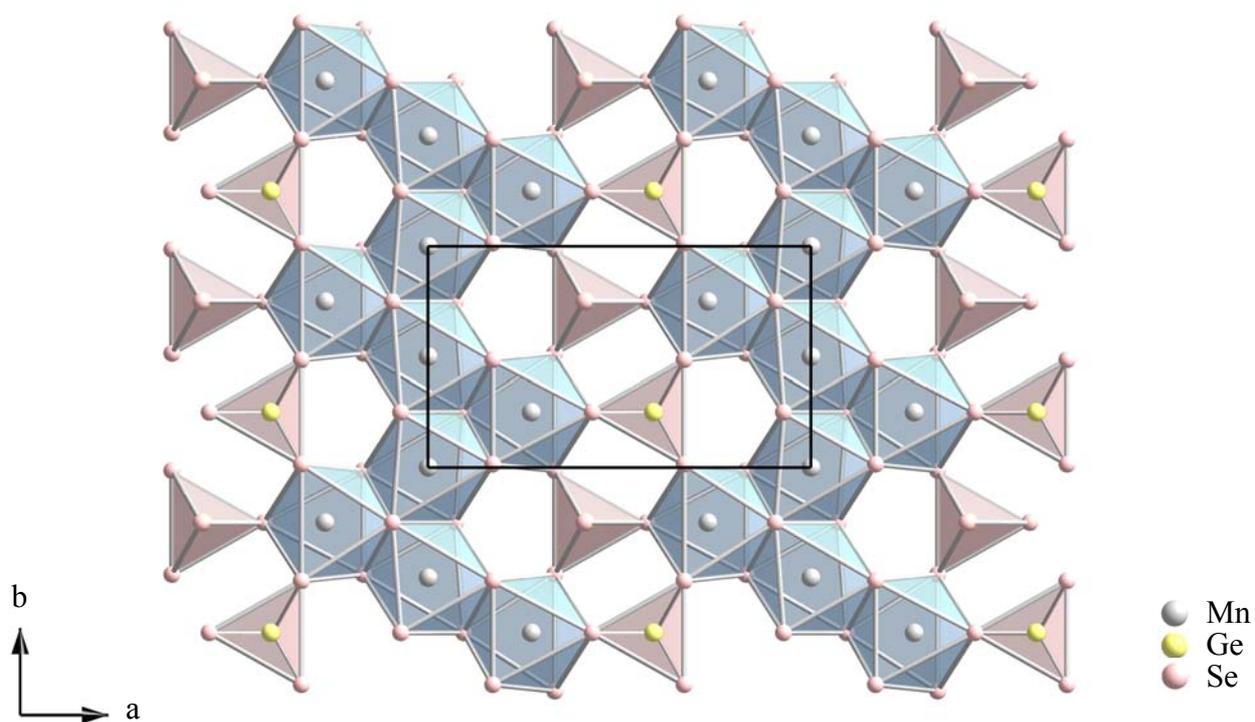
Fig. 4.8: Characteristic section of the Mn₂GeSe₄ structure. (MnSe₆) octahedra form zigzag chains along [010]. The gap between the chains is partially filled with (GeSe₄) tetrahedra

In each layer built of zigzag chains of (MnSe₆) octahedra and (GeSe₄) tetrahedra every Mn1 atom is neighboured to two Mn1 and two Mn2 atoms with two different Mn – Mn distances as shown in Fig. 4.9.

$d_{(Mn1 – Mn1)} = 388.2$ pm
$d_{(Mn1 – Mn2)} = 408.9$ pm
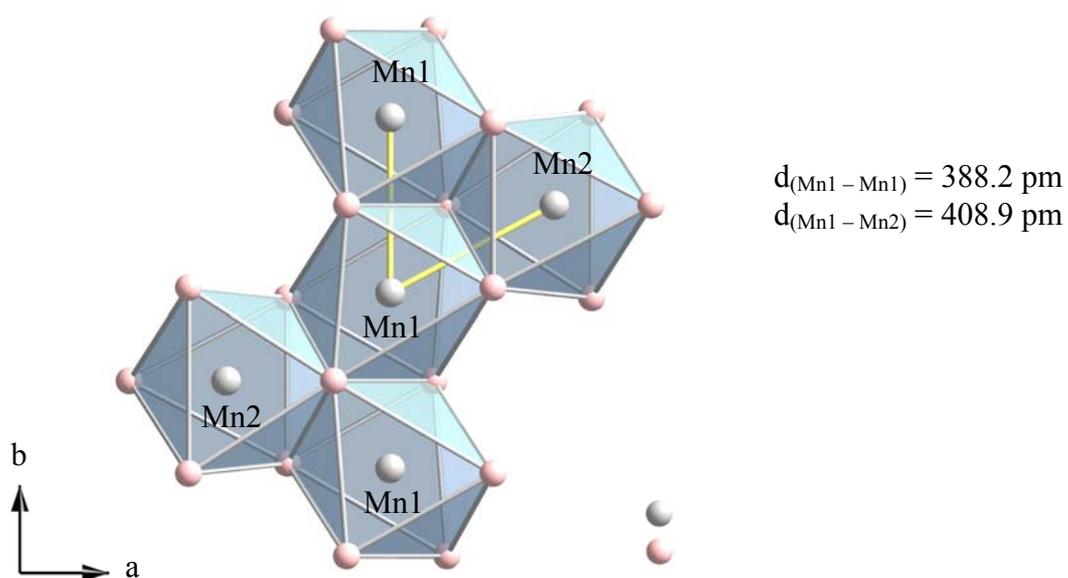
Fig. 4.9: Zigzag chain with two different Mn – Mn distances

The selenium atom common to two Mn1 and one Mn2 octahedra forms one of the apices of a tetrahedron occupied by a germanium atom. The other three corners are located in a horizontal plane and are formed by selenium atoms from the layer below or above. Each Mn1 octahedron shares common edges with two Mn1 and two Mn2 octahedra from the same layer. Additionally, the Mn1 octahedron shares common corners with two Mn2 octahedra and a common edge and corner with two (GeSe₄) tetrahedra from the layer below and above, respectively (Fig. 4.10).
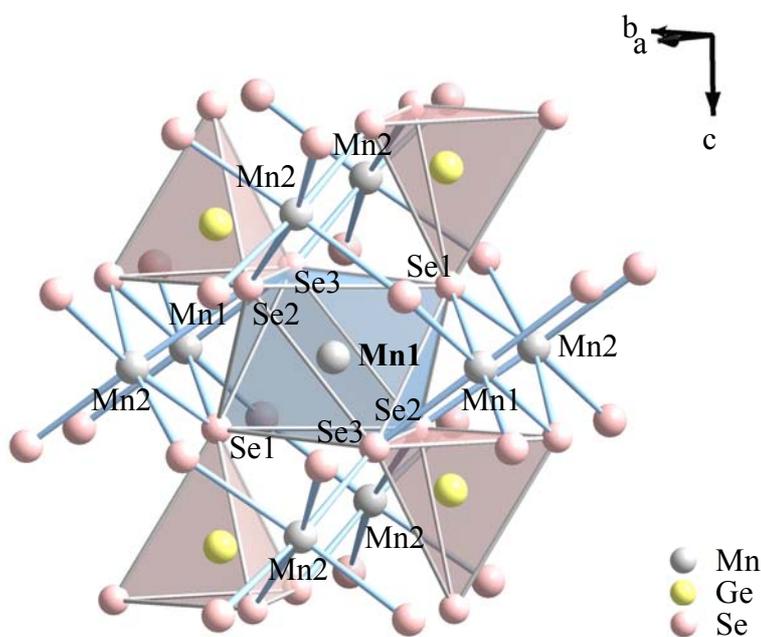
Fig. 4.10: Polyhedral surrounding of Mn1 octahedron

A Mn2 octahedron always shares a common edge with two Mn1 octahedra and common corners with three (GeSe₄) tetrahedra from the same layer. From the layer above, the Mn2 octahedron shares common corners with one (GeSe₄) tetrahedron and with two Mn1 and two Mn2 octahedra. Additionally, it shares a common edge with one (GeSe₄) tetrahedron and common corners with two Mn1 and two Mn2 octahedra from the layer below. This is represented in Fig 4.11.
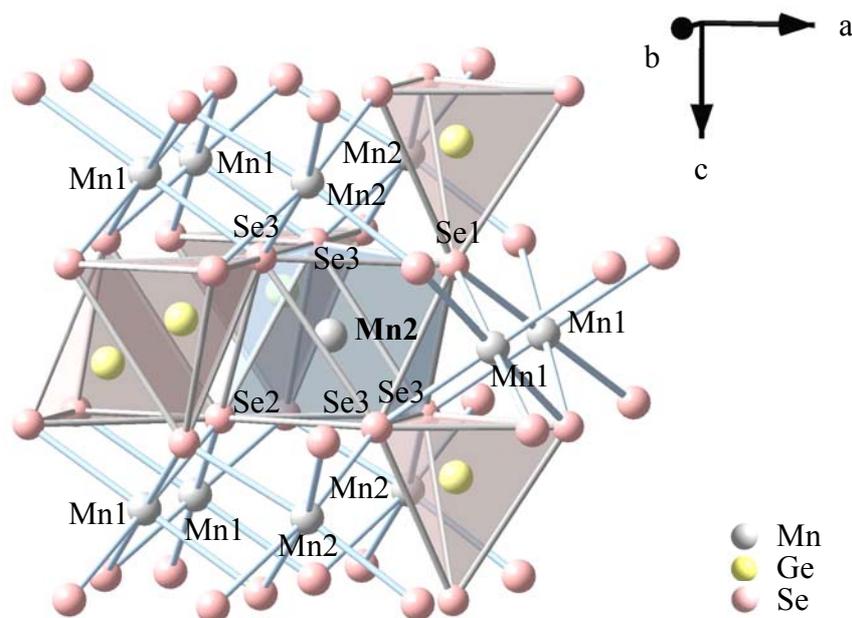
Fig. 4.11: Environment of Mn2 octahedron

In Table 4.7, the interatomic distances and angles of the (MnSe$_6$) and (GeSe$_4$) polyhedra are represented. The Mn – Se distances correspond to the distances reported in the literature [30, 32], but are considerably shorter (Mn – Se distance for Mn1 octahedra is 270.73(5) pm and 272.23(6) pm for Mn2 octahedra, respectively) than one would predict on the basis of the effective ionic radii ($r_{Mn(II)}$ = 83 pm for coordination number 6, $r_{Se(-II)}$ = 198 pm for coordination number 6) [33]. This shortening is probably, caused by the more covalent character of the Mn – Se bonds [34]. Also the Mn2 – Se2 distance (264.91(8) pm), is significantly shorter than the mean value. The shared Se – Se edges (Se1 – Se2, Se1 – Se3, Se2 – Se3 for Mn1 octahedra and Se1 – Se3, Se3 – Se3 for Mn2 octahedra) are significantly shorter than the unshared ones. Their values are in the range of 361.1(0) pm to 371.6(0) pm for the Mn1 octahedra and from 361.1(0) pm to 365.6(1) pm for the Mn2 octahedra. The unshared Se – Se edges are between 389.8(1) pm and 405.9(1) pm for the Mn1 octahedra, and between 379.0(1) pm and 410.9(1) pm for the Mn2 octahedra, respectively. Considering also the Se – Mn – Se angles the smaller distortion of the Mn1 octahedra compared to that of Mn2 is obvious (Fig. 4.12). This corresponds well with the fact that Mn1 is at the centre of symmetry, and thus the stress field on it is more uniform.

Table 4.7: Interatomic distances / pm and angles / ° in Mn_2GeSe_4

Mn1 – coordination			
Mn1 – Se1	269.64(5) × 2	Se1 – Mn1 – Se1	180
Mn1 – Se2	268.94(5) × 2	Se1 – Mn1 – Se3	83.33(1) × 2
Mn1 – Se3	273.61(5) × 2	Se1 – Mn1 – Se3	96.67(1) × 2
Se1 – Se2	371.6(0) × 2	Se2 – Mn1 – Se1	87.27(2) × 2
Se1 – Se2	389.8(1) × 2	Se2 – Mn1 – Se1	92.74(2) × 2
Se1 – Se3	361.1(0) × 2	Se2 – Mn1 – Se2	180
Se1 – Se3	405.9(1) × 2	Se2 – Mn1 – Se3	85.81(1) × 2
Se2 – Se3	369.4(1) × 2	Se2 – Mn1 – Se3	94.19(1) × 2
Se2 – Se3	397.4(0) × 2	Se3 – Mn1 – Se3	180
Mn2 - coordination			
Mn2 – Se1	272.46(8)	Se1 – Mn2 – Se3	82.31(2) × 2
Mn2 – Se2	264.91(8)	Se2 – Mn2 – Se1	173.37(2)
Mn2 – Se3	271.72(6) × 2	Se2 – Mn2 – Se3	92.74(2) × 2
Mn2 – Se3	276.29(6) × 2	Se2 – Mn2 – Se3	96.04(2) × 2
Se1 – Se3	361.1(0) × 2	Se3 – Mn2 – Se1	88.29(2) × 2
Se1 – Se3	379.0(1) × 2	Se3 – Mn2 – Se3	82.84(2)
Se2 – Se3	391.8(1) × 2	Se3 – Mn2 – Se3	88.74(2) × 2
Se2 – Se3	398.9(0) × 2	Se3 – Mn2 – Se3	98.25(3)
Se3 – Se3	365.6(1)	Se3 – Mn2 – Se3	168.12(2) × 2
Se3 – Se3	383.3(0) × 2		
Se3 – Se3	410.9(1)		
Ge – coordination			
Ge – Se1	231.74(6)	Se1 – Ge – Se2	116.25(2)
Ge – Se2	236.13(6)	Se1 – Ge – Se3	115.57(1) × 2
Ge – Se3	236.04(5) × 2	Se3 – Ge – Se2	102.95(2) × 2
Se1 – Se2	397.3(1)	Se3 – Ge – Se3	101.51(2)
Se1 – Se3	395.8(1) × 2		
Se2 – Se3	369.4(1) × 2		
Se3 – Se3	365.6(1)		

The (GeSe$_4$) tetrahedra are almost regular, as Ge – Se distances correspond with the sum of the effective ionic radii ($r_{Ge +IV}$ = 39 pm for coordination number 4, $r_{Se -II}$ = 198 pm) [33] and are in good agreement with the data given in the literature [35, 36]. The presence of three longer distances leads to a small shortening of the tetrahedra along [001] (Fig. 4.12). The shared Se – Se edges as in the (MnSe$_6$) octahedra are shorter than the unshared ones.
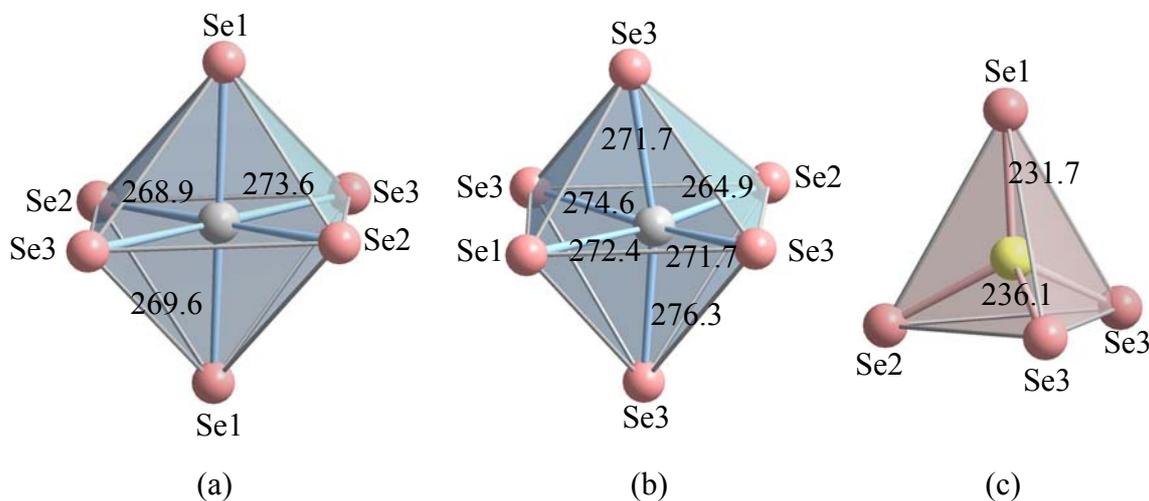
Fig. 4.12: Cation coordination polyhedra in Mn$_2$GeSe$_4$. The Mn1 octahedron (a) is less distorted compared to that of Mn2 (b). The (GeSe$_4$) tetrahedra (c) is weakly flattened along [001]. Distances are given in pm

4.6 MAPLE calculations

The **MA**delung **P**art of the **L**attice **E**nergy (MAPLE) of Mn$_2$GeSe$_4$ can be calculated as the sum of MAPLE of the binary compounds MnSe [37] and GeSe$_2$ [35], using the theory for "additivity" of MAPLE [38, 39]:

$$MAPLE(Mn_2GeSe_4) = 2 \times MAPLE(MnSe) + MAPLE(GeSe_2) \quad (4.1)$$

The MAPLE of MnSe and GeSe$_2$ was calculated using the program MAP 4 [40] and their sum was compared with the MAPLE value of Mn$_2$GeSe$_4$ which was calculated using the same program. Table 4.8 represents the calculated MAPLE values for Mn$_2$GeSe$_4$, MnSe and GeSe$_2$. MAPLE of Mn$_2$GeSe$_4$ calculated by formula 4.1 is 4026.271 kcal mol^{-1}, which is somewhat smaller than the value 4131.663 kcal mol^{-1}, calculated by the program MAP 4 using the data from the structure refinement. The difference Δ MAPLE, is 105.3916 kcal mol^{-1} or 2.58%.

This value shows good agreement between the expected and calculated MAPLE of Mn_2GeSe_4; nevertheless it is significantly bigger than the adopted "normal" values of Δ MAPLE $\sim$ 1% [41]. The coordination number of Mn or Ge does not influence this discrepancy. Both manganese and germanium have the same coordination number in the binary compounds and in Mn_2GeSe_4, Mn is surrounded octahedrally by six Se atoms [37] and Ge is tetrahedrally coordinated with four Se atoms [35].

Table 4.8: MAPLE values of Mn_2GeSe_4, MnSe and $GeSe_2$ / kcal mol^{-1}

Mn₂GeSe₄			MnSe			GeSe₂		
Atom	**Charge**	**MAPLE**	**Atom**	**Charge**	**MAPLE**	**Atom**	**Charge**	**MAPLE**
Mn1	+2	414.3885	Mn1	+2	431.3449	Ge1	+4	1378.4954
Mn2	+2	467.5016	Se1	-2	431.3449	Ge2	+4	1354.6416
Ge1	+4	1464.6629				Ge3	+4	1339.1912
Se1	-2	429.6109				Ge4	+4	1341.2694
Se2	-2	463.6370				Se1	-2	465.6989
Se3	-2	462.2509				Se2	-2	446.6435
						Se3	-2	467.7770
						Se4	-2	482.8623
						Se5	-2	480.6346
						Se6	-2	464.4613
						Se7	-2	502.6339
						Se8	-2	479.2571
		Σ 4131.6626			Σ 862.6897			Σ 2300.8916

The calculated density of Mn_2GeSe_4 (5.062 g/cm^3) is slightly smaller than the expected value (5.097 g/cm^3) which is calculated on the basis of the density increments of MnSe (5.45 g/cm^3) [42] and $GeSe_2$ (4.39 g/cm^3) [35]:

$$\rho = \frac{2 \times \rho_{MnSe} + \rho_{GeSe_2}}{3} = 5.097 \ \text{g/cm}^3 \qquad (4.2)$$

The difference between the expected and calculated density ($\Delta\rho = 0.035$ g/cm^3) explains the greater value of Δ MAPLE.

4.7 Olivine or spinel structure

It is well known that olivine and spinel type compounds have the same general formula A_2BX_4 (A = transition or alkali earth metal, B = Si, Ge, Sn, X = O, S, Se). The two structures differ in the chalcogen arrangement – in olivine the chalcogen atoms form a hexagonal close packing, while in spinel they form a cubic close packing. The cations have the same coordination. Consideration of the polyhedral size reveal that the olivine structure is stable in the case of small, tetrahedrally coordinated cations and relatively large octahedrally coordinated cations. In contrast, the spinel is stable when there are large cations with tetrahedral coordination and small cations in the octahedral [30, 34].

The limit between these two structures is given by the ideal case of close packed spheres and can be described by the ratio [30, 34]:

$$\frac{d_{(A-X)_{mean}}}{d_{(B-X)_{mean}}} = \frac{2}{\sqrt{3}} = 1.155$$

where $d_{(A-X)_{mean}}$ is the mean (A – X) distance and $d_{(B-X)_{mean}}$ is the mean value of the (B – X) distances.

The olivine is stable above and the spinel below this limiting value.

For Mn₂GeSe₄ this value is given by the equation:

$$\frac{d_{(A-X)_{mean}}}{d_{(B-X)_{mean}}} = \frac{271.08}{234.99} = 1.154$$

where $d_{(A-X)_{mean}}$ is the mean Mn – Se distance and $d_{(B-X)_{mean}}$ is the mean Ge – Se distance, calculated from the interatomic distances obtained after structure refinement.

This value is somewhat smaller than the limiting value, but the difference is very small (0.08%). It is also found that other factors, which favour the olivine structure, include the shortening of the shared edges, which reduces metal – metal repulsion between cations occupying adjacent polyhedra. This is observed in many olivine compounds [34]. The second factor stabilizing the olivine structure is the relative covalence of the A – X bonds.

Both factors are observed in Mn₂GeSe₄. The shared edges are significantly shorter than the unshared ones and Mn – Se bonds have a relative strong covalent character. A more covalent character of the bonds corresponds to a greater hybridisation of the metal and ligand orbitals.

The d_{HS}^5 configuration of manganese probably adds stability to the olivine structure [30]. Nevertheless, the eventual transition from an olivine – type structure to a spinel at high temperatures and pressure for Mn_2GeSe_4 is presumable.

4.8 Magnetic measurements

The magnetic measurements have been realized with a SQUID – magnetometer. Powder samples of Mn_2GeSe_4 were measured in the temperature range from 5K to 300K. For determining the dependence of the magnetic susceptibility from the magnetic field different, fields were applied.

Fig. 4.14 represents the inverse magnetic susceptibility measured at a strength field of 100 Oe and 50000 Oe, after cooling under zero field (ZFC). At high temperatures (T > 150 K), the curve has a classical behaviour, following the Curie – Weiss law, $1/\chi = (T - \Theta)/C$ with a paramagnetic Curie temperature $\Theta = -240(5)$ K. This indicates a predominance of antiferromagnetic interactions (Fig. 4.13). The Curie constant C, has a value of 4.35(5) emu/mol K, which corresponds to an effective magnetic moment $\mu = 5.90$ μ_{Bohr}. This value indicates a $3d^5$ configuration of the Mn^{2+} ions ($S = 5/2$).

| (a) | (b) | (c) |
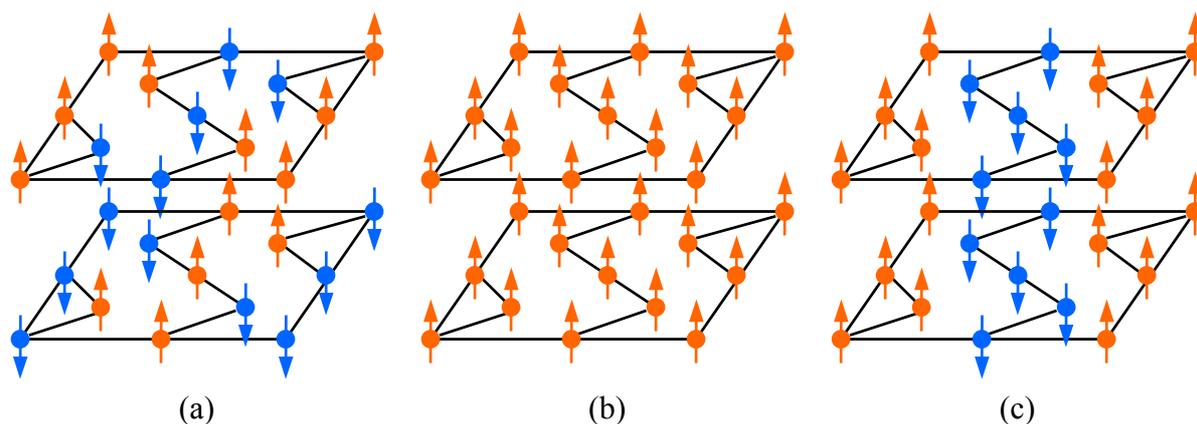
Fig. 4.13: Antiferromagnetic (a), ferromagnetic (b) and ferrimagnetic (c) spin ordering
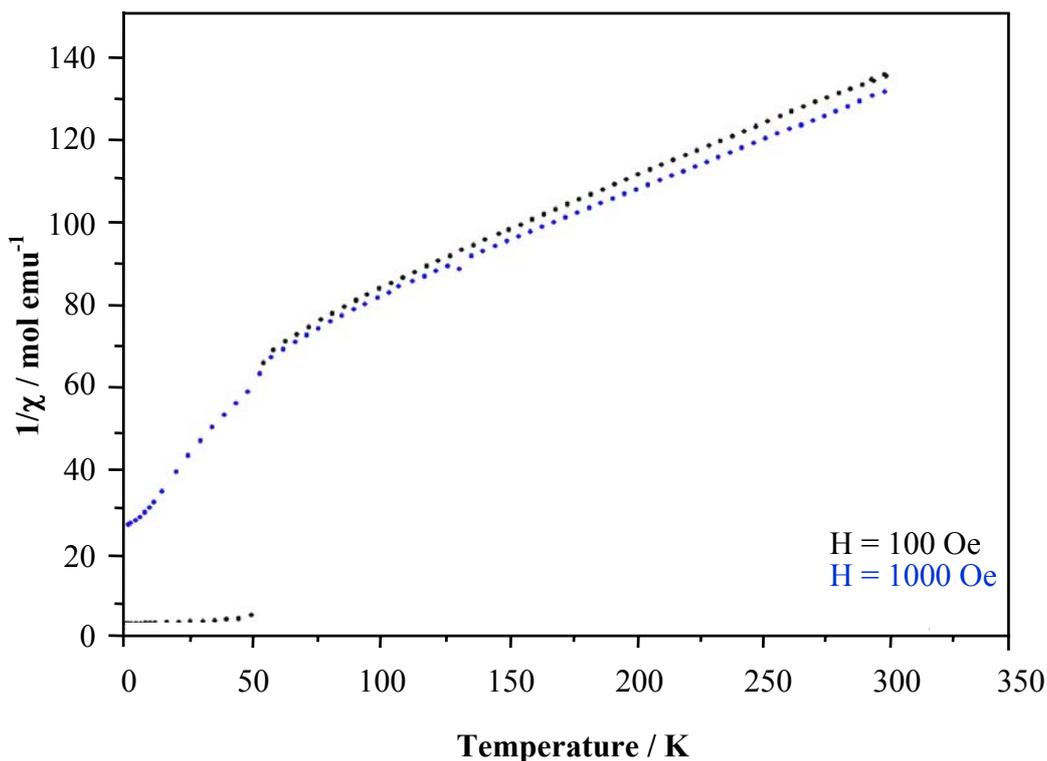
Fig. 4.14: Inverse magnetic susceptibility of Mn_2GeSe_4 as a function of the temperature

At temperatures lower than 150 K a deviation from the Curie – Weiss law is observed. The abrupt drop of the $1/\chi$ value at 66.3 K leads to a break in the curve. At temperatures below ~ 66 K $1/\chi$ continues to decrease before levelling off close to 0 K. This probably corresponds to a weak ferromagnetically ordered compound, which is saturated when a high field is applied. Correspondingly, the $1/\chi$ drop at the higher field is not so sharp. Very similar magnetic behaviour is already observed for Fe_2GeS_4 [42]. Its magnetic moment vectors are found to be aligned parallel to (110). Similar ordering is also observed in many other compounds having olivine – type structure [24, 25, 27, 28, 31, 43 – 52].

5 Cr₂Ge₂Se₆ – a new member of M₂X₂Y₆ compounds (M = Transition metal, X = Si, Ge, Y = Chalcogen)

5.1 Structure – chemical relations

Ternary transition metal chalcogenophosphates (IV) with the general formula $M_2P_2Y_6$ (M = V, Mn, Fe, Co, Ni, Pd, Zn, Cd or Hg, Y = S, Se) present a great variety of compounds [53 – 62]. They are regarded as salts of the hypothetic hexathiohypodiphosphoric acid – $H_4P_2S_6$ [53, 54] and crystallise in two main crystal types though differing in the chalcogen arrangement:

I. $CdCl_2$ – type (cubic close packing of chlorine atoms). All $M_2P_2S_6$ compounds and two of the selenium derivates ($Cr_2P_2Se_6$ and $Ni_2P_2Se_6$) belong to this structure type. Their structures can be derived from the $CdCl_2$ – type, if it is assumed that Cd is replaced by M^{2+} cations and pairs of phosphor atoms in the ratio 2 : 1.

II: CdI_2 – type (hexagonal close packing of iodine atoms). Only compounds having the general formula $M_2P_2Se_6$ belong to this structure type. Analogous to the $CdCl_2$ – type, their structure can be derived if cadmium is substituted by M^{2+} cations and pairs of phosphor atoms in the ratio of 2:1.

In both structure types every second octahedra layer is fully occupied by the M^{2+} and pairs of phosphor in a ordered way. The occupied layers are separated by van der Waals gaps [54 – 60].

Because of the layered structure of the $M_2P_2Y_6$ compounds they crystallize in the form of very thin platelets. For better absorption correction of the X – ray diffraction data the indices of the crystal faces have been determined [55]. The chalcogen arrangement in those compounds, which crystallise in the $CdCl_2$ – type (cubic close packing of chalcogens) suggests a trigonal symmetry and generally for these compounds a hexagonal cell is encountered [55]. However, their structure refinement parameters have been obtained using the monoclinic cell of $Fe_2P_2S_6$ [55, 57]. A close inspection of their lattice constants shows that for all of them the ratio $\frac{b}{a} = \sqrt{3} = 1.732$ is precisely the same (Tab. 5.1). The *(a, b)* – plane parallel to the layers indicates no distortion in the stacking sequence [55]. Therefore, the deviation from the trigonal symmetry is explained by the value of the monoclinic β - angle [55].

Table 5.1: List of the existing $M_2P_2Y_6$ compounds (italic: results from X – ray powder diffraction)

Compound	Lattice parameters / pm, resp. °, SG, *Z*	Structure type	Ref.
$V_2P_2S_6$	$a = 586.7(1)$, $b = 1016.0(2)$, $c = 665.7(1)$, $\beta = 107.08(2)$, $C2/m$, $Z = 4$, $b/a = 1.732$	$CdCl_2$	[59]
$Mn_2P_2S_6$	$a = 607.7(1)$, $b = 1052.4(3)$, $c = 679.6(1)$, $\beta = 107.35(2)$, $C2/m$, $Z = 4$, $b/a = 1.738$	$CdCl_2$	[55, 56]
$Fe_2P_2S_6$	$a = 594.7(1)$, $b = 1030.0(1)$, $c = 672.22(8)$, $\beta = 107.16(1)$, $C2/m$, $Z = 4$, $b/a = 1.732$	$CdCl_2$	[55, 56]
$Co_2P_2S_6$	$a = 590.1(1)$, $b = 1022.2(2)$, $c = 665.8(2)$, $\beta = 107.17(2)$, $C2/m$, $Z = 4$, $b/a = 1.732$	$CdCl_2$	[55, 56]
$Ni_2P_2S_6$	$a = 581,2(2)$, $b = 1007.0(3)$, $c = 663.2(1)$, $\beta = 106,98(3)$, $C2/m$, $Z = 4$, $b/a = 1.732$	$CdCl_2$	[55, 56]
$Pd_2P_2S_6$	$a = 597$, $b = 1032$, $c = 673$, $\beta = 107.1$, $C2/m$, $Z = 2$, $b/a = 1.729$	$CdCl_2$	[53, 58]
$Zn_2P_2S_6$	$a = 597.2(4)$, $b = 1034.2(8)$, $c = 675.7(5)$, $\beta = 107.14(4)$, $C2/m$, $Z = 4$, $b/a = 1.725$	$CdCl_2$	[60, 62]
$Cd_2P_2S_6$	$a = 621.8(1)$, $b = 1076.3(2)$, $c = 686.7(1)$, $\beta = 107.58(1)$, $C2/m$, $Z = 4$, $b/a = 1.729$	$CdCl_2$	[55, 56, 62]
$Hg_2P_2S_6$	$a = 625.2(3)$, $b = 626.2(4)$, $c = 712.6(6)$, $\alpha = 96.21(6)$ $\beta = 105.69(6)$, $\gamma = 119.15(4)$, $P\overline{1}$, $Z = 1$	–	[58]
$V_2P_2Se_6$	$a = 584$, $c = 1844$, $\gamma = 120$, $R\overline{3}$	CdI_2	[59]
$Cr_2P_2Se_6$	$a = 614.8(1)$, $b = 1059.0(2)$, $c = 668.9(2)$, $\beta = 107.71(2)$, $C2/m$, $b/a = 1.722$	$CdCl_2$	[57]
$Mn_2P_2Se_6$	$a = 638.5(1)$, $c = 2003.8(4)$, $\gamma = 120$, $R\overline{3}$	CdI_2	[57, 61]
$Fe_2P_2Se_6$	$a = 626.5(6)$, $c = 1980.0(2)$, $\gamma = 120$, $R\overline{3}$, $Z = 3$	CdI_2	[57]
$Ni_2P_2Se_6$	$a = 613.7(2)$, $b = 1061.1(3)$, $c = 687.0(3)$, $\beta = 107.46(2)$, $C2/m$, $b/a = 1.729$	$CdCl_2$	[57]
$Cd_2P_2Se_6$	$a = 651.2(1)$, $c = 2006.5(4)$, $\gamma = 120$, $R\overline{3}$	CdI_2	[57]
$Hg_2P_2Se_6$	$a = 654.5(3)$, $b = 1137.7(3)$, $c = 1361.0(5)$, $\beta = 98.47(5)$, $C2/c$, $Z = 4$	–	[58]

In the structure of "V$_2$P$_2$S$_6$", cationic vacancies are observed [59], which leads to the formation of a mixed valence compound with the real formula - $V^{II}_{0,68}V^{III}_{0,88}P_2S_6$ (V$_{1,56}$P$_2$S$_6$).

In Co$_2$P$_2$S$_6$ and Ni$_2$P$_2$S$_6$ a partial substitution of phosphorous by metal is observed [55].

Hg$_2$P$_2$S$_6$ and Hg$_2$P$_2$Se$_6$ belong neither to the CdCl$_2$ nor to the CdI$_2$ structure type. Their structures are closely related to the M$_2$P$_2$Y$_6$ compounds. The Hg – atoms have the coordination number 4, in contrast to the coordination number of 6, which is characteristic of metal cations in the members of the M$_2$P$_2$Y$_6$ family. The decrease in the metal coordination number is accompanied by a decrease in the symmetry and results from the $d^{10}s^2$ – electronic configuration of mercury, which favours much more coordination numbers 2, 3 and 4, but not 6[58].

The permanent request for new compounds revealed the possibility of substituting phosphor with its neighbours in the periodic table namely Si and Ge. For charge balance, the M(II) ions have to be replaced by M(III) transition metal ions or an additional cation is necessary (see below). Contrary to expectations, the transition metal chalcogenides isostructural to M$_2$P$_2$Y$_6$, which contain Si or Ge pairs are quite rare. They are represented by three tellurosilicates [4 – 7] and one tellurogermanate [8] (Table 5.2) with the general formula M$_2$X$_2$Te$_6$ (M = transition metal, X = Si, Ge), as up to now sulphides and selenides are not mentioned in the literature at all.

Table 5.2: List of the existing M$_2$X$_2$Te$_6$ compounds

Compound	Lattice parameters / pm, resp. °, SG, *Z*	Structure type	Ref.
Sc$_2$Si$_2$Te$_6$	a = 700.65(5), c = 2129.2(1), γ = 120	–	[6]
Cr$_2$Si$_2$Te$_6$	a = 675.8(1), c = 2066.2(1), γ = 120, *R3*, *Z* = 3	CdI$_2$	[4,5]
Cr$_2$Ge$_2$Te$_6$	a = 682.7(0), c = 2056.2(1), γ = 120, $R\bar{3}$, *Z* = 3	CdI$_2$	[8]
Mn$_3$Si$_2$Te$_6$	a = 702.9(2), c= 1425.5(3), γ = 120, $P\bar{3}1c$, *Z* = 2	–	[7]

All M$_2$X$_2$Te$_6$ compounds have trigonal symmetry, except Sc$_2$Si$_2$Te$_6$ for which only powder data are available and these are indexed hexagonal. The M$_2$X$_2$Te$_6$ compounds have layered structures, similar to the M$_2$P$_2$Y$_6$ structure. The layers alternate along the c – axis and are separated by van der Waals gaps (d$_{Te – Te}$ = 405.5(2) pm for Cr$_2$Si$_2$Te$_6$ and d$_{Te – Te}$=399.0(1) pm for Cr$_2$Ge$_2$Te$_6$) [5]. Each layer is composed of a double sublayer of Te atoms. The metal atoms and Si$_2$ or Ge$_2$ dumbbells occupy slightly distorted octahedral holes within the tellurium sublayers. The structure is consists of two building units – (MTe$_6$) octahedra, where

M is a transition metal and (X$_2$Te$_6$) octahedra, where X$_2$ is a pair of silicon or germanium atoms. Each (X$_2$Te$_6$) octahedron is surrounded by six (MTe$_6$) octahedra, sharing common edges and each (MTe$_6$) octahedron is surrounded by three (MTe$_6$) and three (X$_2$Te$_6$) octahedra (Fig. 5.1).
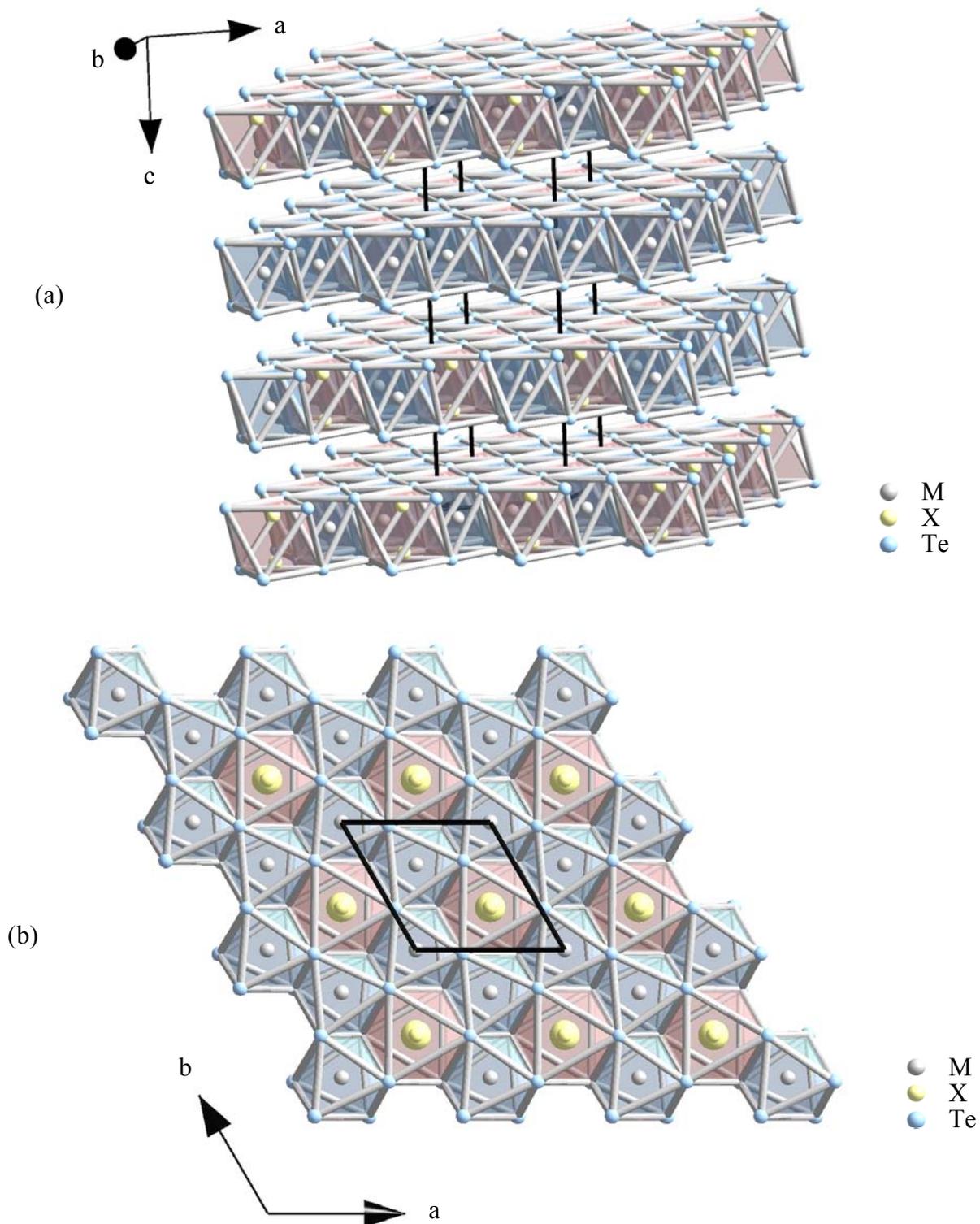
Fig. 5.1: General projection of the M$_2$X$_2$Te$_6$ structure (M = transition metal X = Si or Ge) (a) and polyhedra arrangement within a double sublayer composed of tellurium (b)

The structure of $Mn_3Si_2Te_6$ can be regarded as a somewhat modified $M_2X_2Te_6$ structure. As is visible from the stoichiometric formula, one Mn atom is in "excess". This additional atom, which has an octahedral coordination is located in the van der Waals gap and shares a common face with one ($MnTe_6$) octahedron from the layer above and one from the layer below [7] i. e. it links the layers along [001] (Fig. 5.2).
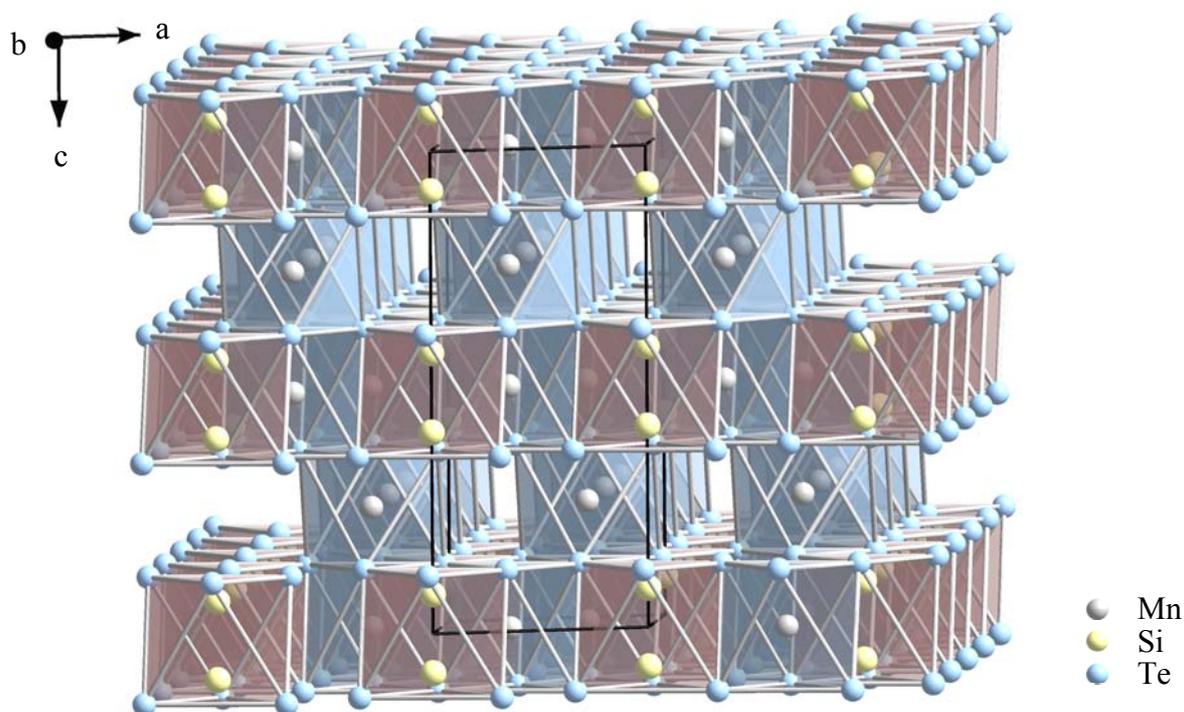
Fig. 5.2: The crystal structure of $Mn_3Si_2Te_6$. The layers along [001] are connected via ($MnTe_6$) octahedra located within the van der Waals gap.

The interatomic distances observed in the existing $M_2X_2Te_6$ (M = transition metal, X = Si, Ge) and $M_2P_2Y_6$ (M = transition metal, Y = S, Se) compounds are given in Table 5.3. The Si – Si bonds, which are in the range of 226.5(7) pm to 232.4(1) pm are longer than the similar P – P bonds, but are shorter than the Ge – Ge bonds in $Cr_2Ge_2Te_6$. This is in good agreement with the atomic size of the elements belonging to the IVA group. The metal – chalcogen bonds in both structure families correspond to the sum of the effective ionic radii confirming to octahedral coordination [33], and vary in a wide range, depending on the type of the metal and chalcogen ions.

Table 5.3: Interatomic distances in $M_2X_2Te_6$ (M = transition metal, X = Si, Ge) and $M_2P_2Y_6$ (M = transition metal, Y = S, Se)

Compound	d_{X-X}, resp. d_{P-P} / pm	d_{M-Te}, resp. d_{M-Y} / pm
$V_2P_2S_6$	216.0(3)	250.2(2) – 250.4(2)
$Mn_2P_2S_6$	218.7(3)	261.9(1) – 263.4(1)
$Fe_2P_2S_6$	217.4(3)	254.4(1) – 255.2(1)
$Co_2P_2S_6$	216.5(3)	250.6(1) – 251.1(1)
$Ni_2P_2S_6$	214.8(4)	246.1(2) – 246.6(2)
$Pd_2P_2S_6$	no data	no data
$Zn_2P_2S_6$	218.6(3)	256.2(1) – 257.5(1)
$Cd_2P_2S_6$	222.2(2)	270.9(1) – 274.0(1)
$Hg_2P_2S_6$	226.7(1)	243.9(9) – 282.4(8)
$V_2P_2Se_6$	no data	no data
$Cr_2P_2Se_6$	no data	no data
$Mn_2P_2Se_6$	no data	no data
$Fe_2P_2Se_6$	224(6)	255(4) – 269(4)
$Ni_2P_2Se_6$	no data	no data
$Cd_2P_2Se_6$	no data	no data
$Hg_2P_2Se_6$	224.6(4)	258.0(4) – 278.2(4)
$Sc_2Si_2Te_6$	no data	no data
$Cr_2Si_2Te_6$	226.5(7)	275.1(3) – 280.3(2)
$Cr_2Ge_2Te_6$	245.9(6)	274.1(7) – 275.7(7)
$Mn_3Si_2Te_6$	232.4(2)	290.7(3) – 295.1(4)

5.2 Preparation and properties

$Cr_2Ge_2Se_6$ was synthesised by a solid – state reaction. The pure elements Cr, Ge and Se in powder form were blended in an agate mortar in stoichiometric proportions (Cr : Ge : Se = 2 : 2 : 6). The prepared mixture was transferred to a quartz glass ampoule. After evacuation and sealing, the ampoule was heated in a furnace with a rate of 50 °C/h until the desired temperature of 600°C was reached. After annealing for 20 days, the oven was cooled down to room temperature.

The product appeared as a homogenous bulk of dark – grey to black powder, formed by many very small crystals (Fig. 5.3). The powder is water and air stable.

The preparation attempts to get crystals of $Cr_2Ge_2Se_6$ were carried out in two ways. First, a transport reaction (temperature gradient 600/200°C, evacuated silica ampoule, l ≈ 20cm) was performed with iodine as a transport agent. After each experiment the phases $GeSe_2$ and CrSe were always found, but never $Cr_2Ge_2Se_6$. The second method was a preparation of pellets. Regardless of the reaction time and temperature, the result was always powder of $Cr_2Ge_2Se_6$ or crystals with extremely small size, not sufficiently big for X – ray single crystal analysis.
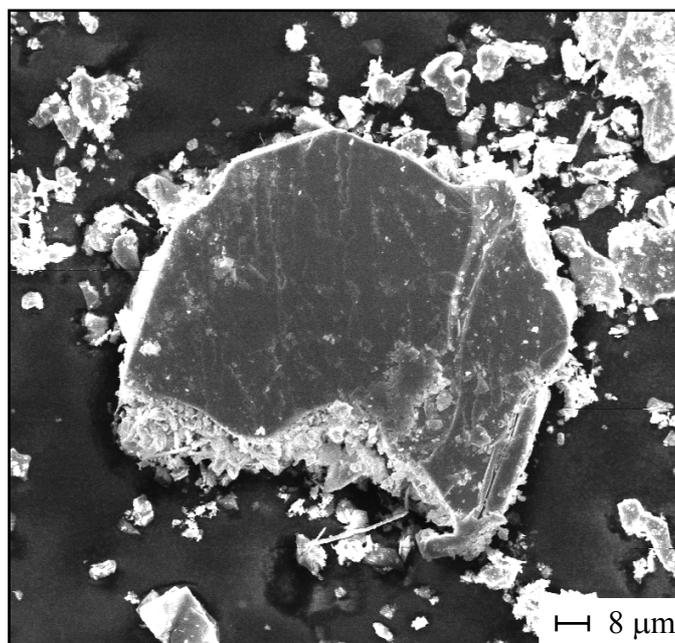
Fig. 5.3: SEM image of $Cr_2Ge_2Se_6$ crystals

The melting temperature t of $Cr_2Ge_2Se_6$ is 646°C and was determined by DTA. The thermal analysis curve is represented in Fig. 5.4. Upon cooling one exothermal effect at 540°C is observed.
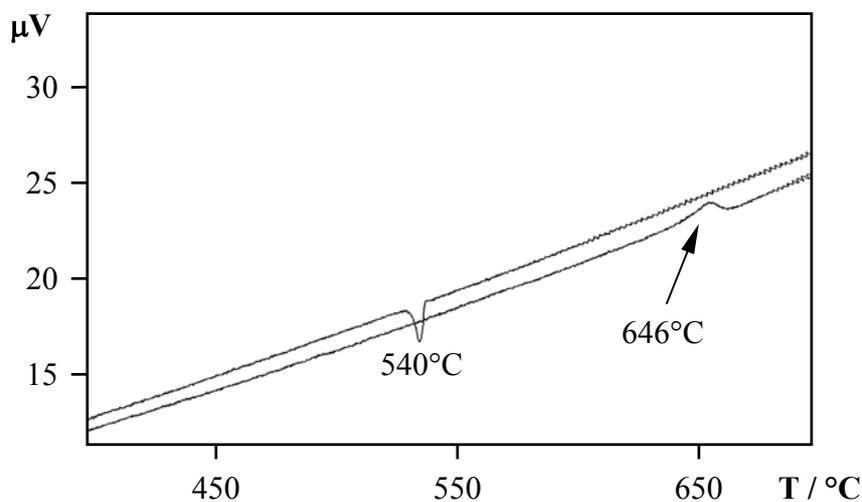
Fig. 5.4: DTA measurement of $Cr_2Ge_2Se_6$. The heating curve shows one endothermic effect at 646°C. Upon cooling one exothermal effect is observed

In order to explain the melting behaviour of $Cr_2Ge_2Se_6$, the substance was investigated using X – ray powder diffractometry after conducting a thermal analysis. In the powder pattern together with the reflections of the compound, additional reflection. which belong to Cr_2Se_3 and $GeSe_2$, respectively are observed (Fig. 5.5). This indicates that $Cr_2Ge_2Se_6$ melts incongruently. As a result of cooling, a mixture of the three compounds, $Cr_2Ge_2Se_6$, Cr_2Se_3 and $GeSe_2$ crystallizes, which is common for incongruently melting compounds [3].
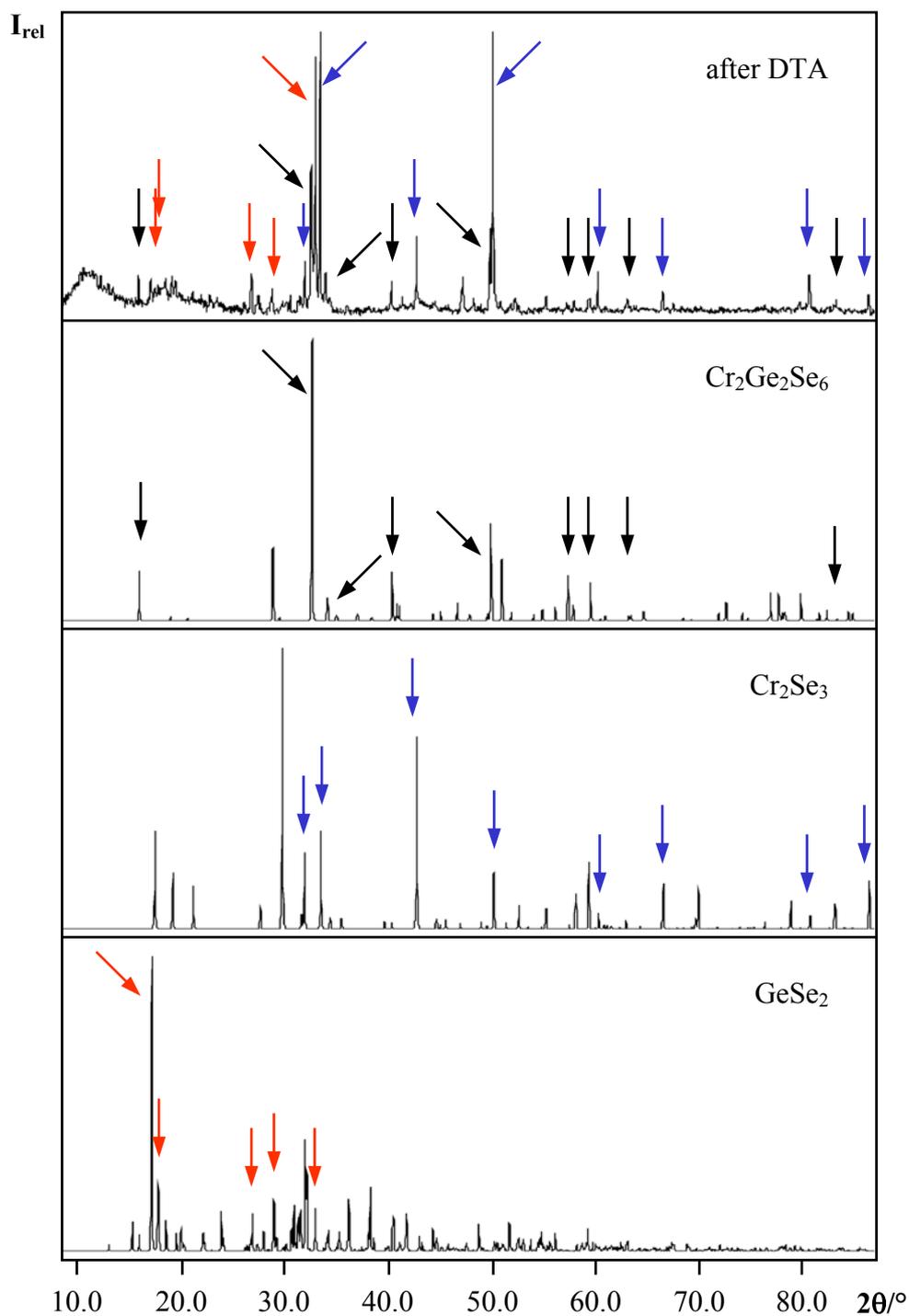
Fig. 5.5: Comparison between the measured powder pattern of "Cr₂Ge₂Se₆" after DTA experiment (top) and the calculated patterns of Cr₂Ge₂Se₆, Cr₂Se₃ and GeSe₂

5.3 Characterization

Fig. 5.6 represents the comparison between the X – ray powder patterns of $Cr_2Ge_2Se_6$ and $Cr_2Ge_2Te_6$. The $Cr_2Ge_2Se_6$ powder pattern is shifted to higher *2θ* – values compared to that of $Cr_2Ge_2Te_6$, which is expected due to the smaller effective ionic radii of Se^{2-} compared to that of Te^{2-} [33].
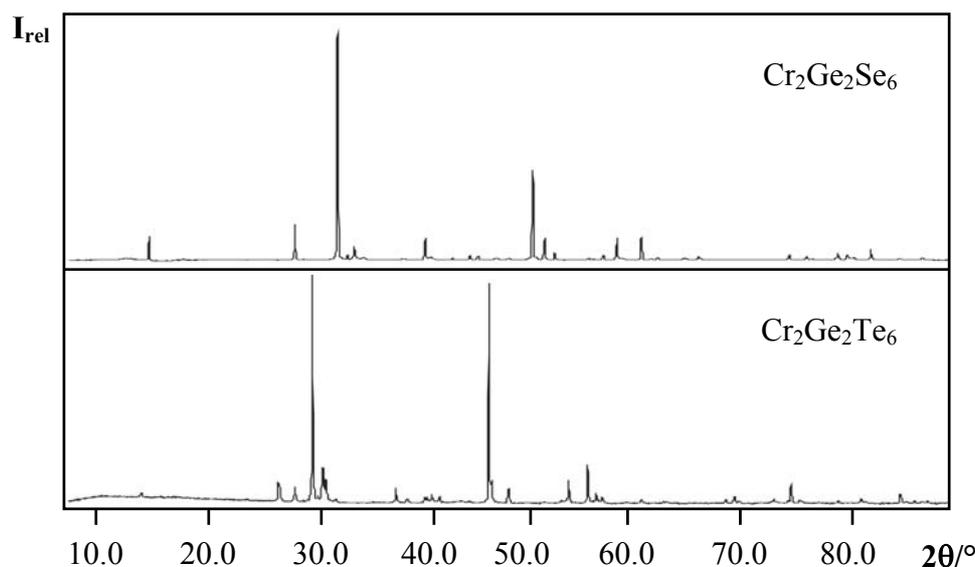
Fig. 5.6: Comparison between the measured X – ray powder patterns of $Cr_2Ge_2Se_6$ (top) and $Cr_2Ge_2Te_6$ (bottom)

If $Cr_2Ge_2Se_6$ crystallizes isotypically to $Cr_2Ge_2Te_6$, the atomic positions of Cr, Ge and Se in the crystal structure of $Cr_2Ge_2Se_6$ may differ slightly (but not necessarily) from the atomic positions of Cr, Ge and Te in the structure of $Cr_2Ge_2Te_6$. On the basis of this assumption, a theoretical powder pattern of $Cr_2Ge_2Se_6$ was calculated. It corresponds very well to the experimentally measured one (Fig. 5.7).

Indexing and refining of the experimentally measured X – ray powder pattern supposes a hexagonal symmetry with lattice constants and a volume of the elementary cell smaller than that of $Cr_2Ge_2Te_6$ (Tab. 5.4). The observed reflections for $Cr_2Ge_2Se_6$ are listed in Table 11.6 (see App.). Two reflections, at 32.5° and 42.5° belong to Cr_2Se_3 (Fig. 5.7).
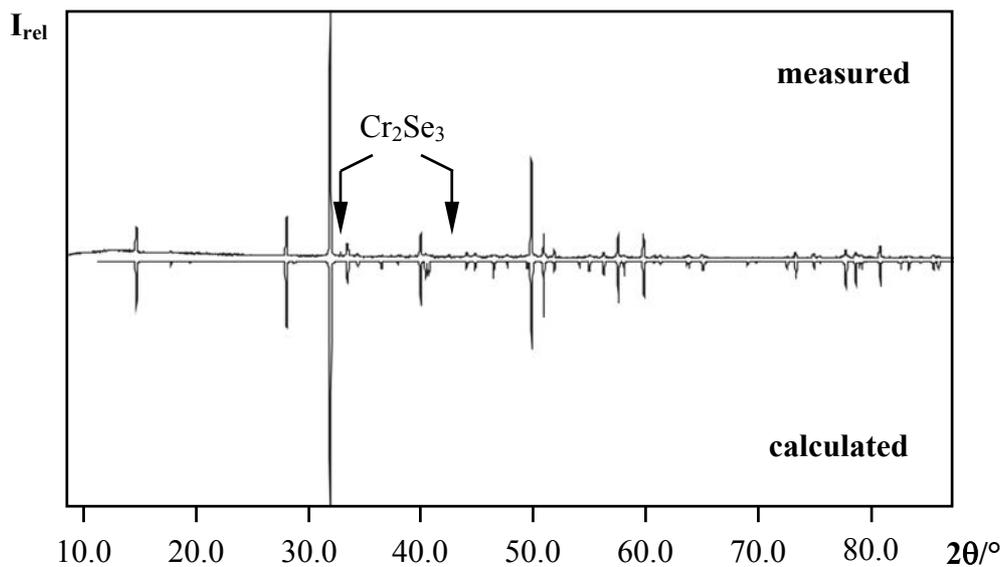
Fig 5.7: Comparison between the measured (top) and calculated powder pattern (atomic positions of $Cr_2Ge_2Te_6$) of $Cr_2Ge_2Se_6$

Table 5.4: Lattice constants and elementary cell volumes of $Cr_2Ge_2Se_6$ and $Cr_2Ge_2Te_6$ obtained from powder data

Compound	a / pm	c / pm	γ / °	$V \times 10^6$ / pm^3
$Cr_2Ge_2Se_6$	629.3(3)	1942.1(6)	120	666.1(5)
$Cr_2Ge_2Te_6$	682.6(4)	2056.2(5)	120	830.1(3)

In order to prove the chemical contents of $Cr_2Ge_2Se_6$, a small piece of the bulk material was examined with an analytical scanning electron microscope (Fig. 5.8). The EDX – spectra shows a relatively good agreement between the expected and the measured content of each element in the substance (Tab. 5.5).

Table 5.5: Expected and observed values for the chemical composition of $Cr_2Ge_2Se_6$ (quantifications based on EDX data)

Element	Observed / atom %	Expected / atom %
Cr	21.82	20.00
Ge	17.79	20.00
Se	60.39	60.00
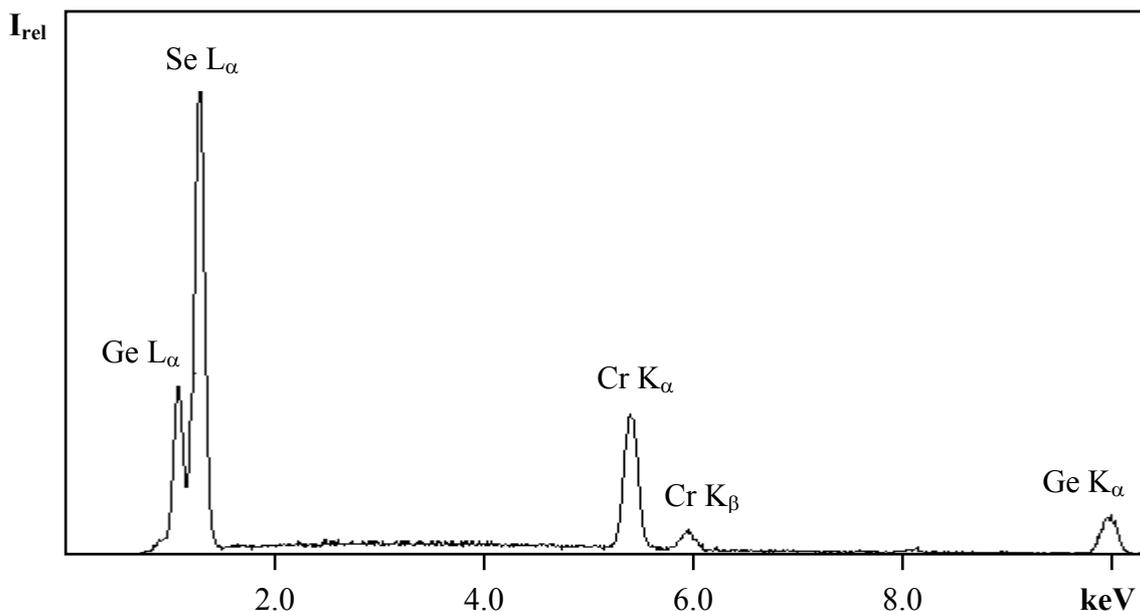
Fig. 5.8: EDX – spectra of $Cr_2Ge_2Se_6$

X – ray powder patterns of the compound were measured at different temperatures in order to investigate the existence of phase transitions at higher temperatures. No phase transitions are observed at temperatures up to 500°C. The thermal expansion of the $Cr_2Ge_2Se_6$ cell parameters is small in both *a* and *b*, whereas a significant increase (two times bigger) can be observed in *c* (Tab. 5.6). This is probably caused by the significantly longer *c* – axis (three times) compared to *a* and *b*, or by any other structural characteristic. Since the structure is not known so far, one can only speculate. In general, an anisotropic thermal expansion is common for non – cubic compounds [3].

Table 5.6: Comparison between the lattice constants and volumes of $Cr_2Ge_2Se_6$ at different temperatures

Temperature / °C	a / pm	c / pm	γ / °	$V \times 10^6$ [pm³]
25	629.3(3)	1942.1(6)	120	666.1(5)
400	630.5(3)	1948.5(5)	120	670.8(5)
500	631.8(3)	1957.9(3)	120	676.8(3)
Δ %	0.4	0.81	–	1.6

The increase of the unit cell parameters results in a small shift to lower 2θ – values in the patterns measured at 400°C and 500°C compared to the one measured at room temperature

(Fig. 5.9). The reflections observed at these temperatures are given in Tab. 11.7 and 11.8 (see App.). In every pattern measured at different temperatures, Cr_2Se_3 reflections at 32.5° and 42.5° are also observed (Fig. 5.9).
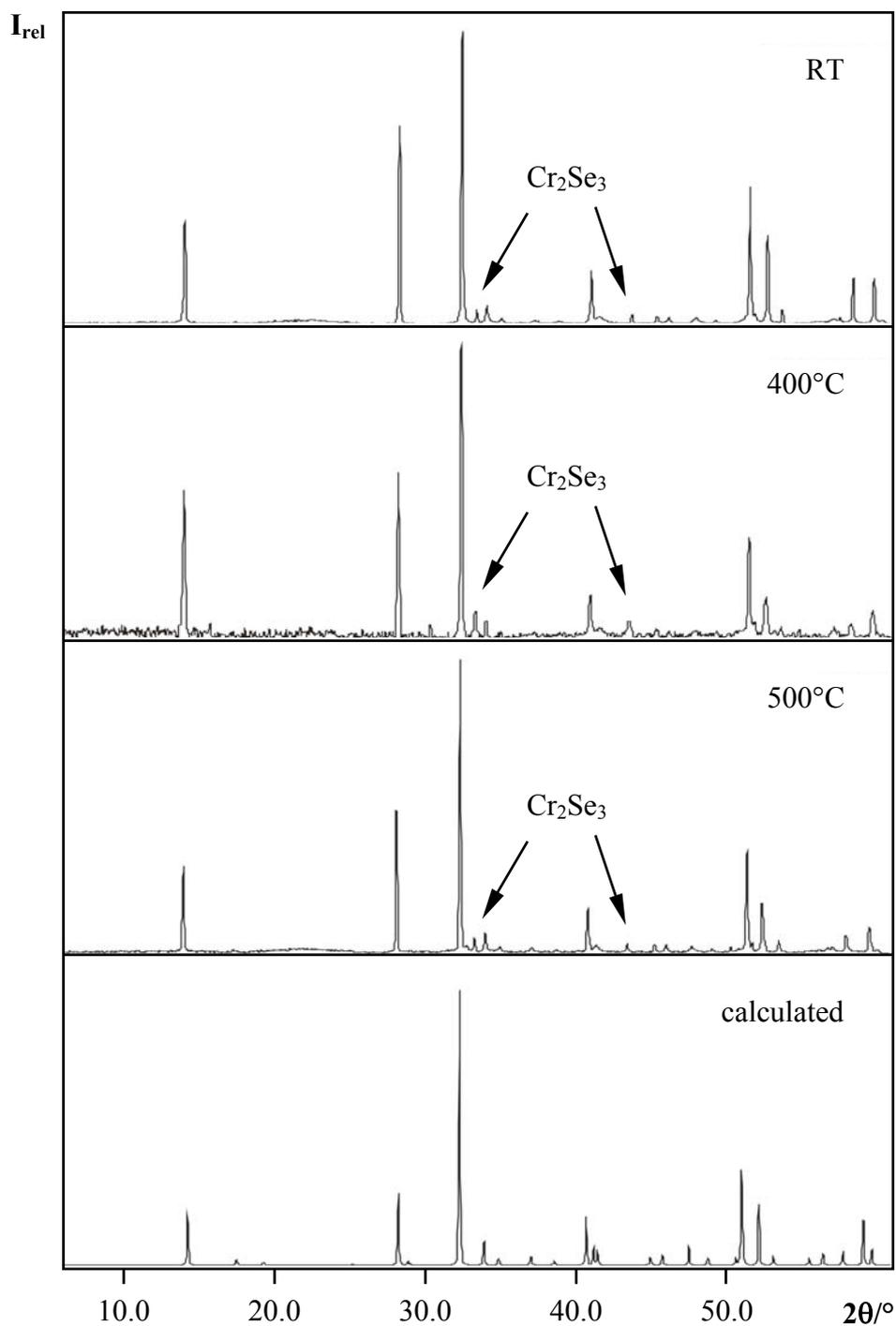
Fig. 5.9: Comparison between the calculated pattern of $Cr_2Ge_2Se_6$ and the patterns for different temperatures

5.4 Outlook

In this chapter the synthesis, characterization and properties of $Cr_2Ge_2Se_6$ were discussed. The chemical content of the compound was proved by EDX – analysis. The thermal behaviour of $Cr_2Ge_2Se_6$was studied with the help of DTA.

Investigation using powder diffractometry showed, that $Cr_2Ge_2Se_6$ has a hexagonal symmetry with the lattice constants *a = b = 629.3(3) pm, c = 1942.1(6) pm, γ = 120°, V = 666.1(5) × 10⁶ pm³*. A high temperature powder diffraction study showed only a thermal expansion of the lattice, but no phase transitions.

The chemical content, hexagonal symmetry and lattice constant close to those of the known $M_2X_2Te_6$ compounds suggest that $Cr_2Ge_2Se_6$ is the first selenide member of this structure type. A thorough discussion represented the close relationship between $M_2X_2Te_6$ and $M_2P_2Y_6$ structure – types.

6 M₃GeTe₂ compounds (M = Fe, Ni)

6.1 Introduction

For many years, a vast number of scientists working in different areas concentrated their attention on the Fe – Ge – Te system because of the amazing properties proposed by compounds containing these elements. Such interest arises due to the specific magnetic properties of different compounds found in this system [63 – 66] and possible transition metal use in thermocouples based on germanium telluride [9].

The only existing compound in the Ge – Te system is GeTe [67]. A number of compounds were found in the Fe – Ge [68 – 71] and Fe – Te [72, 73] systems. Despite exhaustive research, only one ternary compound, Fe_3GeTe_2 is reported in the literature [9]. It was synthesised by Abrikosov et al. who determined its stability range and conducted dilatometric and electrothermal measurements, but it was not structurally characterized.

The close chemical behaviour of iron and nickel induced great efforts in studying in many aspects the similar Ni – Ge – Te system. Except a certain number of compounds in the Ni – Ge [74, 75] and Ni – Te [76, 77] binary systems, ternary compounds in the system Ni – Ge – Te are not known.

In this chapter the properties and crystal structures of Fe_3GeTe_2 and Ni_3GeTe_2, synthesized in the course of this work are presented and their crystal chemistry is discussed.

6.2 The compound Fe₃GeTe₂

6.2.1 Preparation and properties

Fe₃GeTe₂ was synthesised by a solid – state reaction. The pure elements in stoichiometric proportions (Fe : Ge : Te = 3 : 1 : 2) were mixed for several minutes in an agate mortar. The prepared blend was put into a quartz glass ampoule, which was evacuated and sealed. The ampoule was heated in a furnace with a heating rate of 50°C/h until the desired temperature of 625°C was reached. After annealing of two weeks, the furnace was cooled down to room temperature. The resulting product was a homogeneous dark grey powder, which is water and air stable.

In order to get crystals of Fe₃GeTe₂ a pellet from the pure elements mixed in stoichiometric proportions was prepared. It was put in a quartz glass ampoule, which after evacuation and sealing was heated in a furnace with a heating rate of 50°C/h. After reaching the desired temperature of 800°C, the ampoule was annealed for two weeks and then was cooled down to room temperature with a cooling rate of 5°C/h. The resulting dark grey bulk was formed by many good-looking, metal glimmering platelets with hexagonal form (Fig. 6.1).
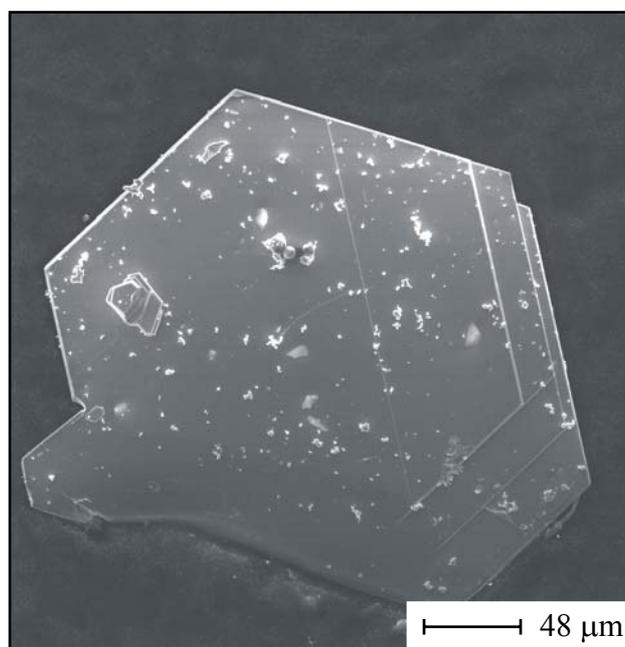
Fig. 6.1: Crystals of Fe₃GeTe₂

The crystals are not air sensitive and stable against water. The thermal behaviour of Fe_3GeTe_2 was investigated by **D**ifferential **T**hermal **A**nalysis. The DTA curve (Fig. 6.2) shows two endothermic effects by heating at 825°C and 837°C, respectively. Upon cooling only one exothermic effect at 825°C is observed. The appearance of two endothermic effects suggests the thermal decomposition of the compound.
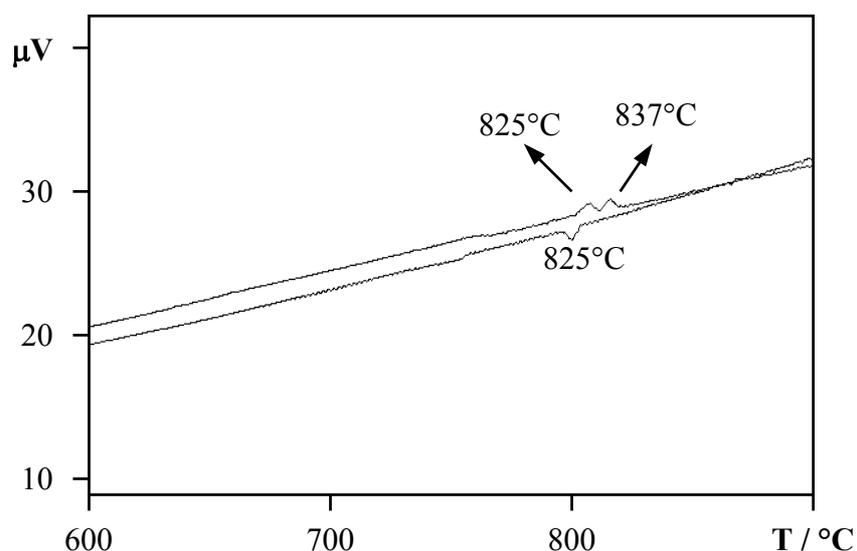
Fig. 6.2: DTA measurement of Fe_3GeTe_2. The heating curve shows two endothermic effects. Upon cooling one exothermic effect at 825°C is observed

In order to explain the melting behaviour of Fe_3GeTe_2 the substance was investigated with X − ray powder diffractcometry, after thermal analysis was carried out. In the measured powder pattern, along with the reflections of the compound additional reflections which belong to $FeTe_2$ and $FeGe$, respectively are also observed (Fig. 6.3). At first it was assumed that Fe_3GeTe_2 decomposes upon heating, as the endothermic effect at 825°C shows its decomposition point and the one at 837°C shows the melting point of $FeTe_2$. Since this temperature is sufficiently higher than its reported melting temperature: 648°C [78], the initial interpretation does not hold true. Therefore, it is assumed that Fe_3GeTe_2 probably first suffers a phase transition at 825°C and then the new polymorph form melts incongruently at 837°C. As a result, by cooling a mixture of three compounds, Fe_3GeTe_2, $FeTe_2$ and $FeGe$ crystallizes, which is common for incongruently melting compounds [3].
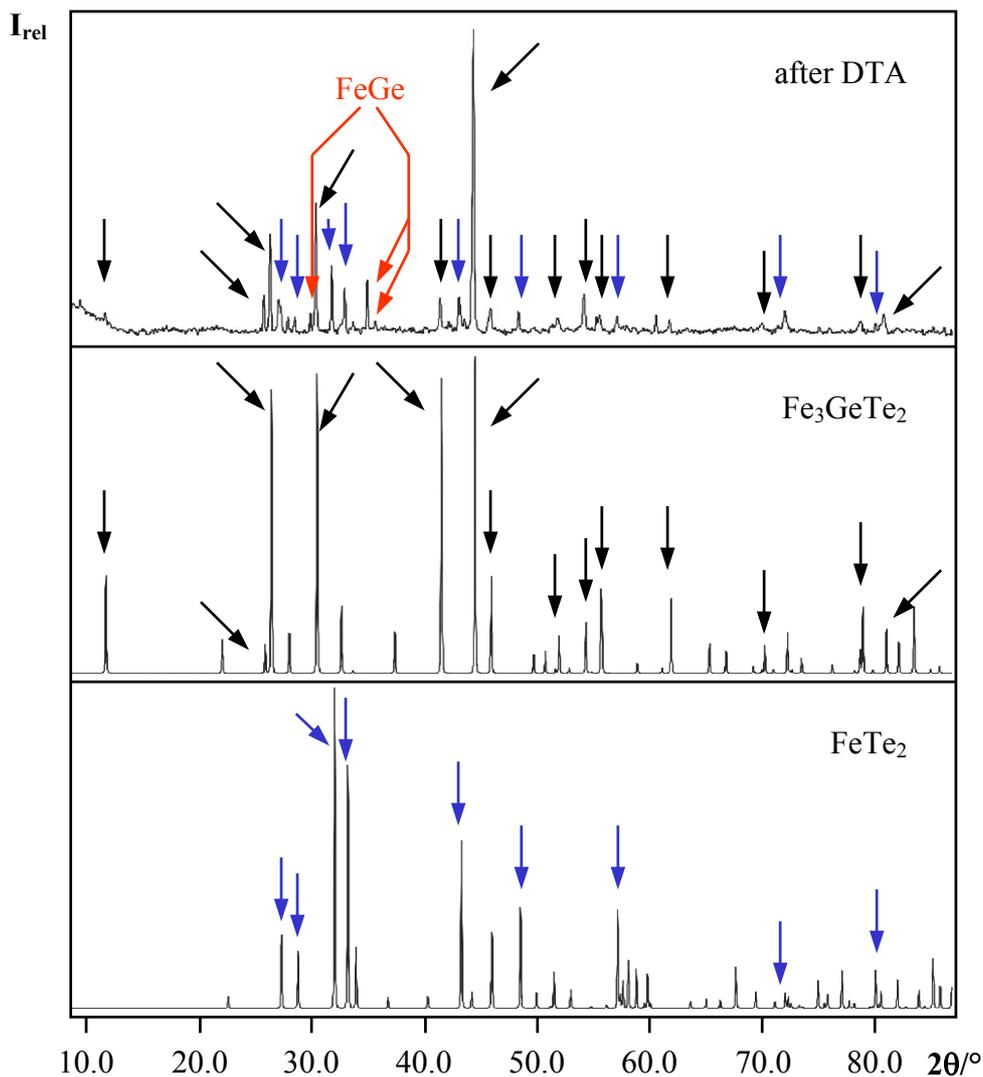
Fig. 6.3: Comparison between the measured powder pattern of "Fe₃GeTe₂" after a DTA experiment (top) and the calculated patterns of Fe₃GeTe₂ and FeTe₂

To prove or reject the existence of possible phase transition of Fe₃GeTe₂ X – ray powder patterns were measured at different temperatures. Despite the very careful sample preparations the capillaries always broke at temperatures over 800°C. This caused oxidation of the compound and prevented further clarification of the problem.

6.2.2 Characterization

Fig. 6.4 represents the experimentally measured X – ray powder pattern of a polycrystalline sample of Fe_3GeTe_2.
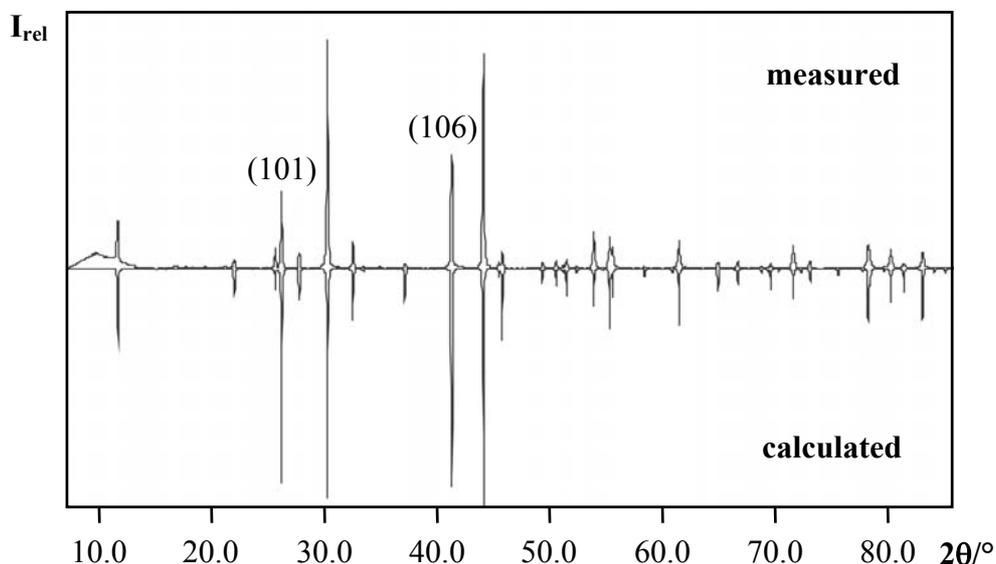
Fig. 6.4: Comparison between the measured powder pattern (top) of Fe_3GeTe_2 and the calculated one (bottom)

The measured powder pattern fits well the pattern calculated on the basis of the lattice constants, the space group and the atom position obtained from the structure refinement. The positions of the reflections in the measured pattern fit with those of the calculated pattern. Reflections from impurities are not observed, but some of the intensities in the measured pattern are significantly lower in comparison with the corresponding intensities in the calculated one. Such "mistakes" in the intensity measurement are clear evidence of a texture effect. This effect is a result of the irregular intensity distribution in the diffraction sphere, due to the non – isotropic distribution of the single particles within the powder sample. [79]. Depending on the location of the measurement point in the sphere of diffraction the intensities are measured either too strong or too weak. Frequently the texture effect appears in samples containing particles with an anisotropic (plate – like, needle – like) form. In particular, plate – like particles have the negative property of decreasing of the particle thickness by grinding (in a mortar), while the overall cross – section of the platelet remains essentially constant. Consequently, this leads to a further increase in the particle distribution anisotropy. The

particles tend to orientate in a preferred direction, which is usually parallel to the plate surface, especially if the surface is smooth.

Indexing of all reflections resulted in a hexagonal cell with the following lattice constants:

a = 401.59(3) pm, c =1633.04(1) pm, γ = 120°, V = 228.08(3) × 10⁶ pm³.

A list of the observed reflections for Fe_3GeTe_2 is given in table 11.9 (see App.).

To analyse the chemical composition, a crystal of Fe_3GeTe_2 was investigated with an analytical scanning electron microscope (Fig. 6.5). The WDX – analysis with standards shows a good agreement between the expected and measured stoichiometric proportions (Tab. 6.1).
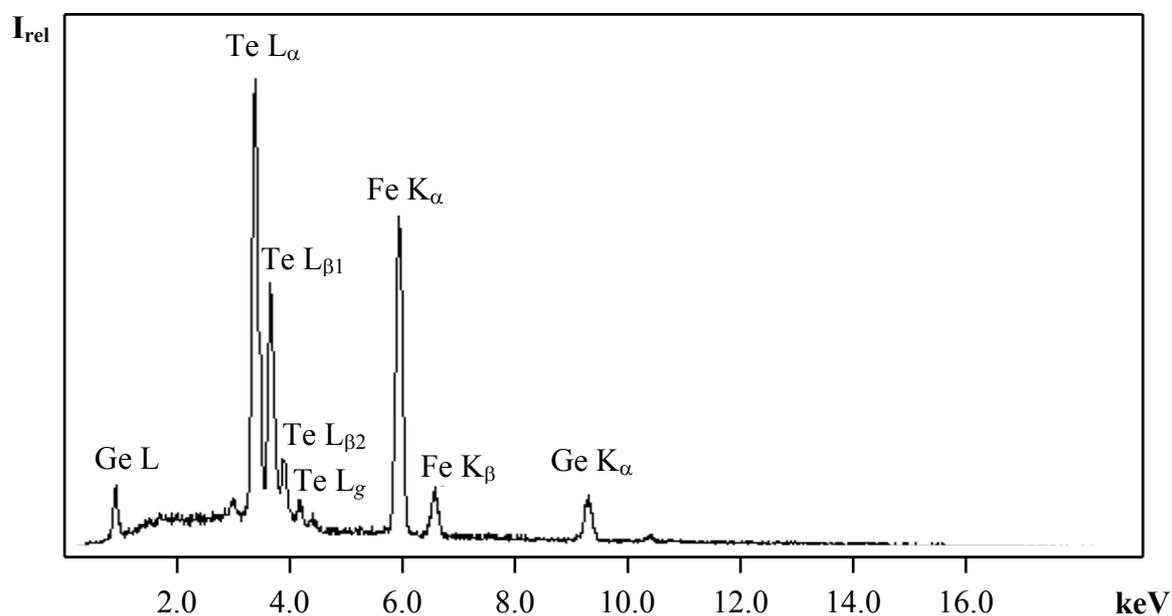
Fig. 6.5: EDX – spectra of Fe_3GeTe_2

Table 6.1: Result of the WDX analysis with standards in comparison to the expected values for Fe_3GeTe_2

Element	Measured / atom %	Expected / atom %
Fe	50.30	50.00
Ge	16.16	16.67
Te	33.54	33.33

6.2.3 Single crystal analysis

Under a light microscope, a thin hexagonal platelet was selected. It was mounted on a goniometric head and analysed with a single – crystal diffractometer. The most important structure refinement parameters and crystallographic data are summarised in Table 6.2.

Table 6.2: Crystallographic data and structure refinement parameters for Fe_3GeTe_2

Formula	Fe_3GeTe_2
Temperature	293(2) K
Molecular weight	$M = 495.34$ g/mol
Crystal system	hexagonal
Space group	$P6_3/mmc$ (No. 194)
Cell dimensions	$a = 399.1(1)$ pm
	$c = 1633.6(3)$ pm
Volume	$V = 225.34(9) \times 10^6$ pm^3
Density (calculated)	$\rho = 7.3$ g/cm^3
Formula units per unit cell	$Z = 2$
Structure solution	SHELXS – 97 [18]
Structure refinement	SHELXL – 97 [19]
Diffractometer	IPDS (Stoe)
Measured θ range	$2.49° \le \theta \le 25.79°$
hkl ranges	$-4 \le h \le 4$
	$-4 \le k \le 4$
	$-20 \le l \le 20$
Absorption coefficient	$\mu = 28.552$ mm^{-1}
No. of measured reflections	1566
No. of unique reflections	113
No. of reflections ($I_0 \ge 2\sigma\,(I)$)	112
Extinction coefficient	$\varepsilon = 0.069(7)$
$\Delta\rho_{min}$ / $\Delta\rho_{max}$ / e/pm$^3 \times 10^{-6}$	-1.944 / 1.584
R_1 / wR_2 ($I_0 \ge 2\sigma\,(I)$)	0.0328 / 0.0731
R_1 / wR_2 (All data)	0.0330 / 0.0731
Goodness – of – Fit on F^2	1.547

The quality factor values after the last refinement cycle are R_1 = 0.0328, respectively wR_2 = 0.0731 (112 reflexes with $I_0 \geq 2\sigma$ (I)). The refinement is realized by the "least – squares" method. The positions of the atoms, Wyckoff notations, their equivalent isotropic displacement parameters and occupancies are listed in Table 6.3. The anisotropic thermal displacement parameters are given in Table 11.10 in the Appendix.

Table 6.3: Atomic coordinates, Wyckoff notations, occupancies and isotropic displacement parameters for Fe₃GeTe₂

Atom	Wyck.	x	y	z	*sof.*	$U_{eq} \times 10^4$ / pm²
Fe1	*4e*	0	0	0.6718(1)	1	0.009(1)
Fe2	*2c*	⅔	⅓	¾	0.83(2)	0.008(2)
Ge	*2d*	⅓	⅔	¾	0.99(2)	0.021(1)
Te	*4f*	⅔	⅓	0.5918(6)	1	0.0096(7)

The equivalent isotropic atom displacement parameters U_{eq} are calculated as one third of the orthogonal tensors U_{ij}.

6.2.4 Structure description and discussion

Fe₃GeTe₂ has a hexagonal symmetry and crystallizes in space group *P6₃/mmc* (*a = 399.1(1) pm, c = 1633.6(3) pm*). Its structure consists of layer packages, which alternate perpendicular to [001]. Each layer package is built of five layers. The first layer formed by Te atoms is followed by a layer of Fe atoms. The third layer is mixed, formed by Fe and Ge atoms. It is followed by another Fe layer. The fifth layer, which completes the package is built again by Te. Different layer packages are separated by a van der Waals gap ($d_{Te – Te}$ = 374.0(1) pm) and are shifted one to another (Fig 6.6). Such an atom arrangement defines two positions for the iron atoms. Fe1 is located at *4e* (all iron atoms from the pure iron layers) and Fe2 is located at *2c* (all iron atoms from the mixed Fe – Ge layers).

The layer sequence within each layer package is represented in Fig. 6.7. The layers consisting of only tellurium or iron atoms respectively, have two times less atoms than the mixed layer built of iron and germanium. The pure iron layer is shifted compared to the tellurium one. Thus, the arrangement of the packages is ABAB.
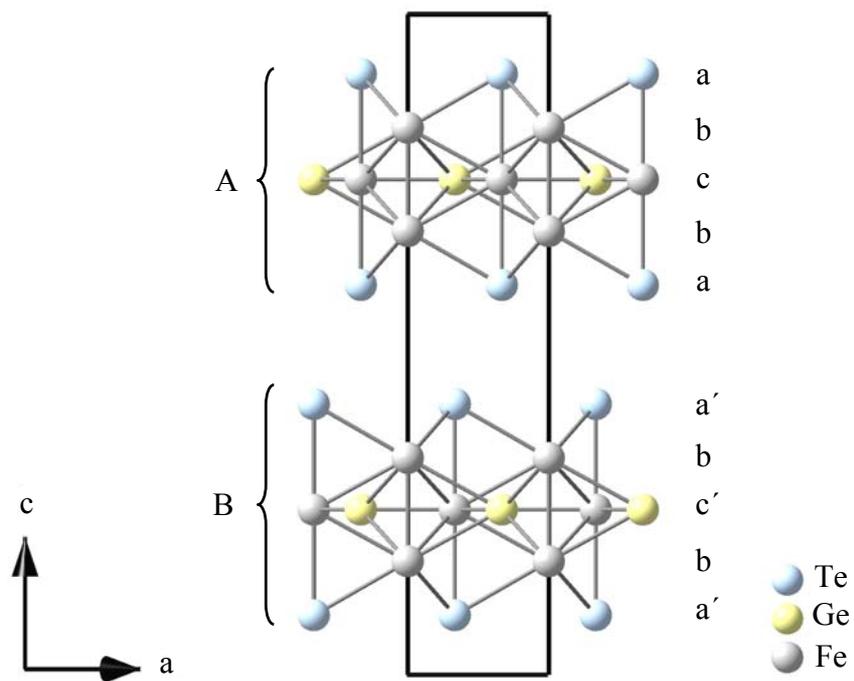
Fig. 6.6: Projection of the structure of Fe₃GeTe₂ along [010]
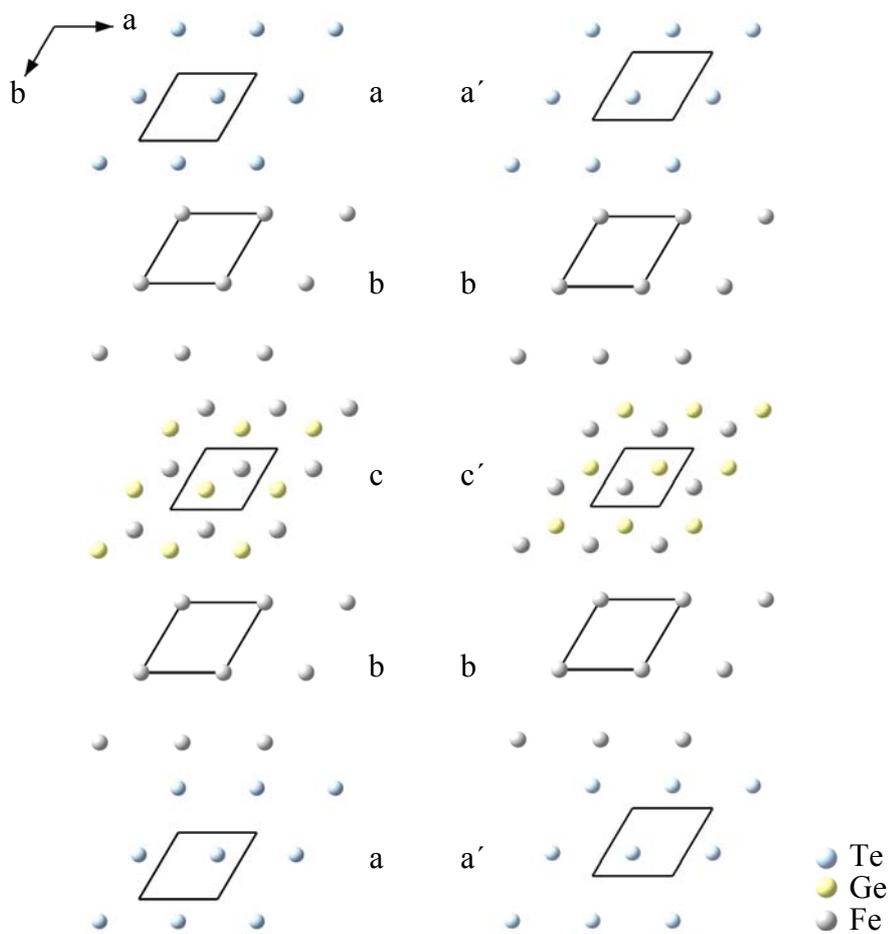
Fig. 6.7: Ordering of the different layers within each layer package

The mixed layer of Fe and Ge is ordered in such a way, that on the top of each hole of the closely packed iron layer (layer *b*) an atom from the mixed layer is located. As a result the iron atoms from the mixed layer (layers *c* and *c′*, respectively) occupy the same positions as the atoms from the pure tellurium layer (layers *a* and *a′*, respectively). Therefore, in the mixed layer of the layer packages (A and B) the positions of the Fe and Ge atoms are exchanged.

The main interatomic distances in Fe_3GeTe_2 are listed in Table 6.4. The Fe atom at *4e* (Fe1) has a coordination number CN = 10. In its coordination polyhedron, three equally long Fe – Te and Fe – Ge distances are observed. Each of them has a length of 266.2(1) pm and 263.4(1) pm, respectively. Three of the observed four Fe – Fe distances are equal to 263.4(1) pm. The fourth one has a length of 255.4(4) pm. The Fe1 coordination polyhedron can be considered as a four capped trigonal prism (edges formed by Fe2 and Te, Fig. 6.8a).

Table 6.4: Interatomic distances / pm in Fe_3GeTe_2

Fe1 - coordination		Fe2 – coordination	
Fe1 – Fe2	263.4(1) × 3	Fe2 – Fe1	263.4(1) × 6
Fe1 – Te	266.2(1) × 3	Fe2 – Ge	230.4(6) × 3
Fe1 – Ge	263.4(1) × 3	Fe2 – Te	261.1(1) × 2
Fe1 – Fe1	255.4(4)		
Ge – coordination			
Ge – Fe1	263.4(1) × 6		
Ge – Fe2	230.4(6) × 3		

The Fe atom located at *2c* (Fe2) is surrounded by six Fe1 atoms, three Ge and two Te atoms, giving a coordination number, CN = 11. The six Fe – Fe distances are all equal to 263.4(1) pm. All Fe – Ge distances have a length of 230.4(6) pm. The Fe – Te distance are 261.1(1) pm long. The atoms surrounding the Fe2 atom form a five capped trigonal prism (edges built by Fe1, Fig. 6.8b).

Germanium, which occupies position *2d*, is surrounded by nine iron atoms. The Ge – Fe distances vary between 230.4(6) pm and 263.4(1) pm. Its coordination polyhedron can be seen as a three capped trigonal prism (edges built by Fe1, Fig. 6.8c).

The Fe – Ge distances observed in Fe_3GeTe_2 correspond well with the distances observed in the monoclinic FeGe (d_{Fe-Ge} = 231.1(4) pm ÷ 264.6(3) pm) [68].

Tellurium is connected to four iron atoms (Fig. 6.8d). The Fe – Te distances (mean value ~ 265 pm) are longer than the corresponding values of the Fe – Te distances in FeTe ($d_{Fe – Te}$ = 261.5 pm) [71], which has NiAs – type [80] crystal structure.
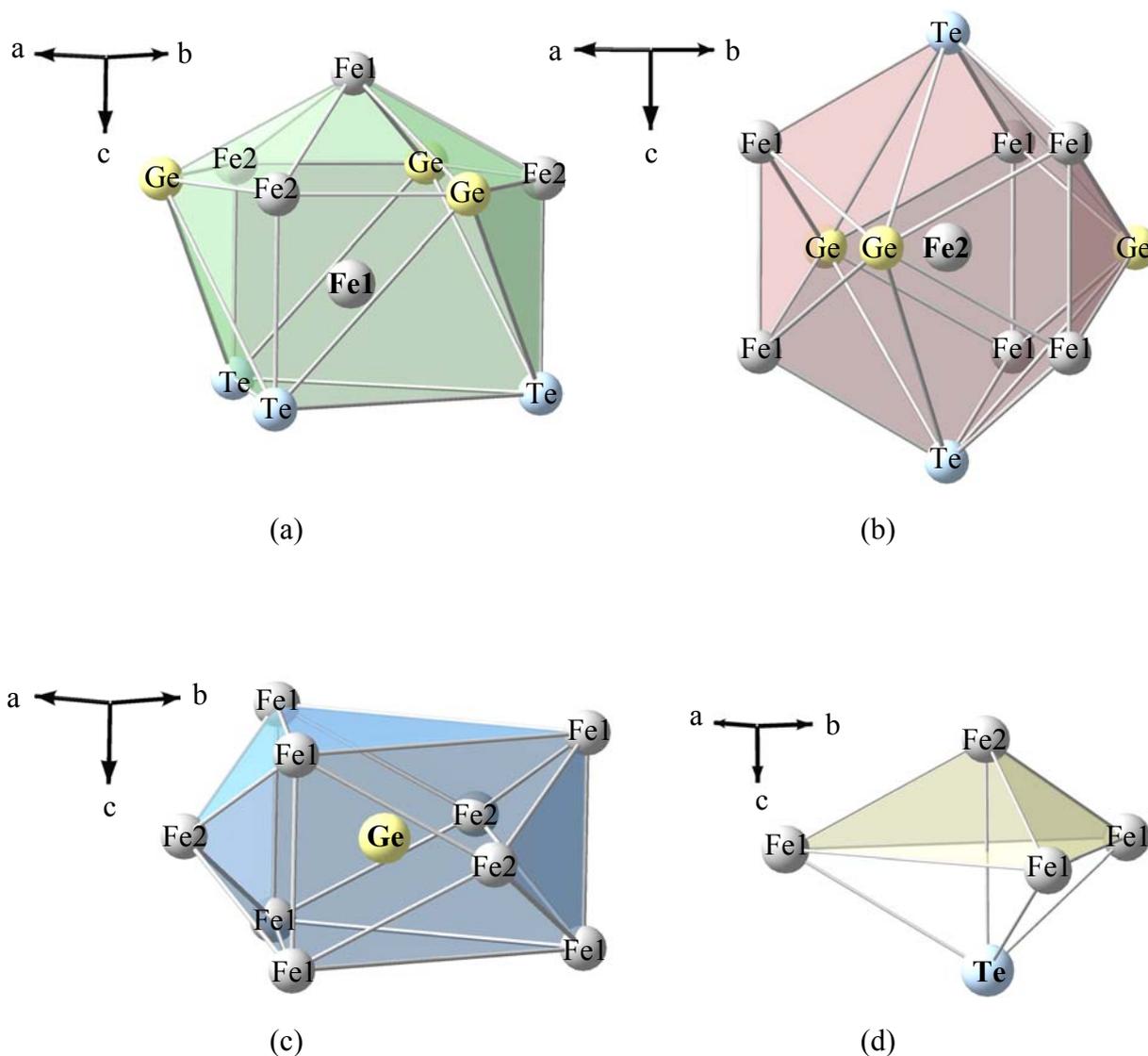
Fig. 6.8: Coordination polyhedra in Fe₃GeTe₂. Fe1 (a), Fe2 (b), Ge (c) and Te (d)

The Fe – Fe and Fe – Ge distances observed in Fe₃GeTe₂ are in a surprisingly good agreement with the relevant distances observed in the intermetallic phase Fe$_{1,67}$Ge [64]. This is a result of the close structural relation between these compounds. As Fe₃GeTe₂, Fe$_{1,67}$Ge has a hexagonal symmetry and crystallizes in the same space group, *P6₃/mmc*. The *a* – lattice constants of both compounds are essentially equal (Tab. 6.5).

Table 6.5: Comparison between the lattice parameters of Fe_3GeTe_2 and $Fe_{1,67}Ge$

Compound	SG	a / pm	c / pm	γ / °
Fe_3GeTe_2	*P6₃/mmc*	399.1(1)	1633.6(3)	120
$Fe_{1,67}Ge$	*P6₃/mmc*	402.1	502.7	120

In $Fe_{1,67}Ge$, similar to Fe_3GeTe_2, pure Fe- and mixed layers, two times denser layers built up of Fe and Ge are observed (Fig. 6.9). Compounds of this type are considered as a filled NiAs structures. The Fe atoms from the mixed layer form a hexagonal close packing in which the Fe atoms from the pure Fe – layer occupy the octahedral holes. Ge atoms occupy quasi trigonal holes.

(a)   (b)   (c)
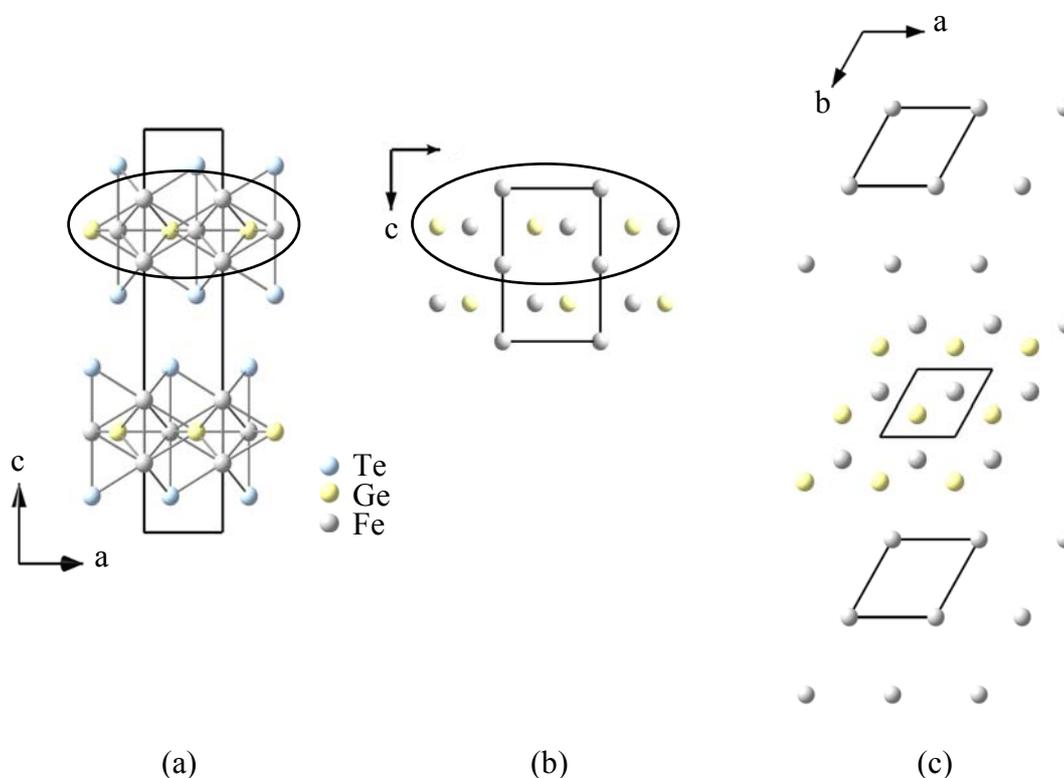
Fig. 6.9: Comparison between the structures of Fe_3GeTe_2 (a) and $Fe_{1,67}Ge$ (b), and the layer sequence within the marked area (c)

In Fe_3GeTe_2 the iron position in the mixed layer (Fe2) is not fully occupied (see Tab. 6.3). The same is reported for $Fe_{1,67}Ge$ [64]. The occupations are 0.83 for Fe_3GeTe_2 and 0.67 for $Fe_{1,67}Ge$ [64, 74], respectively. The Fe2 occupancy factor observed in Fe_3GeTe_2 causes a conflict with the chemical composition determined by the WDX – analysis. Since it reaches

an accuracy of ~ 1 At% [81], a mistake in the determined chemical composition of Fe_3GeTe_2 has to be excluded.

The computer evaluation of the data from the data collection in some cases suggested a doubling of the lattice constants of Fe_3GeTe_2. Consequently, the axes lengths of the new cell were as follows: *a = b = 798.2(1) pm, c = 3267.2(3) pm*. It was assumed that this doubling is related to the partly occupied position of the iron atom (Fe2) in the mixed Fe – Ge layer. In order to clarify this some precession simulations of the doubled cell have been made (Fig. 6.10).

In the investigated sections of the structure and among the main reflections additional, significantly weaker reflections are also observed. The appearance of the interstitial reflections could be related to the existence of a superstructure or some stacking fault in the structure. However, thorough analysis of the observed reflections revealed the so – called *λ/2* effect.

Thus, in the *0kl* layer (Fig. 6.10) the (016) reflection has a *λ/2* reflection with indices (00.53). Consequently, the distance from the centre to the point showing (016) (in reciprocal space a set of planes is represented by a single point) is twice the distance from the centre to (00.53). Similarly, in the *h0l* layer the ($30\bar{6}$) and ($\bar{3}00$) reflections have *λ/2* reflections with the indices ($1.50\bar{3}$) and ($\bar{1}.\overline{5}00$), respectively. In addition, the distances from the centre to the ($30\bar{6}$) and ($\bar{3}00$), respectively are two times longer than the distances between the centre and the corresponding *λ/2* reflection.

Analogously the same could be applied to the pairs of reflections (300), (1.500) and (030), (01.50) observed in the *hk0* layer, as also for many other pairs of reflections observed in the precession images shown on the picture.

Appropriate magnification of the studied sections (Fig. 6.10) shows cross – like form for many of the main reflections. This is partly due to the mosaic structure [12] of the investigated crystal (direction A on the picture) and partly to the existence of powdered fractions inside it (marked as direction B). Elongation in one of the cross directions observed for many reflections could be explained with small variations in the lengths of the elementary cell axes, i. e some disorder exists. This could be already caused by the not fully occupied iron position (Fe2) (in some cells the iron atom is presented in some is missing), but in general the question of its influence on the Fe_3GeTe_2 structure remains open.
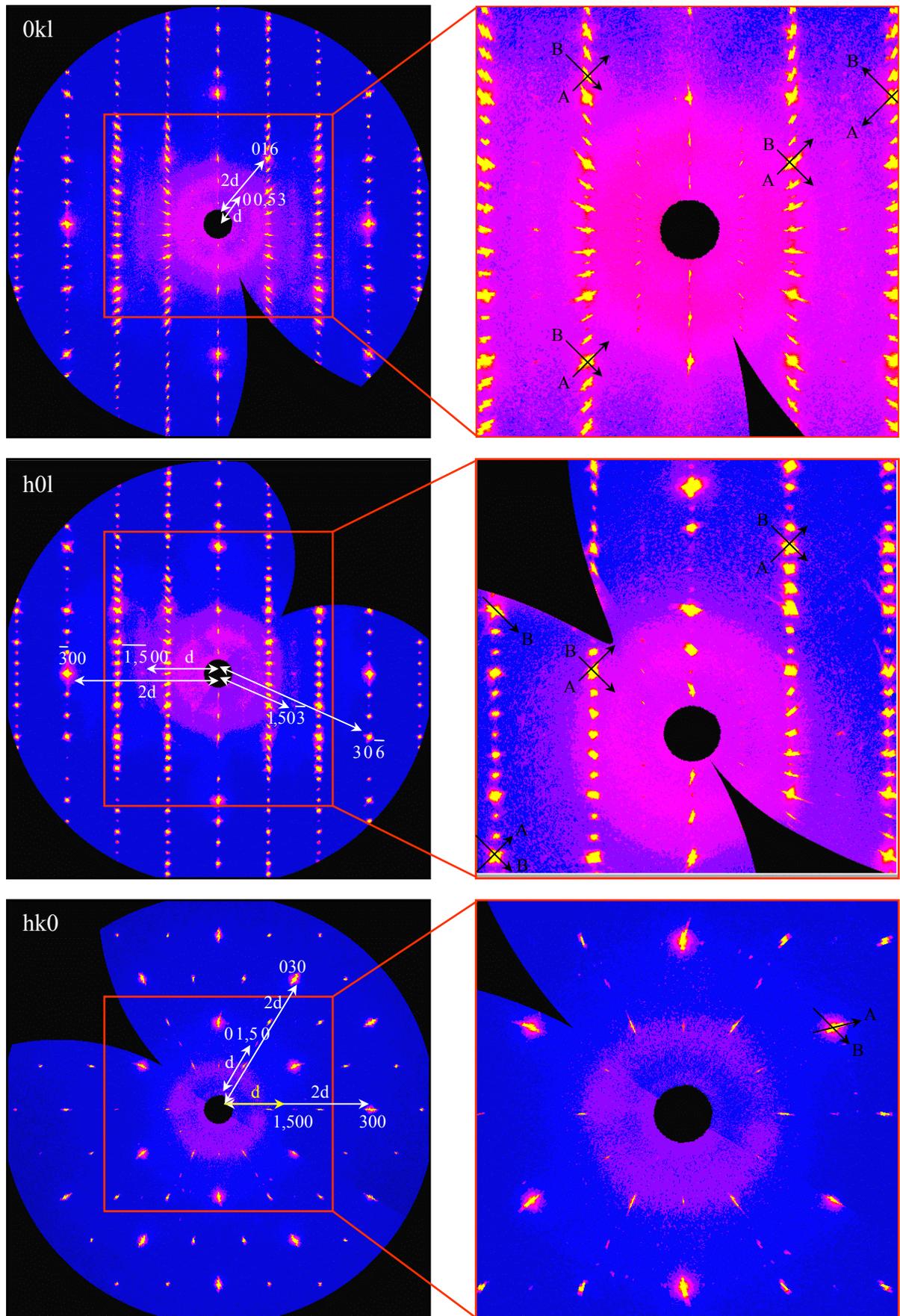
Fig. 6.10: Simulated precession images of the *0kl*, *h0l* and *hk0* layer of the doubled cell of Fe₃GeTe₂

6.2.5 Magnetic measurements

The study of the magnetic properties of Fe_3GeTe_2 started with a simple test of its magnetic behaviour. For the target, at room temperature a piece of Co – magnet with a circular form was moved slowly towards crystals of the compound. At a distance of approximately 1cm the crystals were attracted by the magnet and stuck on its surface. This observation suggested ferromagnetic behaviour of Fe_3GeTe_2.

To prove or eventually to reject this, magnetic measurements with a SQUID – magnetometer were carried out by Dr. R. K. Kremer at the Max – Planck – Institute for Solid State Research, Stuttgart. Powder samples of Fe_3GeTe_2 have been investigated in the temperature range from 5K to 350K. For determining the dependence of the magnetic susceptibility from the magnetic field, different fields have been applied.

Fig. 6.11 represents the inverse magnetic susceptibility measured at strength field 100 Oe and 50000 Oe, after cooling under zero field (ZFC).
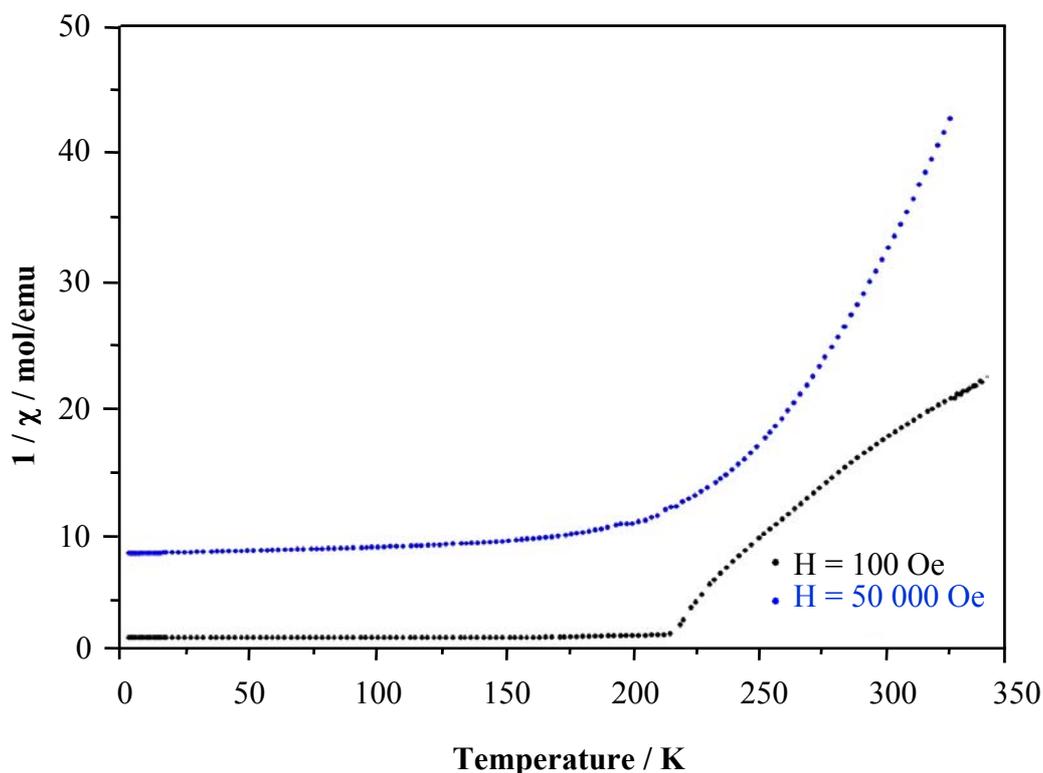
Fig. 6.11: Inverse magnetic susceptibility of Fe_3GeTe_2 as a function of the temperature

At high temperatures (T > 250 K) and strong external field the curve has a general behaviour, following the Curie – Weiss law, $1/\chi = (T – \Theta)/C$ with a paramagnetic Curie temperature

T_c=231K. This indicates a predominance of ferromagnetic interactions. The inverse magnetic susceptibility curve measured at an applied magnetic filed of 100 Oe (the black one) departs form the Curie – Weiss law at temperatures well above 300K. This is probably due to the domain structure of the ferromagnetic materials and the curve follows the trend observed in many other ferromagnetic compounds [3]. Application of very strong external field (5×10^4 Oe) causes full saturation of the compound and at temperatures above T_c the curve (outlined with blue) follows strictly the Curie – Weiss law. The Curie constant C, has a value of 5.87 emu/mol K, which corresponds to an effective magnetic moment $\mu_{eff} = 6.86$ μ_{Bohr}. The effective magnetic moment is calculated using the expression:

$$\mu_{eff} = 2.83\sqrt{C}$$

Fe_3GeTe_2 is considered a mixed valence iron germanide:

$$Fe_3GeTe_2 = (Fe^{3+})_2Fe^{2+}Ge^{4-}(Te^{2-})_2$$
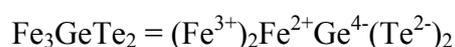
It is assumed high spin configuration of Fe^{3+} (*3d⁵, S = 5/2*) and low spin configuration of Fe^{2+}(*3d⁶, S = 0*). The calculated overall magnetic moment of Fe_3GeTe_2 is:

$$\mu = g\sqrt{S(S+1)} = 5.92\mu_{Bohr} \qquad \text{where, } g\sim2 \text{ is the gyromagnetic ratio}$$

This value differs significantly from the value of the effective magnetic moment determined experimentally, but up to now this discrepancy couldn't be explained.

At temperatures lower than 250K a deviation from the Curie – Weiss law is observed. A relative sharp change in the curve's behaviour is observed at 231K. Below this temperature $1/\chi$ continues to decrease before levelling off close to 0K. This corresponds to a ferromagnetically ordered compound, which is saturated when high field is applied. Accordingly, the shift in the $1/\chi$ behaviour is not so sharp at the higher field.

The Curie temperature determined from the susceptibility measurements, $T_c = 231K$ is significantly lower than the room temperature (293K). Obviously there is a conflict between the result from the preliminary test of the magnetic properties and the results from the magnetic measurements. This apparent disagreement is readily explained by the theory of paramagnetism [3]. Above the Curie temperature some spontaneous magnetization in Fe_3GeTe_2 continues to exist in small, but macroscopic ranges throughout it called domains, according to the domain structure of the ferromagnets [82, 83]. Within each domain the magnetic moments are aligned parallel, but since different domains have random orientation, above the Curie temperature the compound behaves as a paramagnet When placed in an external field (created by the Co – magnet) the number of lines of force passing through it is greater, than would pass through a vacuum. Consequently, all spins (all domains) align in the direction of the external field and the compound is attracted by it.

6.3 The compound Ni₃GeTe₂

6.3.1 Preparation and properties

Ni₃GeTe₂ was synthesised by a solid – state reaction. For this purpose powders of the pure elements in stoichiometric proportions (Ni : Ge : Te = 3 : 1 : 2) were mixed for several minutes in an agate mortar. The prepared sample was put into a quartz glass ampoule. Subsequently it was evacuated and sealed. The ampoule was heated in a furnace with a heating rate of 50°C/h until the desired temperature of 625°C was reached. After annealing period of two weeks the furnace was cooled down to room temperature. The resulting product was a homogeneous dark – grey powder. It is water and air stable.

In order to get crystals of Ni₃GeTe₂, from stoichiometric mixture of the elements a pellet was prepared. It was put in a quartz ampoule, which was evacuated and sealed. The ampoule was heated up to 850°C in a furnace with a heating rate of 50°C/h. After an annealing for 14 days the furnace was cooled down to room temperature with a cooling rate of 5°C/h. The resulting bulk was dark – grey, composed of many fine platelets with a hexagonal form (Fig. 6.12). The crystals are water stable and not air sensitive. In general they were noticeably smaller than the observed crystals of Fe₃GeTe₂.
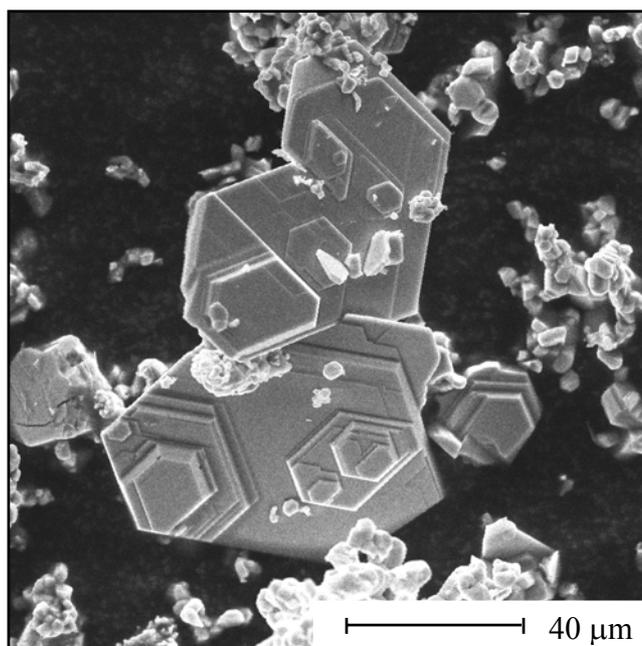
Fig. 6.12: Crystals of Ni₃GeTe₂

The thermal behaviour of Ni_3GeTe_2 was investigated by **D**ifferential **T**hermal **A**nalysis (DTA). The DTA curve is represented in Fig. 6.13.
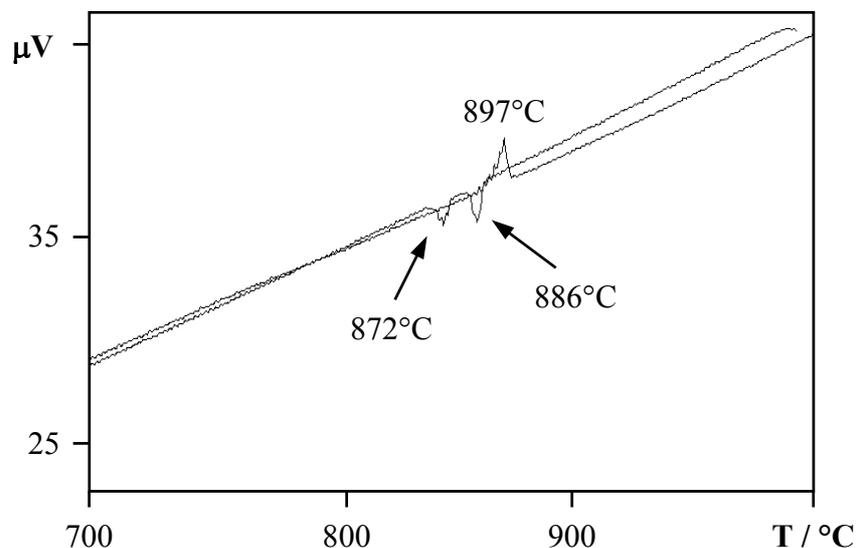
Fig. 6.13: DTA curve of Ni_3GeTe_2. The heating curve shows one endothermic effect at 897°C. Upon cooling two endothermic effects at 886°C and 872°C, respectively are observed

An endothermic effect endothermic effect appears at 897°C in the heating curve. Upon cooling two thermal effects at 886°C and 872°C, respectively are observed. This suggests thermal decomposition of the compound.

To clarify this problem the substance was investigated using X – ray powder diffractometry after the thermal analysis was carried out. In the measured pattern along with the reflections of Ni_3GeTe_2 additional reflections are also observed (Fig. 6.14). They belong to NiTe and Ni, respectively, i. e. Ni_3GeTe_2 decomposes upon heating. The exothermic effect at 886°C then shows the solidification point of Ni_3GeTe_2. The second exothermic effect at 872°C observed in the DTA curve marks the solidification temperature of NiTe (melting point ∼ 870°C [84]).

The DTA experiment was carried out only up to a temperature of 1000°C. That is why the thermal effects of Ni, which melts at 1455°C [85] are not observed in the DTA curve. Thus, Ni_3GeTe_2 is suggested to decompose by one of the two schemes:

$$1.)\ Ni_3GeTe_2 \rightarrow 2NiTe + Ni + Ge$$

$$2.)\ Ni_3GeTe_2 \rightarrow NiTe + 2Ni + GeTe$$
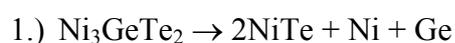
The presence of Ge or GeTe, respectively in the X – ray powder pattern of the DTA sample could not be detected. Furthermore, despite that Ge melts at 937°C [85] and GeTe melts at 725°C [85], their thermal effects are not observed in the DTA curve. Up to now a meaningful explanation of this discrepancy could not be presented.
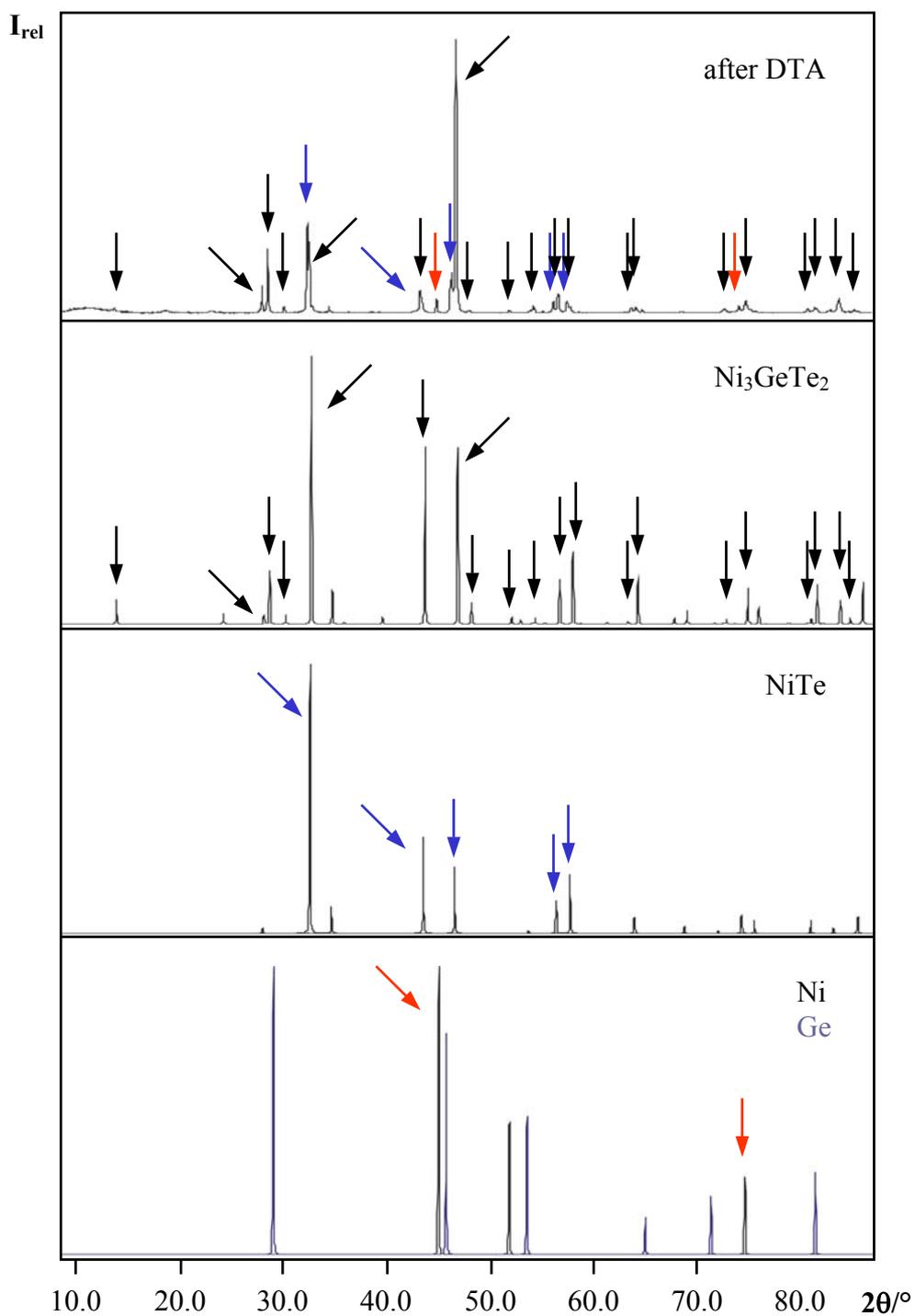
Fig. 6.14: Comparison between the measured powder pattern of "Ni₃GeTe₂" after the DTA experiment (top) and the calculated patterns of Ni₃GeTe₂, NiTe, Ni and Ge

6.3.2 Characterization

In Fig. 6.15 is represented a comparison between the X – ray powder pattern of polycrystalline sample of Ni_3GeTe_2 and the calculated pattern obtained from the structure refinement. The positions and the intensities of the reflections in the experimental pattern correspond very well to those of the theoretical one. No reflections from impurities are observed.

Indexing of all reflections resulted in a hexagonal cell. The lattice constants of Ni_3GeTe_2 are smaller than those of Fe_3GeTe_2 (Tab. 6.6).

A list of the observed reflections for Ni_3GeTe_2 is given in table 11.11 (see App.).
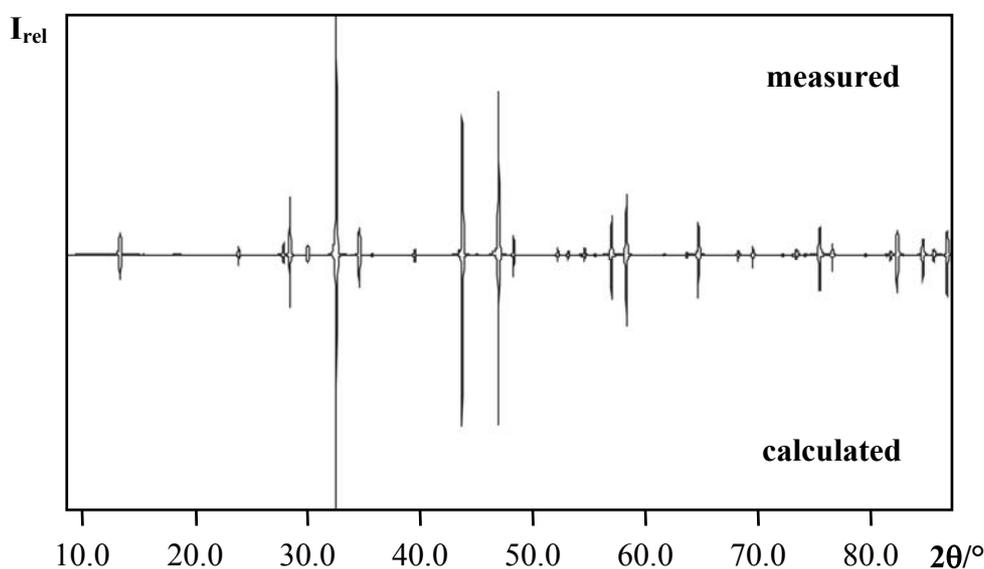
Fig. 6.15: Comparison between the measured powder pattern (top) of Ni_3GeTe_2 and the calculated one (bottom)

Table 6.6: Comparison between the lattice constants and volumes of Fe_3GeTe_2 and Ni_3GeTe_2 obtained from powder data

Compound	a / pm	c / pm	γ / °	V × 10⁶ / pm³
Fe_3GeTe_2	401.59(3)	1633.04(1)	120	228.08(3)
Ni_3GeTe_2	389.90(2)	1603.45(5)	120	221.10(2)

The chemical composition of the crystals was analysed in addition with an analytical scanning electron microscope (Fig. 6.16). The WDX – analysis with standards shows no significant difference between the expected and measured stoichiometric proportions (Tab. 6.7).

Table 6.7: Result of the WDX analysis with standards in comparison to the expected values for the composition Ni_3GeTe_2

Element	Measured / atom %	Expected / atom %
Ni	50.34	50.00
Ge	15.95	16.67
Te	33.71	33.33
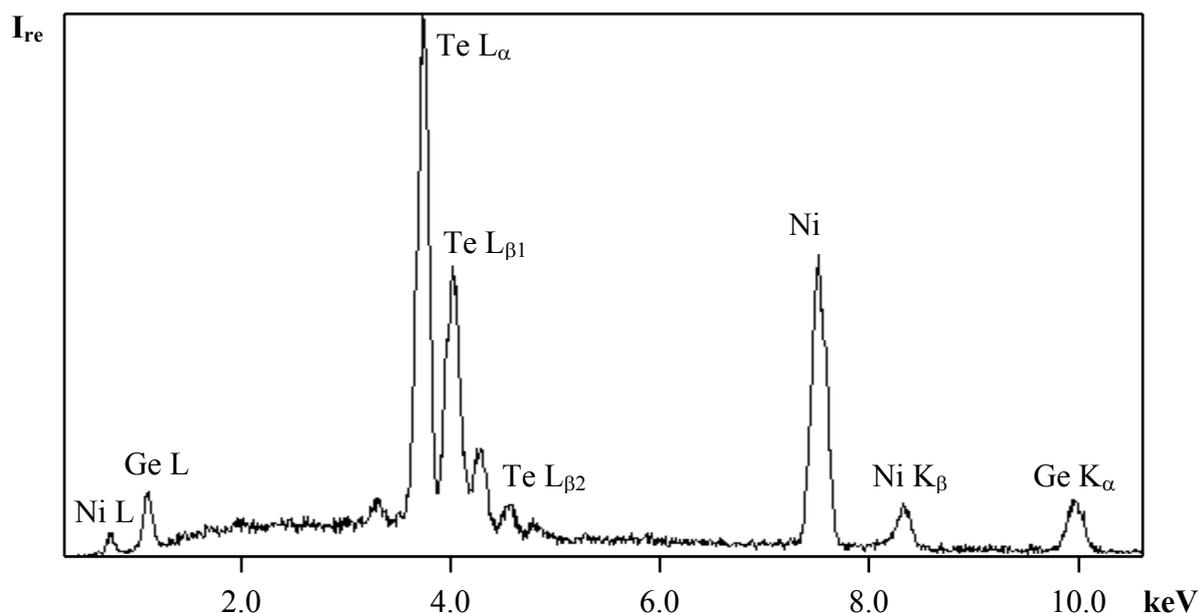
Fig. 6.16 : EDX – spectra of Ni_3GeTe_2

A possible phase transitions of Ni_3GeTe_2 at high temperatures was investigated. The X – ray powder patterns were measured at different temperatures. Fig. 6.17 shows a comparison between the calculated pattern of Ni_3GeTe_2 and the patterns of samples measured at room temperature, 400°C, 600°C and 800°C.
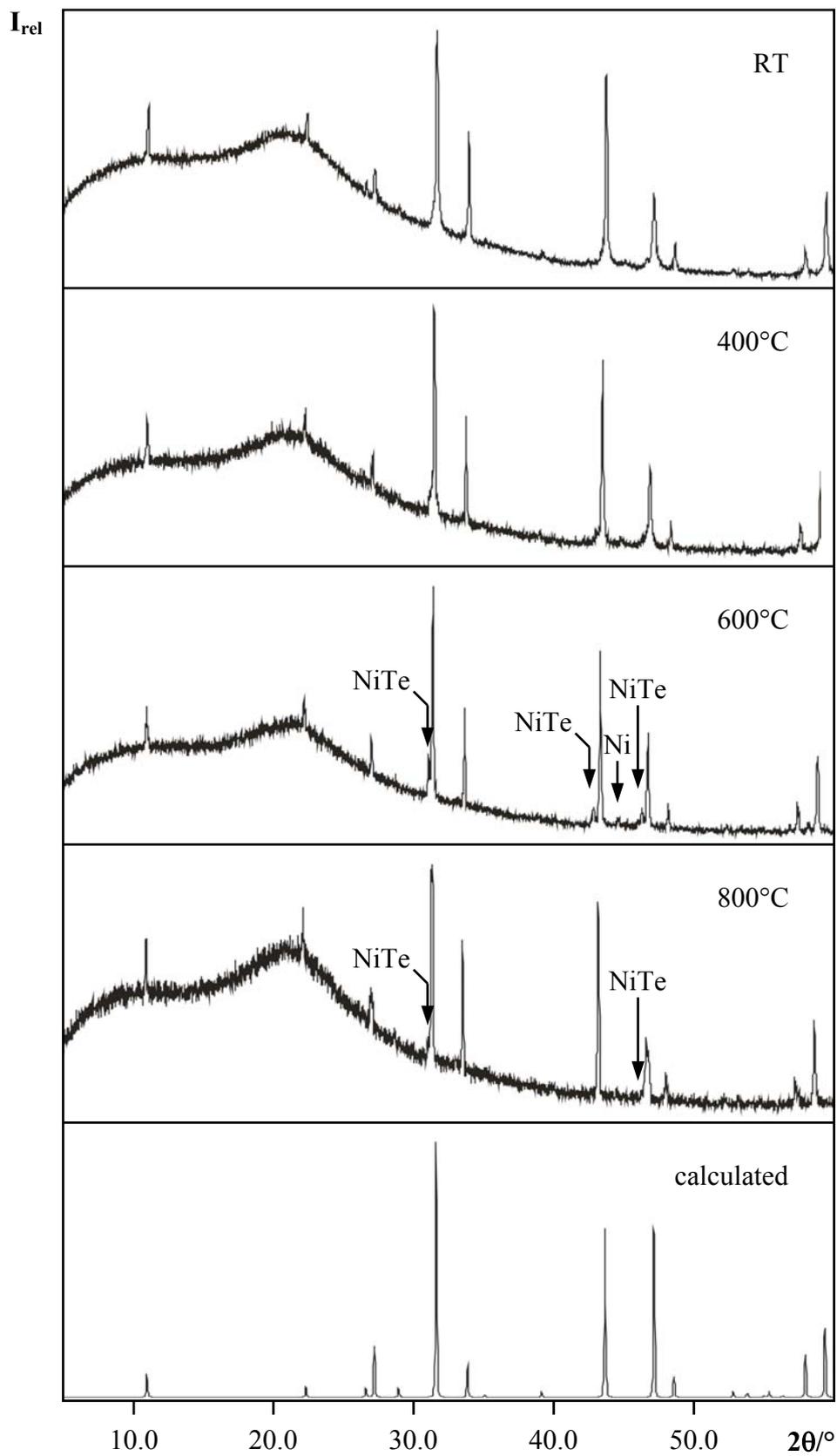
Fig. 6.17: Comparison between the calculated pattern of Ni_3GeTe_2 and the patterns measured at different temperatures

The X – ray powder patterns measured at high temperatures are shifted to lower *2θ* angles compared to the pattern measured at room temperature. This indicates only thermal expansion, but no phase transition. The expansion is more significant when the temperature is changed directly from room temperature to 400°C. This explains the more significant shift in the powder pattern measured at this temperature. Further increase of the temperature leads to a smaller change in the lattice constants of Ni_3GeTe_2. Indexing of the patterns proves this fact (Tab. 6.8). The unit cell volume depends almost linearly on the temperature (Fig 6.18).

In the patterns measured at high temperatures, a "splitting" of some reflections and additional reflections are observed. They are indexed as NiTe. This implies the beginning of the thermal decomposition already at 700°C (the DTA investigation showed thermal decomposition at about 900°C). Another reason could be the crystallization of NiTe, which was already present, but in an amorphous state. The reflections observed for Ni_3GeTe_2 at 400°C, 600°C and 800°C are given in Tab. 11.12 – 11.14 (see App.).

Table 6.8: Comparison between the lattice constants and volumes of Ni_3GeTe_2 obtained by the cell refinement of the powder diffraction data measured at different temperatures

Temperature / °C	a / pm	b / pm	c / pm	$V \times 10^6$ / pm^3
25	390.47(7)	390.47(7)	1602.0(2)	211.52(7)
400	392.76(7)	392.76(7)	1611.8(2)	215.33(7)
600	393.96(6)	393.96(6)	1617.5(2)	217.41(6)
800	395.2(3)	395.2(3)	1626.0(1)	219.9(3)
Δ %	1.20	1.20	1.49	3.90
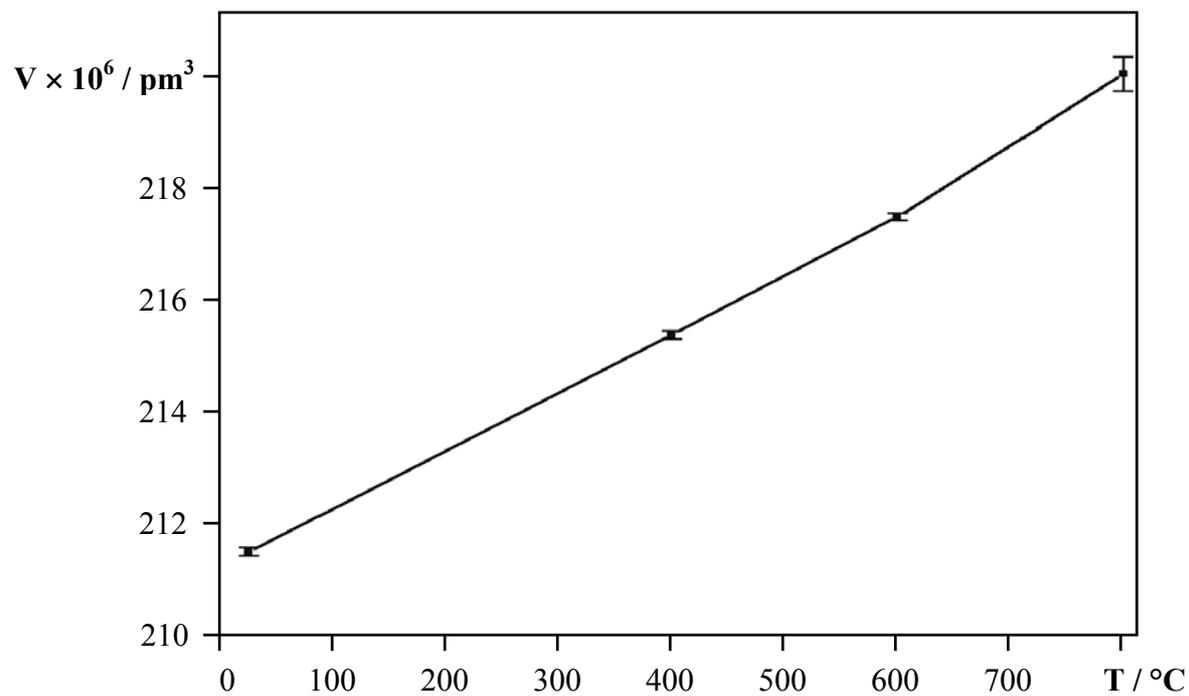
Fig. 6.18: The temperature dependence of Ni₃GeTe₂ unit cell volume

6.3.3 Single crystal analysis

For the single crystal analysis, under a light microscope, a crystal in the form of a thin hexagonal platelet was selected and fixed at the top of a glass capillary. The most important structure refinement and crystallographic data are summarised in Table 6.9.

Table 6.9: Crystallographic data and structure refinement parameters for Ni_3GeTe_2

Formula	Ni_3GeTe_2
Temperature	293(2) K
Molecular weight	$M = 503.92$ g/mol
Crystal system	hexagonal
Space group	$P6_3/mmc$ (No. 194)
Cell dimensions	$a = 391.1(1)$ pm
	$c = 1602.2(3)$ pm
Volume	$V = 212.24(9) \times 10^6$ pm^3
Density (calculated)	$\rho = 7.885$ g/cm^3
Formula units per unit cell	$Z = 2$
Structure solution	SHELXS – 97 [18]
Structure refinement	SHELXL – 97 [19]
Diffractometer	IPDS (Stoe)
Measured θ range	$6.02° \leq \theta \leq 30.30°$
hkl ranges	$-4 \leq h \leq 5$
	$-5 \leq k \leq 5$
	$-22 \leq l \leq 17$
Absorption coefficient	$\mu = 33.368$ mm^{-1}
No. of measured reflections	1182
No. of unique reflections	156
No. of reflections ($I_0 \geq 2\sigma (I)$)	120
Extinction coefficient	$\varepsilon = 0.012(2)$
$\Delta\rho_{min}$ / $\Delta\rho_{max}$ / e/pm$^3 \times 10^{-6}$	-2.190 / 3.617
R_1 / wR_2 ($I_0 \geq 2\sigma$ (I))	0.0509 / 0.1226
R_1 / wR_2 (All data)	0.0613 / 0.1266
Goodness – of – Fit on F^2	1.133

The quality factor values after the last refinement cycle are $R_1 = 0.0509$, respectively $wR_2 = 0.1226$ (120 reflexes with $I_0 \geq 2\sigma\,(I)$). The refinement is carried out with the "least – squares" method. The positions of the atoms, Wyckoff notations, their equivalent isotropic displacement parameters and occupancies are listed in Table 6.10. The anisotropic thermal displacement parameters are given in Table 11.15 in the Appendix.

Table 6.10: Atomic coordinates, Wyckoff notations, occupancies and isotropic displacement parameters for Ni$_3$GeTe$_2$

Atom	Wyck.	*x*	*y*	*z*	*sof.*	$U_{eq} \times 10^4$ / pm^2
Ni1	*4e*	0	0	0.66710(8)	1	0.0106(3)
Ni2	*2c*	⅔	⅓	¾	0.73	0.0102(6)
Ni3	*2a*	0	0	½	0.30	0.024(2)
Ge	*2d*	⅓	⅔	¾	0.99	0.0219(4)
Te	*4f*	⅔	⅓	0.58847(4)	1	0.0085(2)

The equivalent isotropic atom displacement parameters U_{eq} are calculated as one third of the orthogonal tensors U_{ij}.

6.3.4 Structure description and discussion

The structures of Ni$_3$GeTe$_2$ and Fe$_3$GeTe$_2$ are closely related, but not similar. Ni$_3$GeTe$_2$ has a hexagonal symmetry and crystallizes in the same space group as Fe$_3$GeTe$_2$, *P6$_3$/mmc* (*a=391.1(1) pm, c = 1602.2(3) pm*). Accordingly, its structure is build up of layer packages, which alternate perpendicular to [001]. Each layer package is formed by five layers: A layer built of tellurium another composed by nickel atoms, a third mixed layer built of nickel and germanium and another nickel layer. The fifth layer composed again of tellurium completes the layer package (Fig. 6.19).

Despite the close structural relation between both compounds Ni$_3$GeTe$_2$ shows a significant difference in comparison with Fe$_3$GeTe$_2$. The layers found in its structure, as it was described above, are separated by a van der Waals gap. In contrast to that in Ni$_3$GeTe$_2$, an additional electron density maximum appears in the van der Waals gap which separates adjacent layer packages. It is assumed to be a Ni atom, surrounded octahedrally by tellurium (Fig. 6.19) (three atoms from the layer package above and three from the package below).

The atoms arrangement defines three positions for the Ni atoms. Ni1 located at *4e* (Ni atoms from the pure Ni layer). Ni2 located at *2c*. On this position are located all Ni atoms which take part in the formation of the mixed Ni – Ge layer. Ni3 is located at *2a*. This position is occupied by the Ni atoms located in the space (van der Waals gap), which connects the adjacent layer packages.
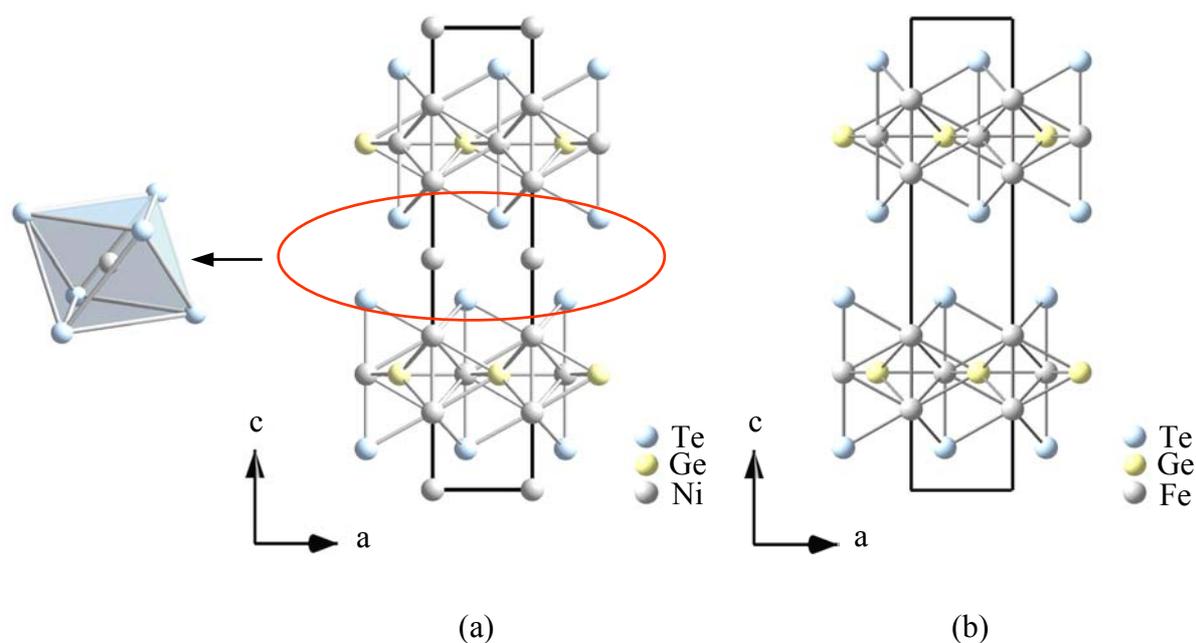
Fig. 6. 19: Comparison between the structures of Ni_3GeTe_2 (a) and Fe_3GeTe_2(b). In Ni_3GeTe_2 an additional electron density maximum appears in the space between the layer packages. It is assumed to be Ni, which occupies an octahedral hole in the van der Waals gap

The structural differences between Ni_3GeTe_2 and Fe_3GeTe_2 were first suggested investigating crystals of both compounds with a scanning electron microscope (SEM). The recorded picture images showed a crystal size up to millimetres for Fe_3GeTe_2 (Fig. 6.20a). At higher magnification, thin layers are easily recognised. In contrast, the crystals of Ni_3GeTe_2 are significantly smaller (Fig. 6.20b) and at higher magnification their habitus is much more compact compared to the crystals of the iron compound.

(a)   (b)
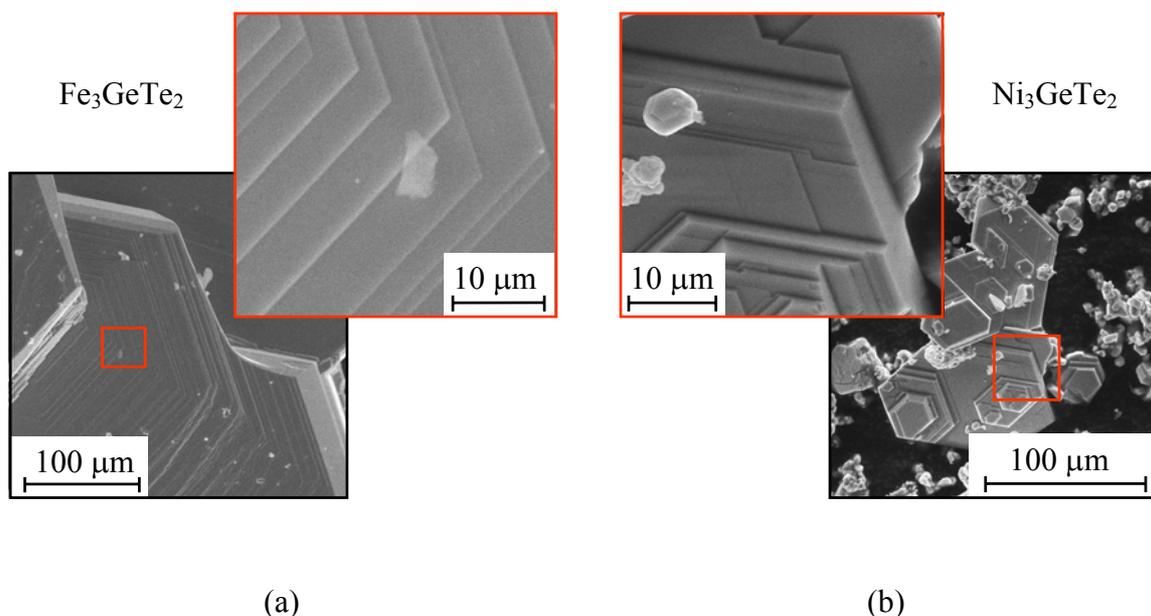
Fig. 6.20: SEM images of crystals of Fe₃GeTe₂ (a) and Ni₃GeTe₂ (b)

The main interatomic distances in Ni₃GeTe₂ are listed in Table 6.11. The Ni atom located at *4e* (Ni1) is surrounded by five Ni atoms, three Ge and three Te, giving a coordination number, CN = 11. All Ni − Ge distances have a length of 261.97(9) pm. The Ni − Te distances are 256.56(9) pm long. Three of the remaining five Ni − Ni distances are equal to 261.97(9) pm. The other two have a length of 265.7(3) pm and 267.7(1) pm, respectively. The atoms surrounding the Ni1 form five capped trigonal prism (edges built by Ni2 and Te, Fig. 6.21a).

Table 6.11: Interatomic distances / pm in Ni₃GeTe₂

Ni1 - coordination		Ni2 – coordination	
Ni1 – Ni2	261.97(9) × 3	Ni2 – Ni1	261.97(9) × 6
Ni1 – Te	258.56(9) × 3	Ni2 – Ge	225.8(6) × 3
Ni1 – Ge	261.97(9) × 3	Ni2 – Te	258.8(8) × 2
Ni1 – Ni1	265.7(3)		
Ni1 – Ni3	267.7(1)		
Ni3 - coordination		**Ge – coordination**	
Ni3 – Te	266.61(6) × 6	Ge – Ni1	261.97(9) × 6
		Ge – Ni2	225.8(6) × 3
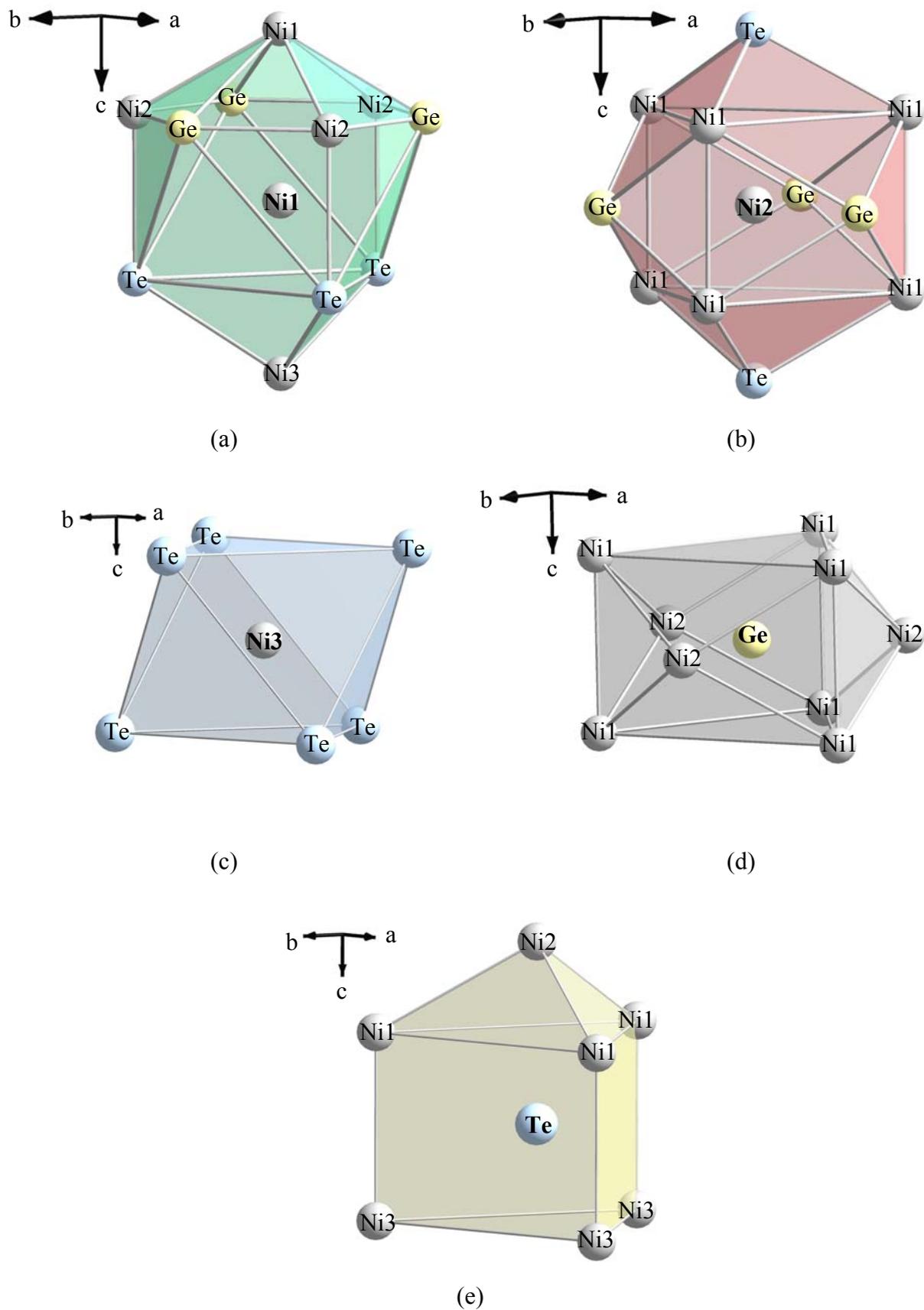
Fig. 6.21: Coordination polyhedra in Ni₃GeTe₂. Ni1 (a), Ni2 (b), Ni3 (c), Ge (d) and Te (e)

The Ni atom at *2c* (Ni2) has a coordination number, CN = 11. In its coordination polyhedron two equally long Ni – Te distances and three equally long Ni – Ge distances are observed. Each of them has a length of 258.8(8) pm and 225.8(6) pm, respectively. The six Ni – Ni distances are equal to 261.97(9) pm each. The Ni2 coordination polyhedron can be considered as a five capped trigonal prism (edges formed by Ni1, Fig. 6.21b).

The Ni atom located in the van der Waals gap, which separates two successive layer packages (Ni3 at *2a*) is surrounded octahedrally by tellurium atoms (Fig. 6.21c). The observed Ni – Te distances are all equal to 266.61(6) pm. This value is in good agreement with the length of the corresponding distances observed in the hexagonal NiTe (d_{Ni-Te} = 265 pm) [77].

Germanium (*2d*) is surrounded by nine nickel atoms, which form a three capped trigonal prism (edges built of Ni1, Fig. 6.21d).The Ge – Ni distances vary between 261.97(9) pm and 225.8(6) pm.

Tellurium is connected to seven nickel atoms, which form one capped trigonal prism (edges formed by Ni1 and Ni3, Fig. 6.21e). Due to the additional transition metal position, which appears in the van der Waals gap the coordination number of tellurium in Ni_3GeTe_2 increases to seven from four in Fe_3GeTe_2. The observed Te – Ni distances (mean value ~ 262 pm) correspond good to the Ni – Te distances observed in NiTe (d_{Ni-Te} = 265 pm) [77], which crystallises in NiAs – structure type [80].

The Ni – Ni and Ni – Ge distances observed in Ni_3GeTe_2 are very close to the corresponding distances observed in $Ni_{1,67}Ge$ [63, 71, 74, 75]. A thorough inspection of their structures reveals a surprisingly close relation. Both compounds crystallize in the same space group, *P6₃/mmc*. Their *a* – lattice constants are essentially equal (Tab. 6.12).

In $Ni_{1,67}Ge$, similar to Ni_3GeTe_2 pure Ni layers and mixed, two times denser layers made up of Ni and Ge atoms appear (Fig. 6.22). In both compounds the Ni position in the mixed layer (Ni2) is not fully occupied. The occupations are 0.67 for $Ni_{1,67}Ge$ [63, 75] and 0.73 for Ni_3GeTe_2 (see Tab. 6.10), respectively. The latter added to the occupation of the additional Ni position (0.3, see Tab.6.10) gives an occupation 1. Thus, the result of the structure refinement agrees excellently with the result obtained from the WDX investigation. Similar relations for the pair Fe_3GeTe_2 and $Fe_{1,67}Ge$ were discussed before.

Table 6.12: Comparison between the lattice parameters of Ni_3GeTe_2 and $Ni_{1,67}Ge$

Compound	SG	a / pm	b / pm	γ / °
Ni_3GeTe_2	*P6₃/mmc*	391.1(1)	1602.2(3)	120
$Ni_{1,67}Ge$	*P6₃/mmc*	391.3	506.4	120

(a)   (b)   (c)
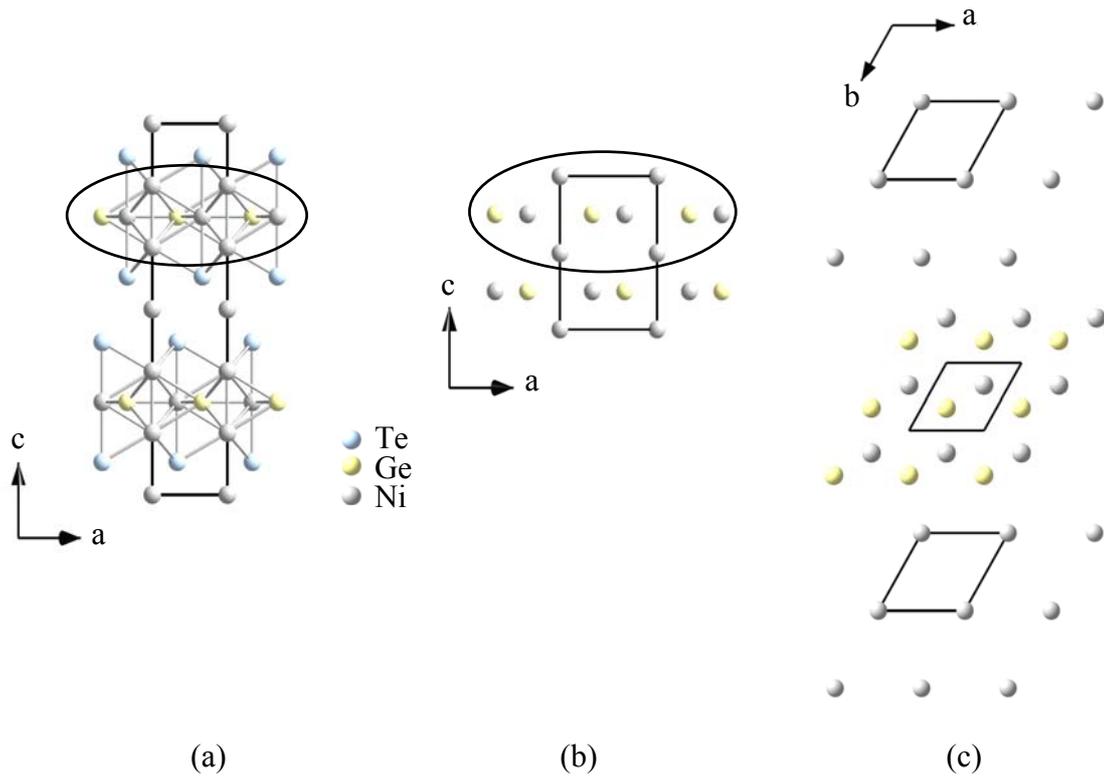
Fig. 6.22: Comparison between the structures of Ni_3GeTe_2 (a) and $Ni_{1,67}Ge$ (b). On (c) is represented the layer sequence within the marked area

6.3.5 Magnetic measurements

The magnetic measurements have been realised with a SQUID – magnetometer. Powder samples of Ni_3GeTe_2 have been investigated in the temperature range from 5K to 350K. For determining the dependence of the magnetic susceptibility from the magnetic field different, fields have been applied.

Fig. 6.23 represents the magnetic susceptibility measured at strength field 1000 Oe and 10000 Oe, after cooling under zero field (ZFC).
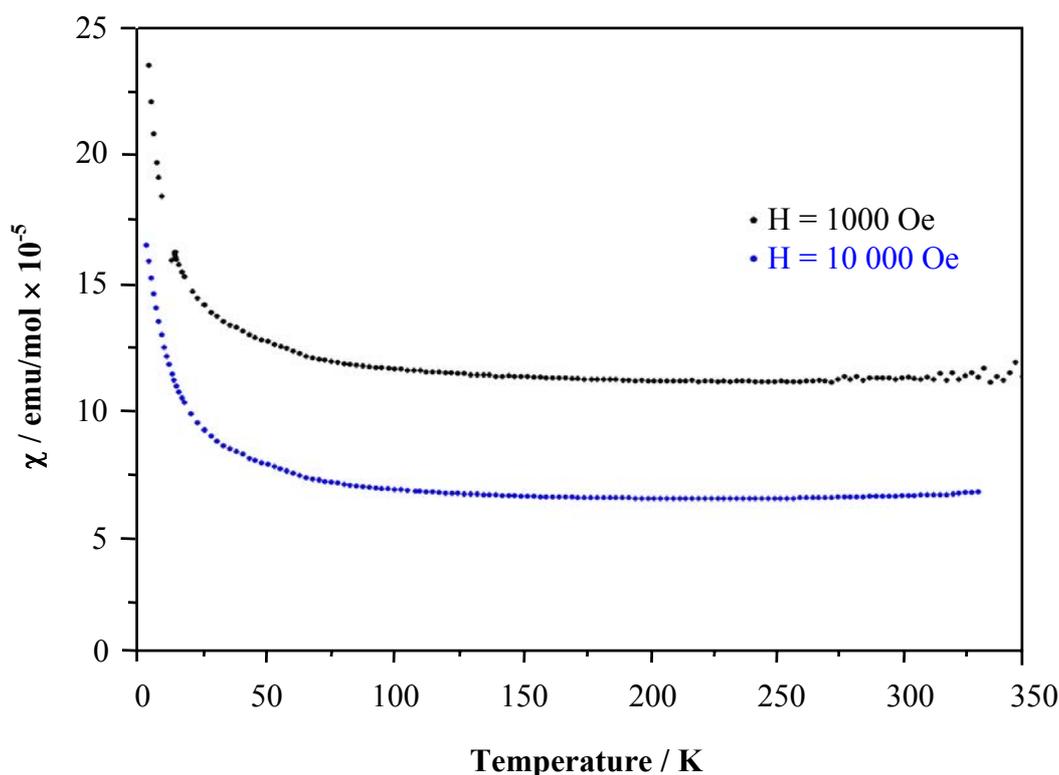
Fig. 6.23: Magnetic susceptibility of Ni_3GeTe_2 as a function of the temperature

The magnetic susceptibility of Ni_3GeTe_2 changes very weakly with the temperature and the applied magnetic field. Such behaviour suggests a paramagnetic compound. The paramagnetism is proved by the very low values of the susceptibility ($\chi \sim 10^{-5}$ emu/mol). Paramagnetic substances have typical magnetic susceptibility values, $10^{-4} \leq \chi \leq 10^{-6}$ emu/mol [3].

7 Synthesis and characterization of nanoscale hydroxylapatite

7.1 Introduction

Nanoscience investigates materials with particle size in the range of 1 to 100 nm. Today the production of nanoparticles is considered a fast growing field of science and technology with unlimited and not yet completely admitted applications in different areas of the human life – aeroplane and space industry, magnetic memory, high – strength ceramics, computer and military industry, production of solar cells, etc.

Nanoparticles are larger than individual atoms and molecules, but smaller than the bulk solid. Hence they obey neither absolute quantum chemistry nor laws of classical physics. This offers interesting and valuable properties markedly different from those expected.

There are two major phenomena responsible for that. The first is the high dispersity of nanocrystalline systems. As the size of the crystal is reduced, the number of atoms at the surface compared to the number of atoms in the crystal itself, increases. Properties, which are usually determined by the crystal structure of the bulk lattice, now become increasingly dominated by the defect structure of the surface. The second phenomenon occurs noticeably only in metals and semiconductors. It is called size quantisation and arises because the size of a nanoparticle is comparable to the Broglie wavelengths of its charge carriers (i. e. electrons and holes). Due to the spatial confinement of the charge carriers, the edge of the valence and conduction bands split into discrete, quantised, electronic levels. These levels are similar to those in atoms and molecules.

The properties arising from the decrease in the size have been investigated for various inorganic materials. A number of works were dedicated to synthesis and characterization of nanoscale metal oxides, such as ZnO [86], MgO [87], TiO_2 [88, 89] and others [90 – 92], as well as to some hydroxides [87, 93], pure elements [94] and luminescent materials [95].

The size quantisation observed in metals and semiconductors also attracts many scientists. As a result, many nanosize metal particles (Ag, Cu, Pd, etc.) [96 – 98] have been synthesised and studied. Appropriate attention is paid to semiconducting materials, for example CdS [99, 100], CuCl, CuBr, CdSe [100] and many others.

In recent years many inorganic compounds with a nano – range size found applications in biomedicine. Among them probably the most extensively studied ones are Ca compounds [101, 102], and particularly hydroxylapatite – $Ca_{10}(PO_4)_6(OH)_2$ [103 – 105]. It is synthesised by a great variety of methods predominantly using organic surfactants in order to decrease the particle size. The reason for this is the fact, that this material is the main constituent of the human bones and teeth [106, 107]. Thus, the synthetic hydroxylapatite has excellent biocompatibility and bioactivity and nowadays is widely used as an implantant and coating onto prosthesis. It can also be used as a filter for heavy atoms in aqueous solutions [108], for separation of proteins and nuclei acids [109] and also in catalysis [110].

In this chapter, a simple synthesis approach as well as characterization of nanoscale particles of hydroxylapatite are described. The problems arising in the course of the work are discussed.

7.2 Experimental outline

The synthesis of nanoscale crystals of hydroxylapatite was performed by a drop wise titration of $CaCl_2$ aqueous solutions with aqueous solutions of $(NH_4)_2HPO_4$. Three different concentrations for both solutions were used and investigated. An overview of the operating conditions for each sample is presented in Table 7.1.

Table 7.1: Operating conditions for nanorange crystals of hydroxylapatite

c_{CaCl_2} / g/l	1			2			3		
$c_{(NH_4)_2HPO_4}$ / g/l	1	2	3	1	2	3	1	2	3
T / K	293			293			293		
Titrating speed / drop min^{-1}	12 – 15			12 – 15			12 – 15		
Type of stirring	continuous			continuous			continuous		

After complete adding, the resulting solution was aged for 24 hours and subsequently decanted. The obtained fine white crystals were washed with ethanol and dried in an oven at 80°C. Each of the dried samples was split into two equal parts. The first was characterized by IR spectroscopy and scanning electron microscopy (SEM). The second part was calcinated in

a tube furnace at 650 °C for six hours. After that it was examined with IR spectroscopy and SEM. The experimental procedure is summarised in Fig. 7.1. Wang et al. described similar, but more complicated procedures for the synthesis of hydroxylapatite, [103 - 105]. It includes the addition of non-ionic organic surfanctants and preparation of special oil – in – water emulsions in order to decrease the size of the obtained hydroxylapatite powders.
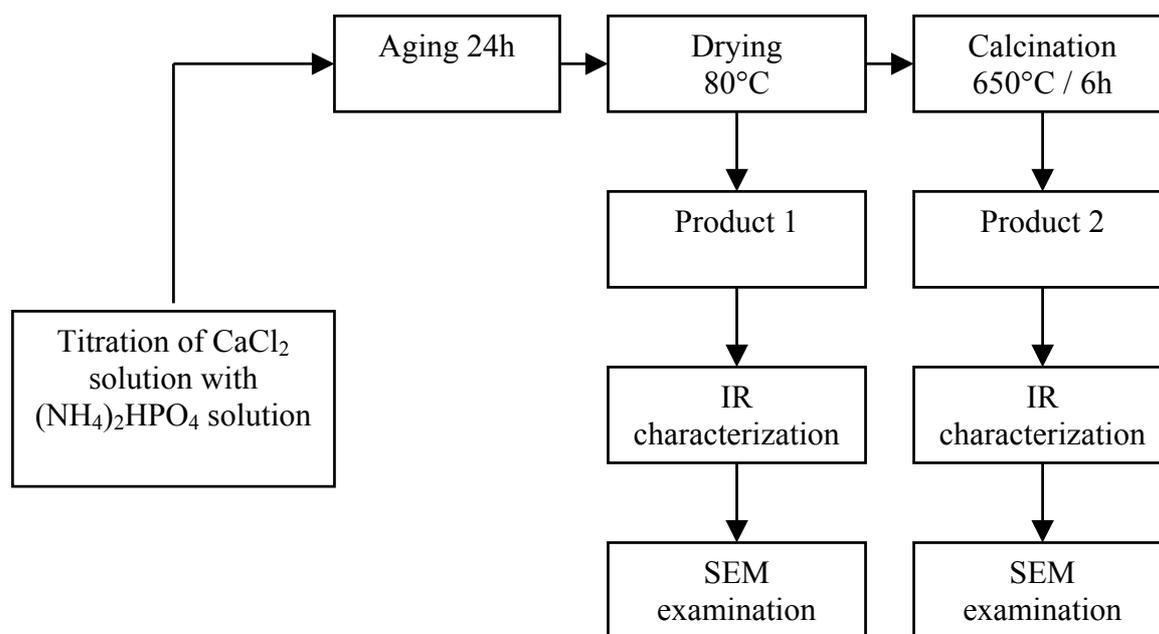
Fig 7.1: Preparation procedure of hydroxylapatite crystals with nanorange size

7.3 Results and discussion

7.3.1 IR characterization

In the spectra of the products obtained by drop wise titration of CaCl$_2$ aqueous solution **(concentration c = 1 g/l)** with (NH$_4$)$_2$HPO$_4$ aqueous solutions with concentrations c = 1, 2 and 3 g/l respectively are observed three main groups of vibrations (Fig. 7.3):

– in the range 3450 – 3230 cm^{-1} – valence vibrations of the OH^- groups

– around 1035 cm^{-1} – characteristic valence vibrations ν_3 [111] of the PO_4^{3-} groups.

– between 600 – 550 cm^{-1} – characteristic valence vibrations ν_4 [111] of the PO_4^{3-} groups.

The bands in spectra b_1 and c_1 at 866, 876 cm^{-1}, respectively, are characteristic of the HPO_4^{2-} anions [112]. They can be explained as traces of residual $(NH_4)_2HPO_4$. The absorption maxima at 1396, and 1394 cm^{-1} with a great probability can be attributed to either combination vibrations, or overtone of valence, or deformation vibrations of the PO_4^{3-} group, which are located below 650 cm^{-1}.

Combining the aforementioned reasons and comparison of the IR – spectra of hydroxylapatite (Fig. 7.2) [112, 113], with the spectra shown in Fig. 7.3 leads to the conclusion that titration of $CaCl_2$ water solution (c = 1 g/l) with aqua solutions of $(NH_4)_2HPO_4$ with concentrations c = 1, 2 and 3 g/l respectively, results in formation of pure hydroxylapatite – $Ca_{10}(PO_4)_6(OH)_2$.
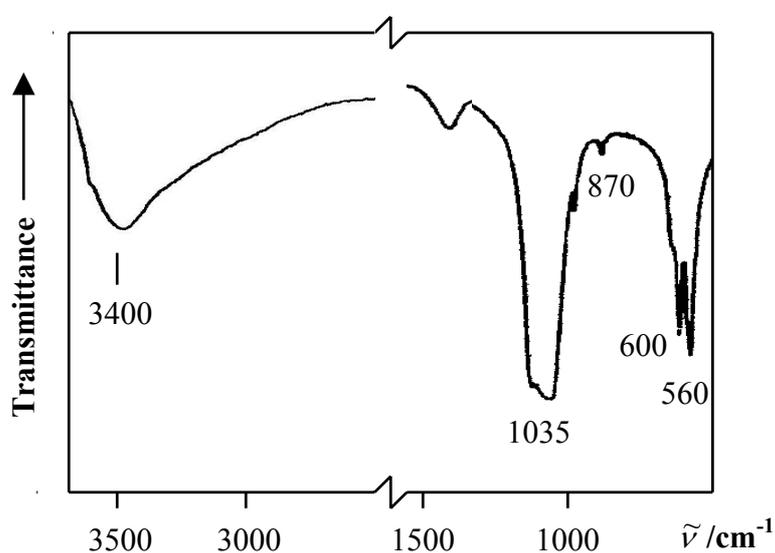
Fig. 7.2: Infrared transmission spectra in the MIR range of hydroxylapatite [113]
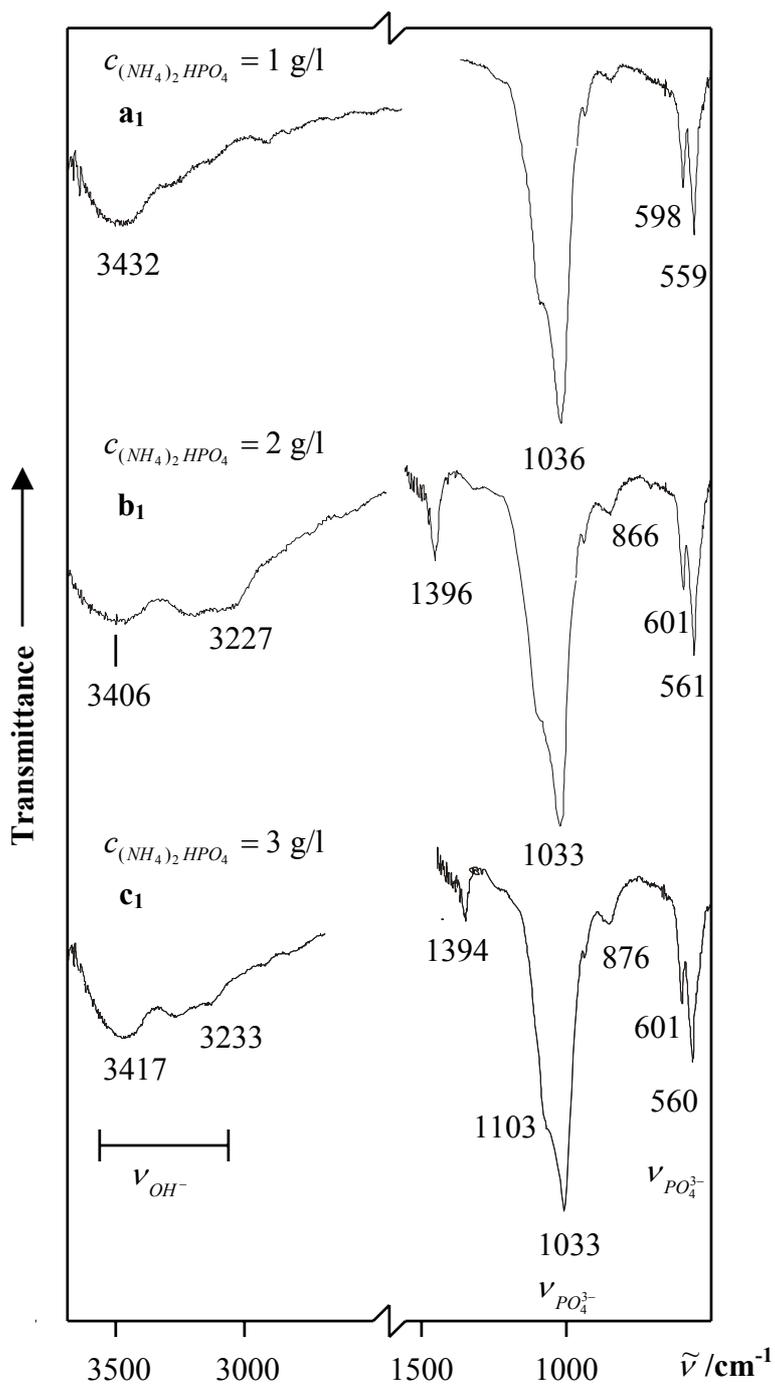
Fig. 7.3 Infrared transmission spectra in the MIR range of products obtained by dropping of water solutions of $(NH_4)_2HPO_4$ to $CaCl_2$ aqua solution **(c = 1 g/l)**

IR spectra of the products obtained by dropping of $(NH_4)_2HPO_4$ aqueous solutions with concentrations 1, 2 and 3 g/l to aqueous solution of $CaCl_2$ **(concentration c = 2 g/l)** are represented on Fig. 7.4.
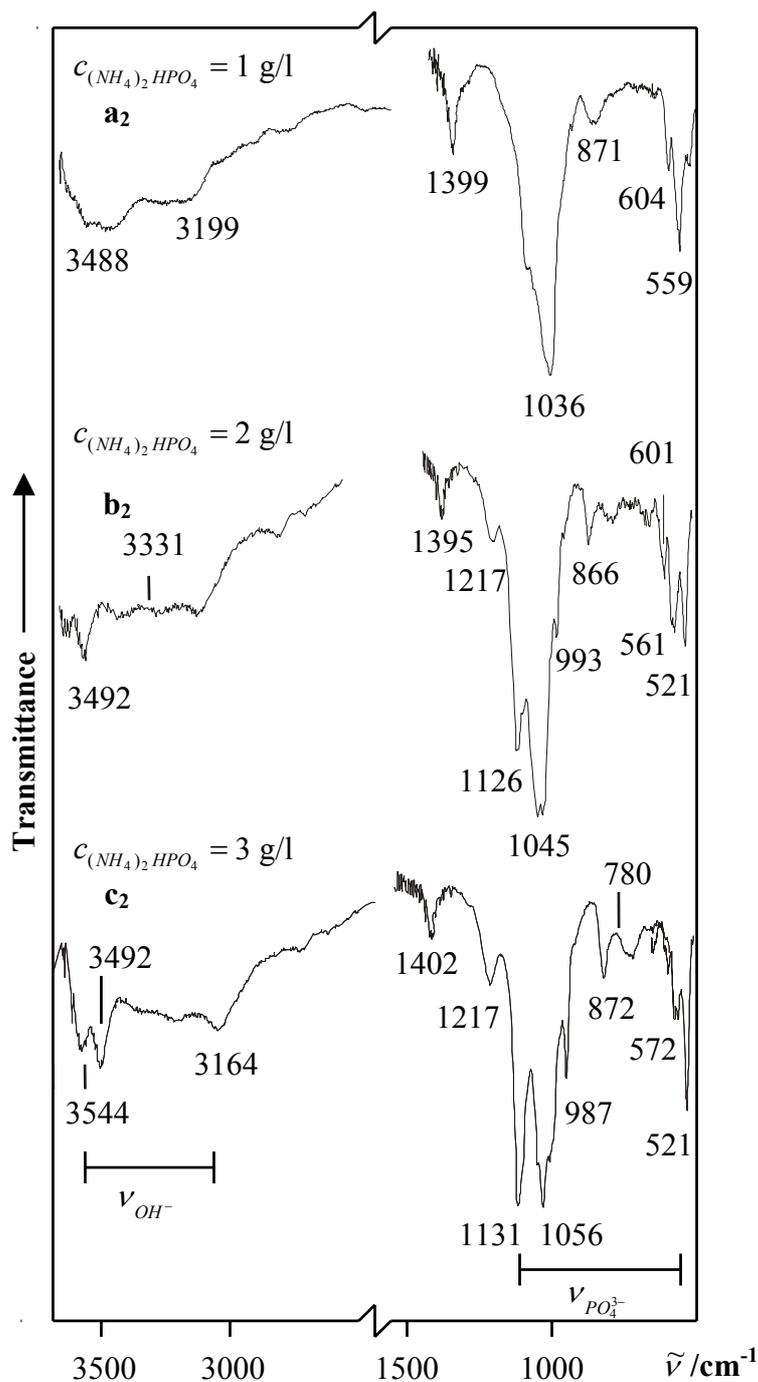
Fig. 7.4: Infrared transmission spectra in the MIR range of products obtained by dropping of aqueous solutions of $(NH_4)_2HPO_4$ to $CaCl_2$ aqueous solution **(c = 2 g/l)**

Dropping of $(NH_4)_2HPO_4$ solution with concentration 1 g/l to the $CaCl_2$ solution leads to formation of pure hydroxylapatite. This is proved by the characteristic vibrations of OH^- (v_{OH^-} = 3488 cm^{-1} and 3199 cm^{-1}) and PO_4^{3-} ($v_{PO_4^{3-}}$ = 1036, 604, 559 cm^{-1}) groups. In the spectra b_2 and c_2 more bands are present. Instead of one maximum at 1036 cm^{-1} (spectrum a_2)

two bands are observed at 1126, 1045 cm^{-1}, respectively 1131, 1056 cm^{-1}, which are shifted to higher wave numbers. Nevertheless, they are located in the characteristic range of the phosphate groups. By taking into account the vibrations between 570 – 520 cm^{-1} (v_4 for PO_4^{3-}), it can be concluded that dropping $(NH_4)_2HPO_4$ solutions with concentrations 2 and 3 g/l results in formation of some calcium phosphate. In the range 3550 to 3300 cm^{-1} two additional bands are found. In this region v_{OH} of the crystal water are located [111]. This fact supposes the formation of calcium phosphate crystal hydrate, probably brushite – $CaHPO_4 \cdot 2H_2O$, but not hydroxylapatite.

The bands at 1217, 993, 866 cm^{-1} (spectrum b$_2$) and 1217, 987, 872, 780 cm^{-1} in spectrum c$_2$ belong to the characteristic vibrations of HPO_4^{2-} groups, however, with higher intensities compared to those observed in Fig. 7.3.

Fig. 7.5 represents the IR spectra of samples obtained by drop wise addition of aqueous solutions of $(NH_4)_2HPO_4$ with concentrations 1, 2 and 3 g/l to aqueous solution of $CaCl_2$ **(concentration c = 3 g/l)**. The characteristic vibrations of OH^- (v_{OH^-} = 3488 cm^{-1} and 3199 cm^{-1}) and PO_4^{3-} ($v_{PO_4^{3-}}$ = 1036, 604, 559 cm^{-1}) groups in spectrum a$_3$ show formation of pure hydroxylapatite – $Ca_{10}(PO_4)_6(OH)_2$ (see Fig. 7.3, Fig. 7.4). Spectra b$_3$ (Fig. 7.5) shows two bands at 1137 cm^{-1} and 1057 cm^{-1}, while and c$_3$ (Fig. 7.5) shows bands at 1131 cm^{-1} and 1056 cm^{-1}, respectively, as opposed to one maximum at 1033 cm^{-1} observed in spectrum a$_3$, analogous to spectra b$_2$ and c$_2$ from Fig. 7.4. As in the previous case this suggests formation of brushite with impurities of $(NH_4)_2HPO_4$.
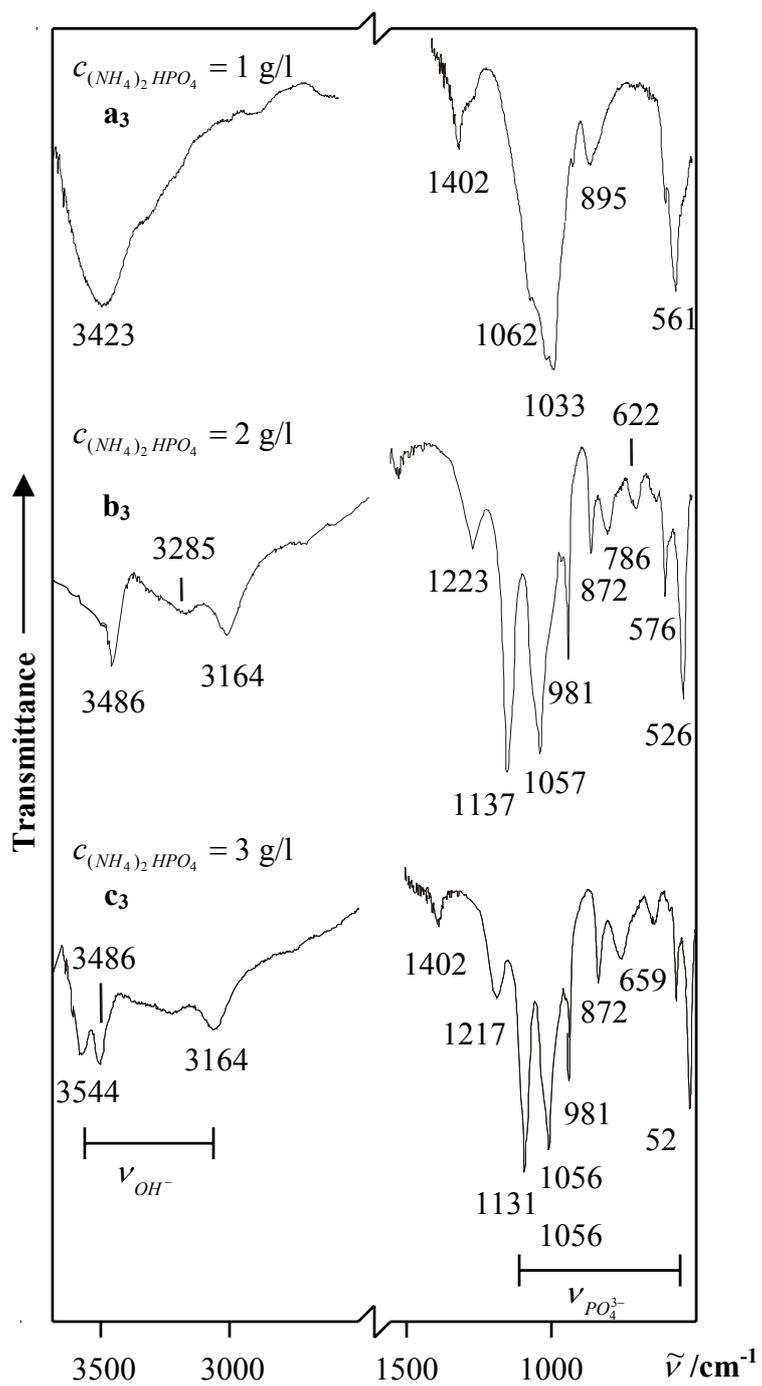
Fig. 7.5: Infrared transmission spectra in the MIR range of products obtained by drop wise titration of $CaCl_2$ aqua solution **(c = 3 g/l)** with aqueous solutions of $(NH_4)_2HPO_4$

7.3.2 X – ray characterization

Samples b_2, c_2, b_3 and c_3 were analysed by X – ray powder diffraction (Fig. 7.6).
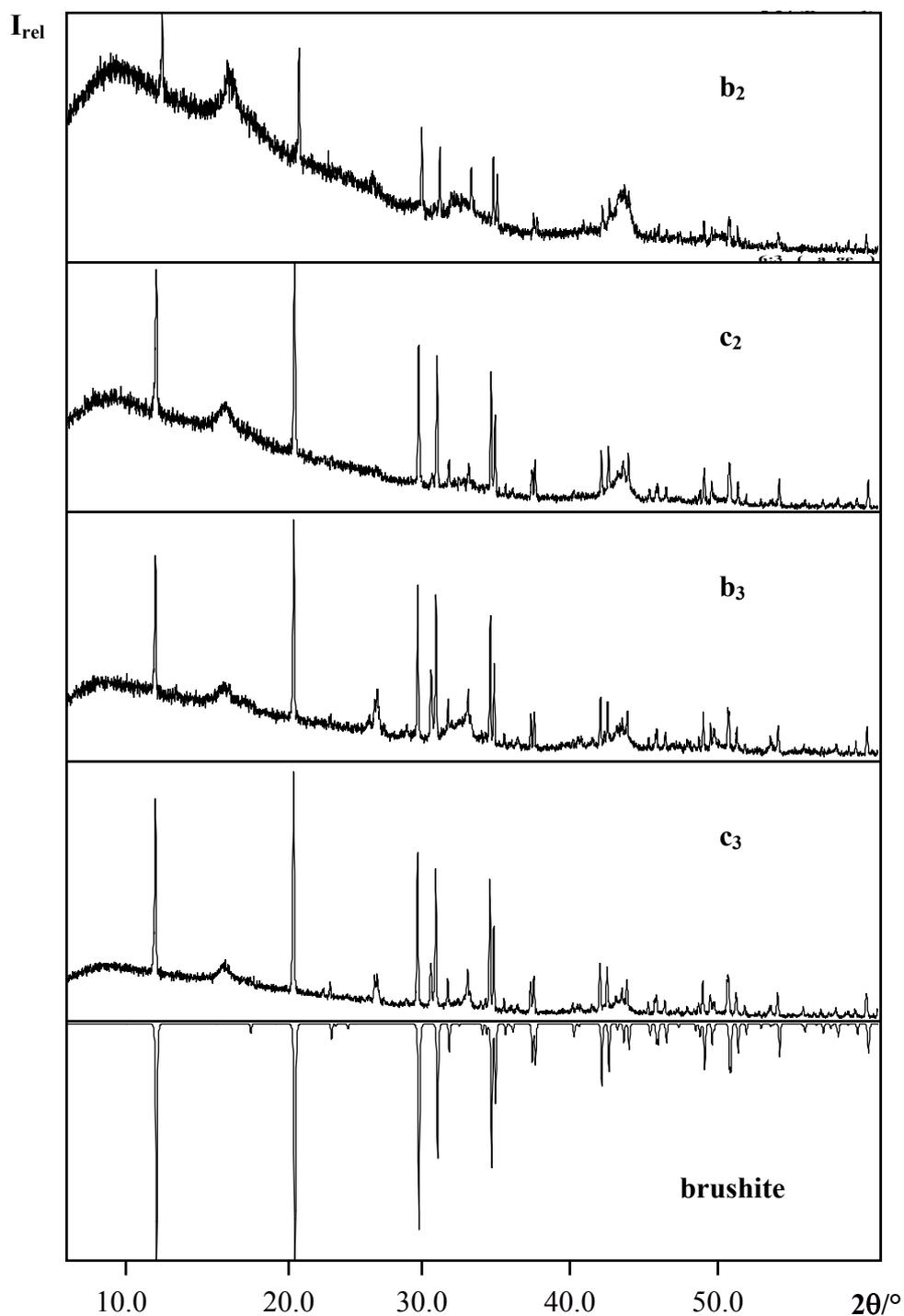
Fig 7.6: Comparison between the measured powder patterns of the brushite samples (b_2, c_2, b_3, c_3) and the calculated one

A comparison between the measured patterns and the patterns of the known phosphates revealed that the product formed in these cases is brushite – CaHPO$_4$·2H$_2$O. The presence of crystal water in this substance corresponds well with the IR spectra, in which its characteristic vibrations (v_{OH^-} = 3550 – 3300 cm^{-1}) are also found (see 7.3.1). The good quality of the powder patterns of these samples suggests a crystal size in the micrometer range, which is much larger than the desired particle size. Opposite to that are the bad quality powder patterns of the samples, which are hydroxylapatite (Fig. 7.7). Owing to the broad peaks with low intensity as well as the noise, this pattern cannot be used for identification purposes. However, it indicates the nano – crystalline nature of the product. As such only IR spectroscopy was used for the identification of these samples.
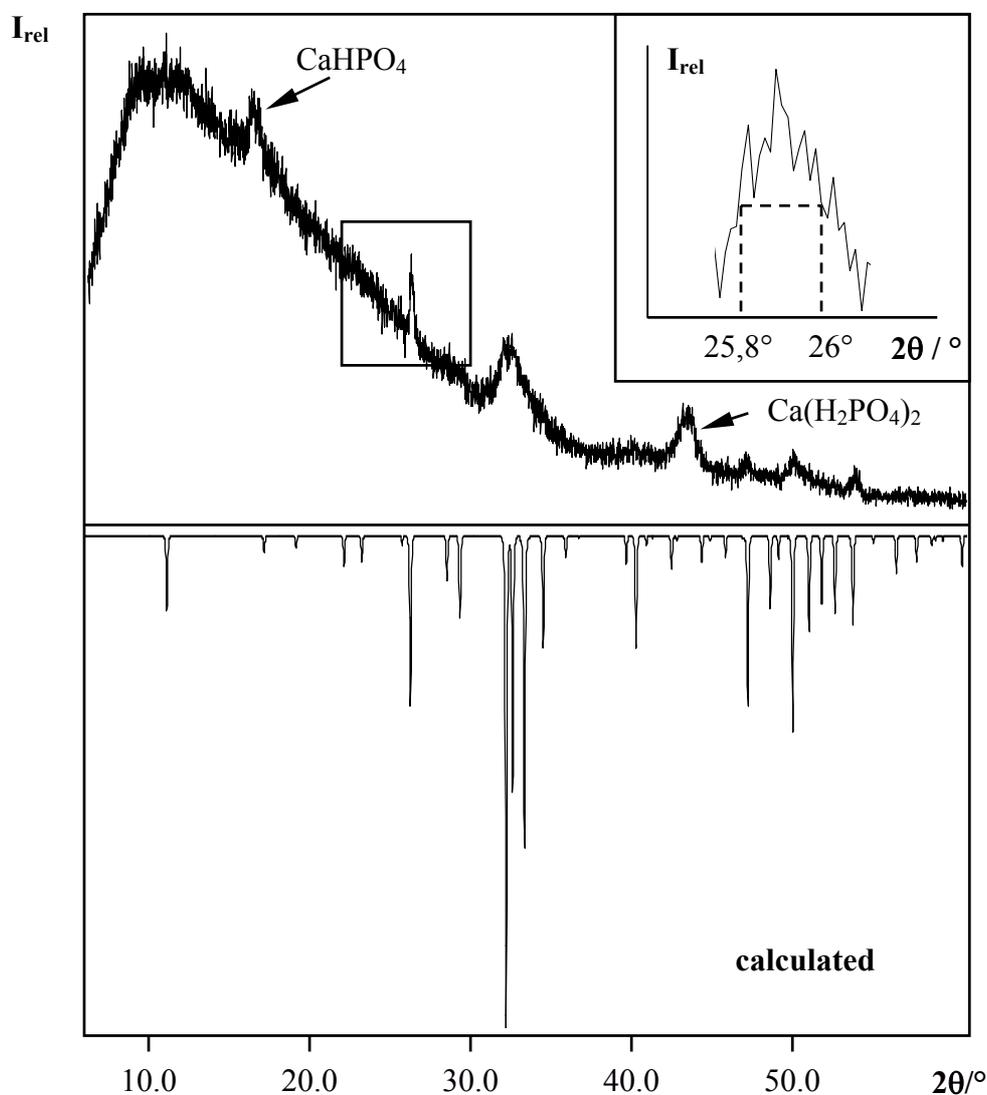
Fig. 7.7: Comparison between a measured powder pattern of hydroxylapatite (top), obtained by drop wise adding of (NH$_4$)$_2$HPO$_4$ in aqueous solution to a CaCl$_2$ solution and the calculated one (bottom)

The approximate average crystalline size *D* was calculated from the sharpest diffraction peak (see Fig. 7.7) at the **F**ull angular **W**idth at **H**alf **M**aximum (FWHM), using the Sherrer's formula [114 – 117]:

$$D = \frac{K\lambda}{\Delta(2\theta)\cos\theta} = 71\,\text{nm}$$

where, λ is the X – ray wavelength (1.548 Å for Cu K$_\alpha$), $K = 0.9$ is proportional coefficient, θ = 12.9° is the diffraction angle and $\Delta(2\theta)$ is FWHM. The obtained particle size of 71 nm was calculated with $\Delta(2\theta) = 0.225°$.

7.3.3 SEM investigation

For estimation of the approximate size of the obtained particles, an analytical scanning electron microscope (SEM) was used. Fig 7.8 shows the SEM pictures of products obtained by dropping of aqueous solutions of $(NH_4)_2HPO_4$ to $CaCl_2$ aqueous solution with concentration c = 1 g/l.

$c_{(NH_4)_2 HPO_4} = 1$ g/l $c_{(NH_4)_2 HPO_4} = 2$ g/l $c_{(NH_4)_2 HPO_4} = 3$ g/l

$c_{CaCl_2} = 1$ g/l
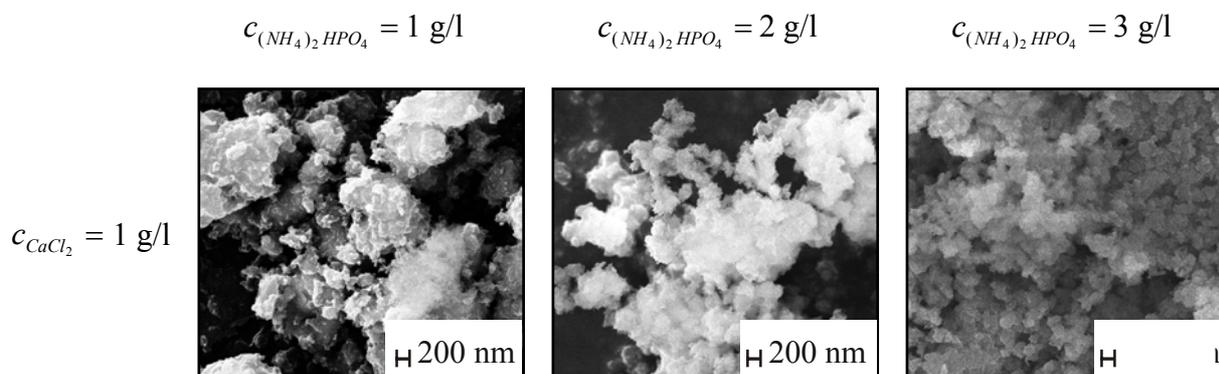
Fig. 7.8: SEM images of samples obtained by drop wise adding of $(NH_4)_2HPO_4$ aqueous solutions to aqueous solution of $CaCl_2$ **(c = 1 g/l)**

At concentrations of the $(NH_4)_2HPO_4$ solution 1 and 2 g/l the particles size is around 200 nm. The increase of the concentration up to 3 g/l leads to an increase of the particles size of about 50% – up to 300 nm.

As was mentioned above, increasing the concentration of both solutions results in the formation not only of hydroxylapatite, but also of brushite (see 7.3.2). As a consequence, a characteristic change in the morphology of the crystals and their size is observed (Fig. 7.9).

$c_{(NH_4)_2HPO_4} = 1$ g/l $c_{(NH_4)_2HPO_4} = 2$ g/l $c_{(NH_4)_2HPO_4} = 3$ g/l

$c_{CaCl_2} = 2$ g/l

Brushite   Hydroxylapatite
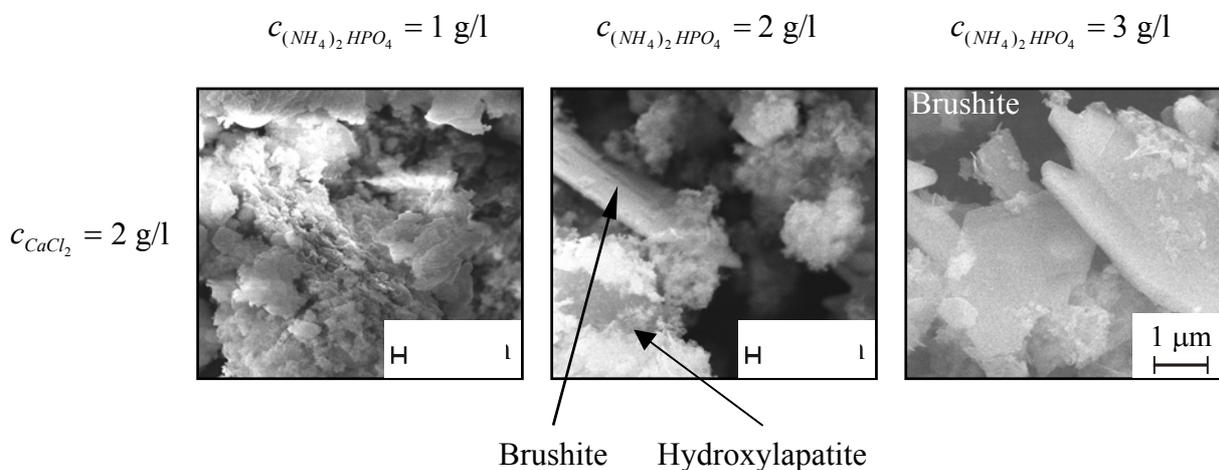
Fig. 7.9: SEM images of samples obtained by drop wise adding of $(NH_4)_2HPO_4$ aqueous solutions to aqueous solution of $CaCl_2$ **(c = 2 g/l)**

The crystal size of the hydroxylapatite particles increases sharply from 300 nm to 1 μm in brushite – $CaHPO_4 \cdot 2H_2O$.

The same tendency is observed if the $CaCl_2$ solution is concentrated up to 3 g/l. Almost no change in the size of the hydroxylapatite crystals occurs, but a strong increase of the size is observed when brushite is formed (Fig. 7.10).

$c_{(NH_4)_2HPO_4} = 1$ g/l $c_{(NH_4)_2HPO_4} = 2$ g/l $c_{(NH_4)_2HPO_4} = 3$ g/l

$c_{CaCl_2} = 3$ g/l
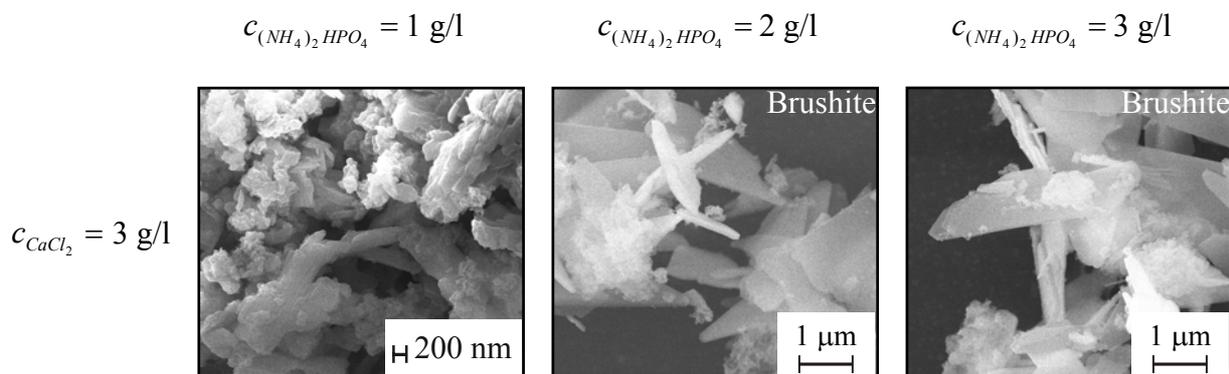
Fig. 7.10: SEM images of samples obtained by drop wise adding of $(NH_4)_2HPO_4$ aqueous solutions to aqueous solution of $CaCl_2$ **(c = 3 g/l)**

The SEM study of the hydroxylapatite samples obtained via dropping of $(NH_4)_2HPO_4$ aqueous solutions to those of $CaCl_2$ showed also small quantities of particles with a size between 60 and 90 nm, i. e. in the nano range. This size is in fairly good agreement with the size calculated from the powder pattern using Sherrer's formula.

Hydroxylapatite crystallizes hexagonally (SG *P6₃/m, a = 943.2 pm, c = 688.1 pm*) [118, 119]. Phosphor atoms are tetrahedrally surrounded by oxygen atoms. Ca atoms occupy two crystallographically different sites. Ca1, located at *4f* is surrounded by nine O atoms belonging to six (PO₄) tetrahedra. The environment of Ca2, which is located at *6h* consist of eight atoms – six O atoms belonging to five (PO₄) tetrahedra and one OH group. A projection of the hydroxylapatite structure is shown on Fig. 7.11.
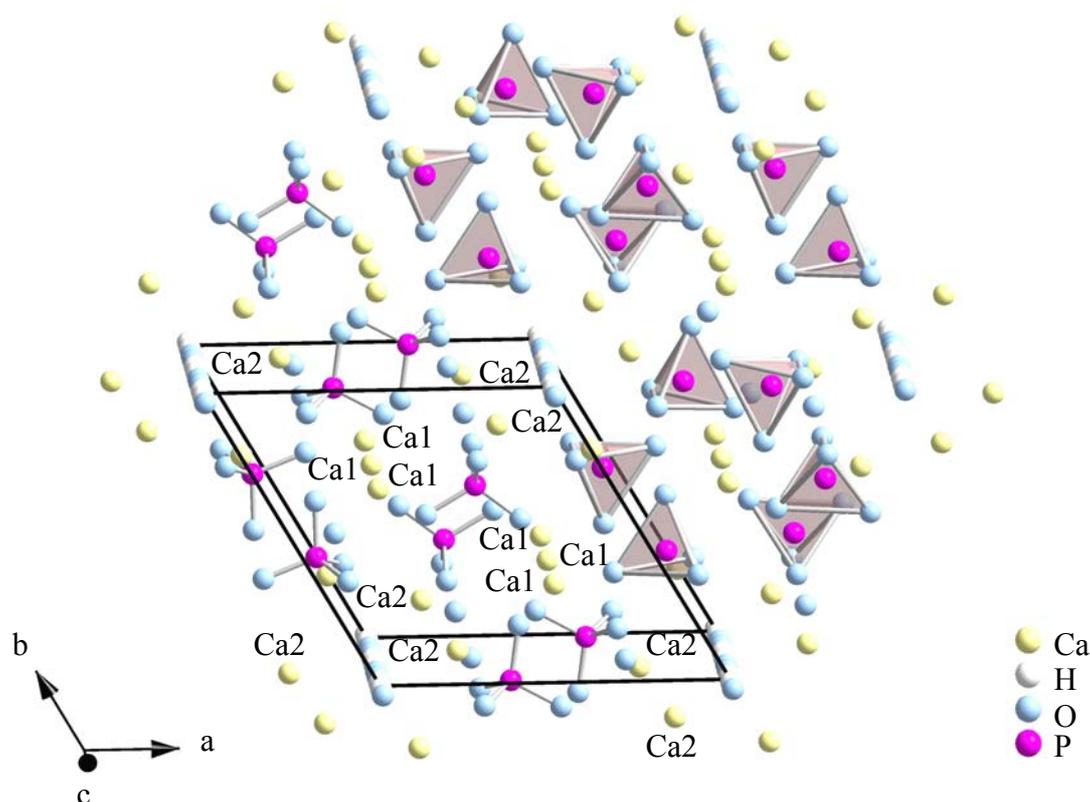
Fig. 7.11: General projection of the $Ca_{10}(PO_4)_6(OH)_2$ structure

Because of the extremely small size of the obtained hydroxylapatite particles, it is not possible to find a relationship between their morphology and crystal structure. In this case, it is probable that the form of the particles depends on the conditions at which hydroxylapatite is formed (concentration, temperature, stirring, etc.).

In contrast to that, the morphology of the obtained brushite crystals can be explained in terms of the crystal structure. It crystallizes in the monoclinic space group *Ia* (*a = 581.2(2) pm, b=1518.0(3) pm, c = 623.9(2) pm, β = 116.43(3)°*) [120 – 122]. The structure is built of (PO_4) tetrahedra and (CaO_8) polyhedra, which form double layers alternating along [010]. The layers are connected via hydrogen bonds (Fig. 7.12).
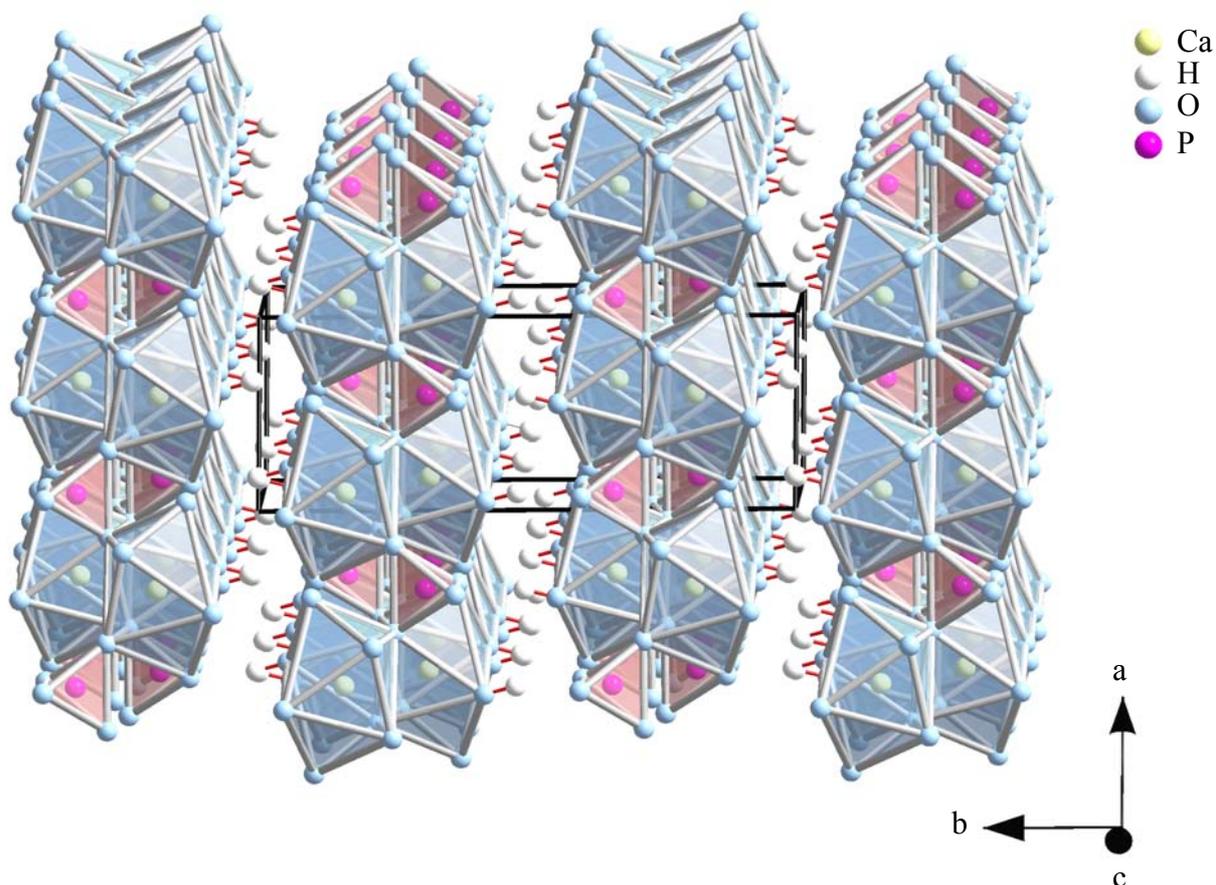
Fig. 7.12: Characteristic section of the $CaHPO_4 \cdot 2H_2O$ structure. (PO_4) tetrahedra and (CaO_8) polyhedra built double layers alternating along [010], connected via hydrogen bonds

The obtained brushite crystals are needle – like, elongated in one direction. According to the crystal structure it should be [010]. In the unit cell of brushite, the *b* axis is significantly longer (almost three times) than the other two axes *a* and *c*. This means that the crystal growth rate along [010] can be smaller compared to that in the other two directions, [100] and [001]. A smaller growth rate leads to a more perfect crystallisation along [010]. Similar results were reported by Le Geros [123]. It is found that the crystal habit of brushite is also governed by the method of growth – whether in solution or gel, temperature and presence of impurities [123 – 125].

7.3.4 Influence of the temperature

The samples of hydroxylapatite were calcinated at 650°C (m.p. = 1614°C for hydroxylapatite) for six hours to investigate the influence of heat treatment on the crystal size. After that the products were investigated by IR spectroscopy for characterization. The particle size was measured with an analytical scanning electron microscope.

The IR spectra of the hydroxylapatite samples after temperature treatment (Fig. 7.14) show groups of vibrations in the following ranges:

– 1200 – 930 cm^{-1} – v_3 characteristic valence vibrations of the PO_4^{3-} groups [111]

– between 600 cm^{-1} and 450 cm^{-1} – v_4 vibrations of the PO_4^{3-} [111]

The IR spectra do not show any vibrations around 3400 cm^{-1}, where normally the characteristic vibrations of the OH^- groups are normally located.

Comparison of the measured spectra with data found in the literature [112] revealed that the spectra shown in Fig. 7.14 are identical with those of calcium orthophosphate – $Ca_3(PO_4)_2$ (Fig.7. 13), i. e. temperature treatment leads to a change in the chemical composition of the samples.
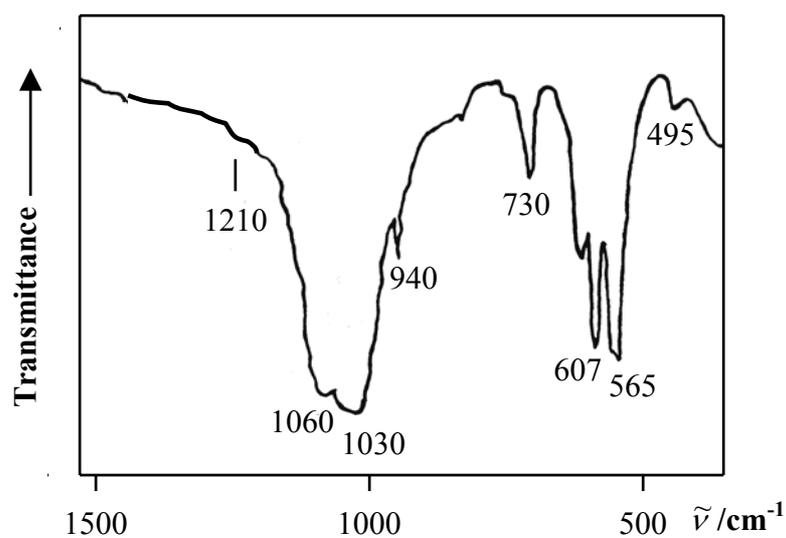
Fig. 7.13: Infrared transmission spectra in the MIR range of calcium orthophosphate
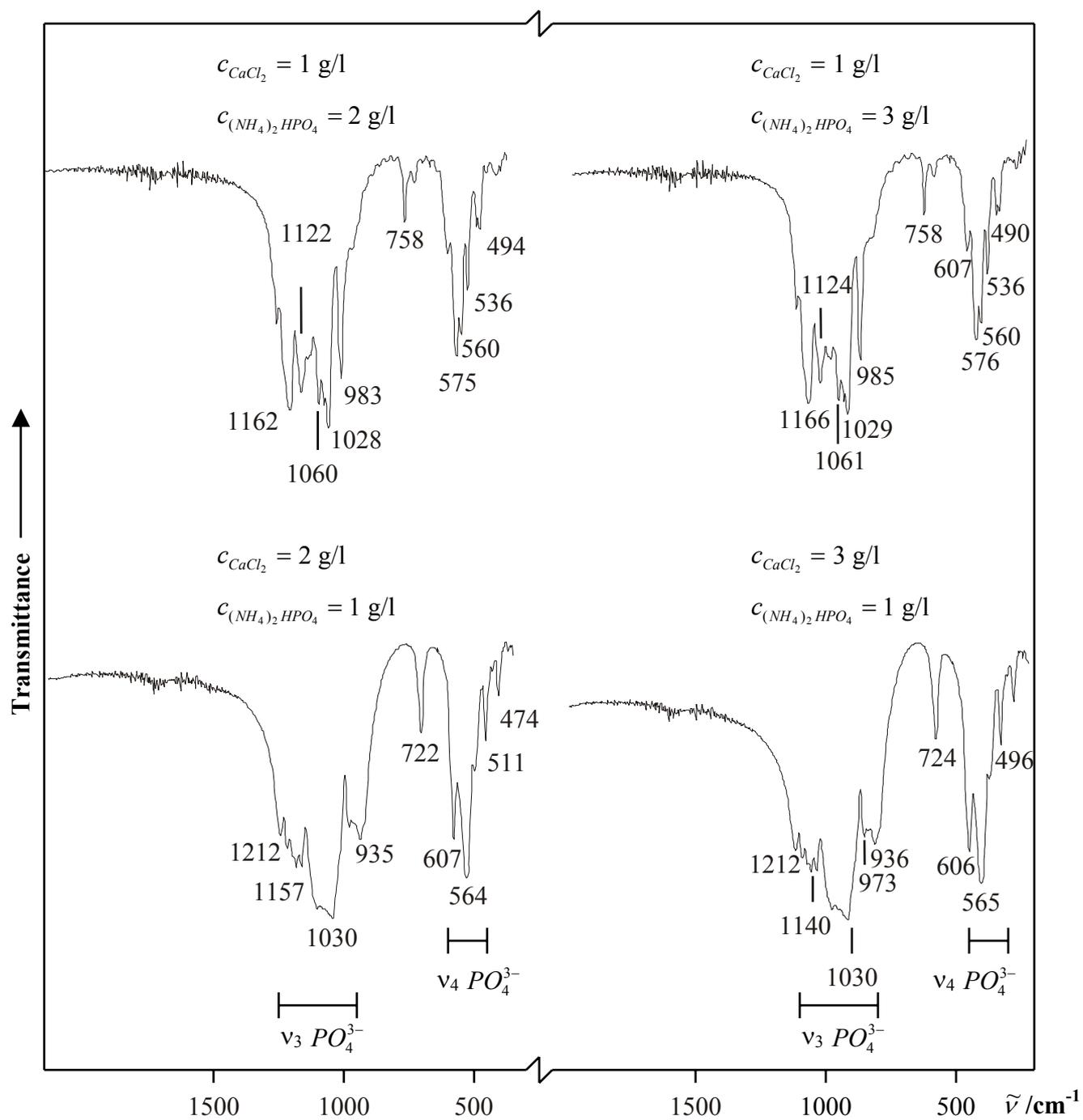
Fig. 7.14: Infrared transmission spectra of hydroxylapatite samples after calcination at 650°C for 6 hours measured in the MIR range. The spectra are identical with that one of calcium orthophosphate – $Ca_3(PO_4)_2$

The samples of calcium orthophosphate obtained after the hydroxyapatite calcination were studied with SEM to check the crystal size. Two of the obtained $Ca_3(PO_4)_2$ samples have crystals with a size around 100 nm (Fig. 7.15). The crystal size of the other samples remains unchanged, around 200 nm.

$c_{CaCl_2} = 1$ g/l $\qquad c_{(NH_4)_2HPO_4} = 2$ g/l $\qquad\qquad c_{CaCl_2} = 1$ g/l $\qquad c_{(NH_4)_2HPO_4} = 3$ g/l
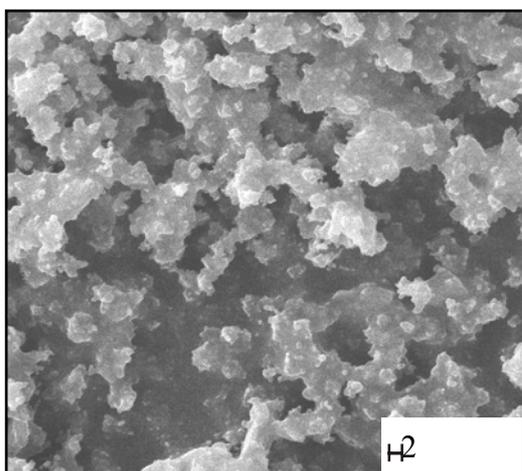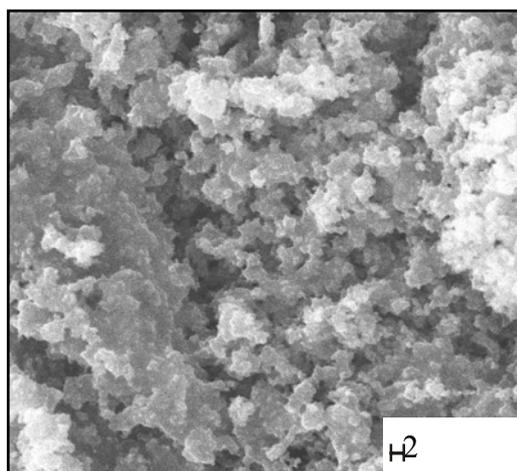
$c_{CaCl_2} = 2$ g/l $\qquad c_{(NH_4)_2HPO_4} = 1$ g/l $\qquad\qquad c_{CaCl_2} = 3$ g/l $\qquad c_{(NH_4)_2HPO_4} = 1$ g/l
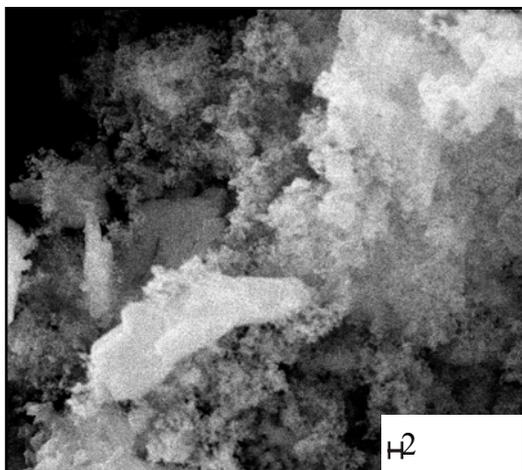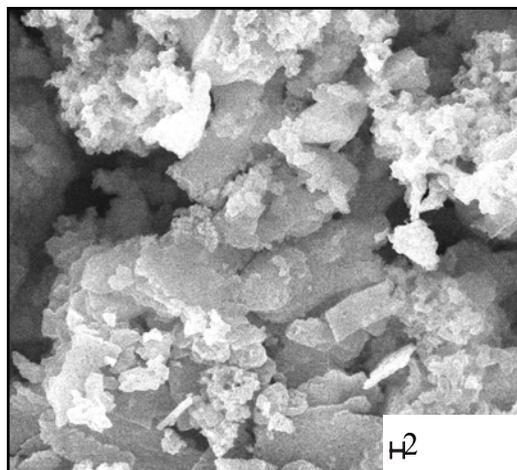
Fig. 7.15: SEM pictures of $Ca_3(PO_4)_2$ samples obtained after calcination of hydroxylapatite at 650°C for six hours

7.3.5 Conclusion

The IR characterization of the products obtained by drop wise titration of aqueous solutions of $CaCl_2$ with aqueous solutions of $(NH_4)_2HPO_4$ showed that with concentrations 1, 2 and 3 g/l of both solutions, hydroxylapatite is obtained only in the cases shown in Tab. 7.2. In the other cases secondary reactions, in particular the formation of brushite – $CaHPO_4 \cdot 2H_2O$ instead of hydroxylapatite – $Ca_{10}(PO_4)_6(OH)_2$ occur. This is proved by X – ray powder diffraction.

Table 7.2: Products obtained by drop wise titration of $CaCl_2$ aqueous solutions with solutions of $(NH_4)_2HPO_4$

c_{CaCl_2} / g/l $\diagdown$ $c_{(NH_4)_2HPO_4}$ / g/l	1	2	3
1	$Ca_{10}(PO_4)_6(OH)_2$	$Ca_{10}(PO_4)_6(OH)_2$	$Ca_{10}(PO_4)_6(OH)_2$
2	$Ca_{10}(PO_4)_6(OH)_2$	*Brushite*	*Brushite*
3	$Ca_{10}(PO_4)_6(OH)_2$	*Brushite*	*Brushite*

SEM studies of the obtained chemical compounds revealed, that in cases when hydroxylapatite is formed, the particle size is between 180 nm and 300 nm. A small number of crystals with nanoscale size from 60 nm to 90 nm is also observed.

Increasing the concentration of the initial solutions leads to the formation of brushite. This is accompanied by achange in the crystal habitus and an increased crystal size up to 1 μm.

Temperature treatment of hydroxylapatite at 650°C for 6 hours resulted in a transformation of the hydroxylapatite into calcium orthophosphate. A SEM study showed particle sizes at the upper border of the nano range (100 nm).

The previously described experimental route is not sufficient for the synthesis of nanoscale hydroxylapatite, but it can be used for the synthesis of calcium orthophosphate with particle sizes in the nano range. For the synthesis of hydroxylapatite with nano size crystals the process should be modified by organic surfactants [103 – 105] or more diluted solutions. Furthermore, a decrease in the crystal size can be achieved via the titration of solutions heated to 80 – 100°C combined with stirring, followed by immediate cooling with ice [126].

8 Preliminary experiments to synthesise new ternary transition metal chalcogenides

The new compounds described in the preceding chapters show only a very small part of the experiments carried out in the course of this work. In solid state chemistry it is often the case that many experiments prove to be unfruitful and though they do not yield the desired compound, they helped to deduce the synthesis procedures previously described. Since they cost a lot of time and labour it is obligatory to mention something about them.

8.1 Research on transition metal olivines, A_2BX_4
   (A = transition metal; B = Si, Ge, Sn; X = Se, Te)

The experimental work in this field was concentrated on the synthesis of new selenium and tellurium olivines of the first row transition metal elements, predominantly Cr, Mn, Fe, Co, Ni and Zn (Tab. 8.1).

Table 8.1: Investigated compositions of new members of the olivine family

Chemical composition of the educt	Reaction temperature / °C	Reaction product
Cr_2SiSe_4	800	Cr_3Se_4 + Si + ?
Cr_2GeSe_4	600; 800	Cr_2Se_3 + GeSe
Mn_2GeTe_4	700	$MnTe_2$ + GeTe + ?
Mn_2SnSe_4	600; 800	MnSe + $SnSe_2$
Fe_2SiSe_4	800	Fe_7Se_8 + Si + ?
Fe_2GeTe_4	600; 700; 800	$FeTe_2$ + GeTe + ?
Co_2GeSe_4	800	CoSe + $GeSe_2$
Ni_2GeSe_4	600	NiSe + $GeSe_2$
Zn_2GeSe_4	800	ZnSe + $GeSe_2$

The experiments for the synthesis of new olivine compounds were performed through a classical solid state reaction. Stoichiometric mixtures of the pure elements were filled in quartz glass ampoules. After evacuation and sealing they were annealed for three weeks in a

standard tube furnace at temperatures between 600°C and 800°C (Tab. 8.1). The characterization of the products was carried out with the help of X – ray powder diffraction.

The reaction products of the Mn, Co, Ni and Zn containing educts resulted in the formation of the corresponding transition metal selenide MSe (black coloured, M = Mn, Co, Ni, Zn) and $GeSe_2$ (orange).

In the case of Cr – and Fe – containing samples unreacted silicon and the formation of Cr_3Se_4 or Fe_7Se_8, respectively, could be observed. No further phases could be detected, although selenium is missing to complete the starting composition.

The experimental trials for the synthesis of Cr_2GeSe_4, independently of the reaction temperature led to the formation of two phases after the solid state reaction. The first one, a homogeneous looking black powder was Cr_2Se_3. The second phase, plate – like, dark – grey crystals were identified as GeSe (Fig. 8.1a, 8.1b).

The synthesis of two new tellurides, Fe_2GeTe_4 and Mn_2GeTe_4, possible new members of the olivine structure family, was attempted by solid state reactions at different temperatures. In both cases the products contained the corresponding binary transition metal telluride, MTe_2 (M = Mn, Fe) and GeTe. Again, no further products could be clearly identified.

(a)
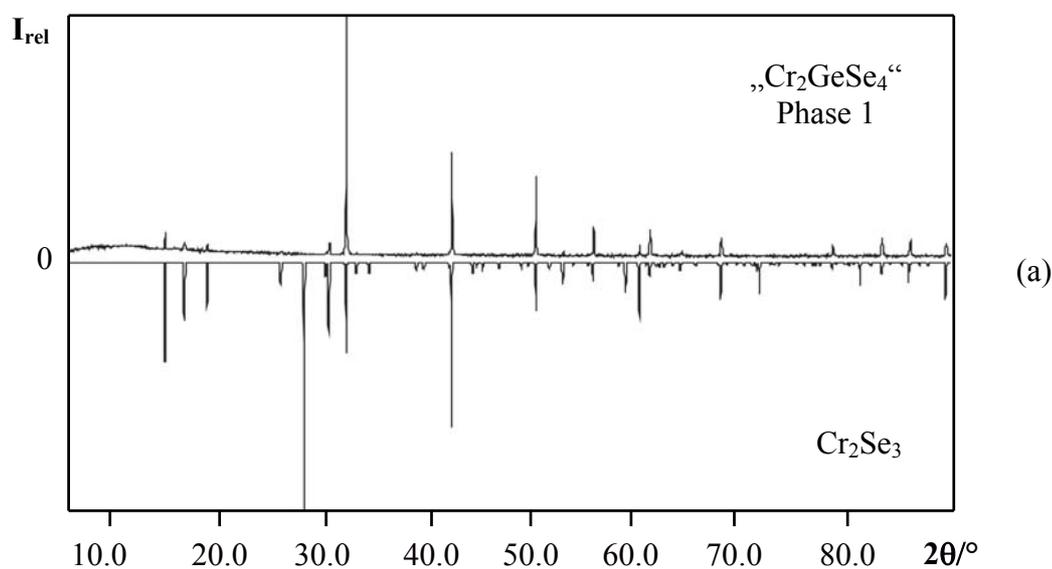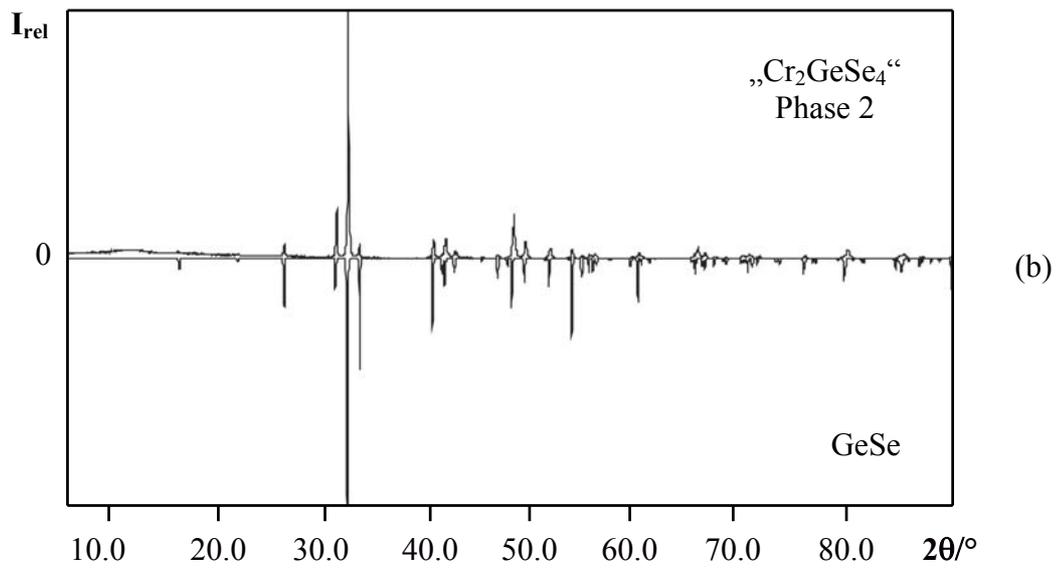
Fig. 8.1: Comparison between the measured powder patterns of phases 1 and 2 of "Cr$_2$GeSe$_4$" synthesised at 600°C, and the calculated patterns of Cr$_2$Se$_3$ (a), and GeSe (b)

8.2 Attempts to prepare ternary compounds of the type $M_2X_2Y_6$
(M = transition metal, X = Si, Ge, Sn, Y = S, Se, Te)

Experimental studies similar to the investigations of the transition metal olivines were carried out to prepare new selenides and tellurides of the first row transition metals, Cr, Mn, Fe, Co, Ni, possibly belonging to the $M_2X_2Y_6$ family. Additionally, Mo-, W-, and S − containing compositions were tested. (Tab. 8.2)

Table 8.2: Investigated $M_2X_2Y_6$ compositions

Chemical content	Reaction temperature / °C	Reaction product
$Cr_2Ge_2S_6$	750; 800	$Cr_2S_3 + GeS_2 + ?$
$Cr_2Sn_2Te_6$	700; 900; 1000	$CrTe + SnTe + ?$
$Mo_2Ge_2Se_6$	600; 700	$MoSe + GeSe_2$
$Mo_2Ge_2Te_6$	700	$MoTe_2 + GeTe$
$W_2Ge_2Te_6$	700	$WTe_2 + GeTe$
$Mn_3Ge_2Te_6$	700	$MnTe_2 + GeTe$
$Fe_2Si_2Te_6$	500; 600; 700; 800; 900	$FeTe_2 + SiTe_2 + ?$
$Fe_2Ge_2S_6$	750; 800	$Fe_2GeS_4 + S + ?$
$Fe_2Ge_2Se_6$	500; 600; 700; 800	$FeSe + GeSe_2$
		$Fe_2GeSe_4 + GeSe_2$ (600°C)
$Fe_2Ge_2Te_6$	600; 700; 800	$FeTe_2 + GeTe$
$Co_2Si_2Te_6$	500; 600; 700; 800	$CoTe_2 + Si + Te$
$Co_2Ge_2S_6$	800	$Co_4S_3 + GeS_2 + ?$
$Co_2Ge_2Se_6$	500; 600	$CoSe_2 + GeSe_2 + ?$
$Co_2Ge_2Te_6$	600; 700	$CoTe_2 + GeTe$
$Ni_2Si_2Te_6$	500; 600; 700; 800; 900	$NiTe_2 + Si_2Te_3 + ?$
$Ni_2Ge_2Se_6$	500; 600; 700	$NiSe + GeSe_2$
$Ni_2Ge_2Te_6$	700	$NiTe_2 + GeTe$

The synthesis trials were carried out via solid state reactions. The samples were prepared by mixing the pure elements in stoichiometric proportions. The blends were filled in quartz ampoules. After evacuation and sealing the ampoules containing the samples were annealed in a furnace for 20 days at temperatures in the range 500°C to 1000°C (Tab. 8.2). For the characterization of the reaction products X − ray powder diffraction was used.

The experimental tests used to synthesise new members of the $M_2X_2Y_6$ family ended with the formation of mixtures of Co_4S_3 and GeS_2 instead of $Co_2Ge_2S_6$, Cr_2S_3 and GeS_2 instead of $Cr_2Ge_2S_6$ and Fe_2GeS_4 and unreacted sulphur instead of $Fe_2Ge_2S_6$, respectively.

Regardless of the temperature, the products of a series of experiments for the synthesis of new selenides with a $M_2X_2Y_6$ structure were in some cases intimate mixtures, but in other cases they were two separate phases of orange and black colour. The mixtures could be identified as the corresponding binary, transition metal selenide, MSe or MSe_2 and $GeSe_2$. In the case of the separated phases, the black one was the transition metal selenide and the orange one was characterized as $GeSe_2$.

A different result was obtained in the experiments to synthesise $Fe_2Ge_2Se_6$ carried out at 600°C. Instead of the desired product the solid state reaction ended with the formation of two phases: a black one identified as Fe_2GeSe_4 [29] and orange one identified as $GeSe_2$ (Fig. 8.2a, 8.2b).

All experimental trials to synthesise new compounds with the general formula $M_2Si_2Te_6$ (M = Fe, Co, Ni) ended with homogeneous looking, black powders as reaction products. It was established, that irrespective of the reaction temperature the products represent mixtures of the corresponding binary, transition metal telluride, MTe_2 and unreacted Si and Te instead of $Co_2Si_2Te_6$, $SiTe_2$ instead of $Fe_2Si_2Te_6$ and Si_2Te_3 instead of $Ni_2Si_2Te_6$, respectively.

Regardless of the temperature all attempts to synthesise new tellurides with the general formula $M_2Ge_2Te_6$, possible new members of the $M_2X_2Y_6$ structure family, led to the formation of mixtures of the corresponding transition metal telluride, MTe_2 and GeTe, instead of the desired compounds.

The solid state reactions for the synthesis of $Cr_2Sn_2Te_6$ carried out at different temperatures ended with different products, non of them the desired compound. At 700°C, CrTe and SnTe could be identified, while at 1000°C, the products were Cr_2Te_3 and SnTe.
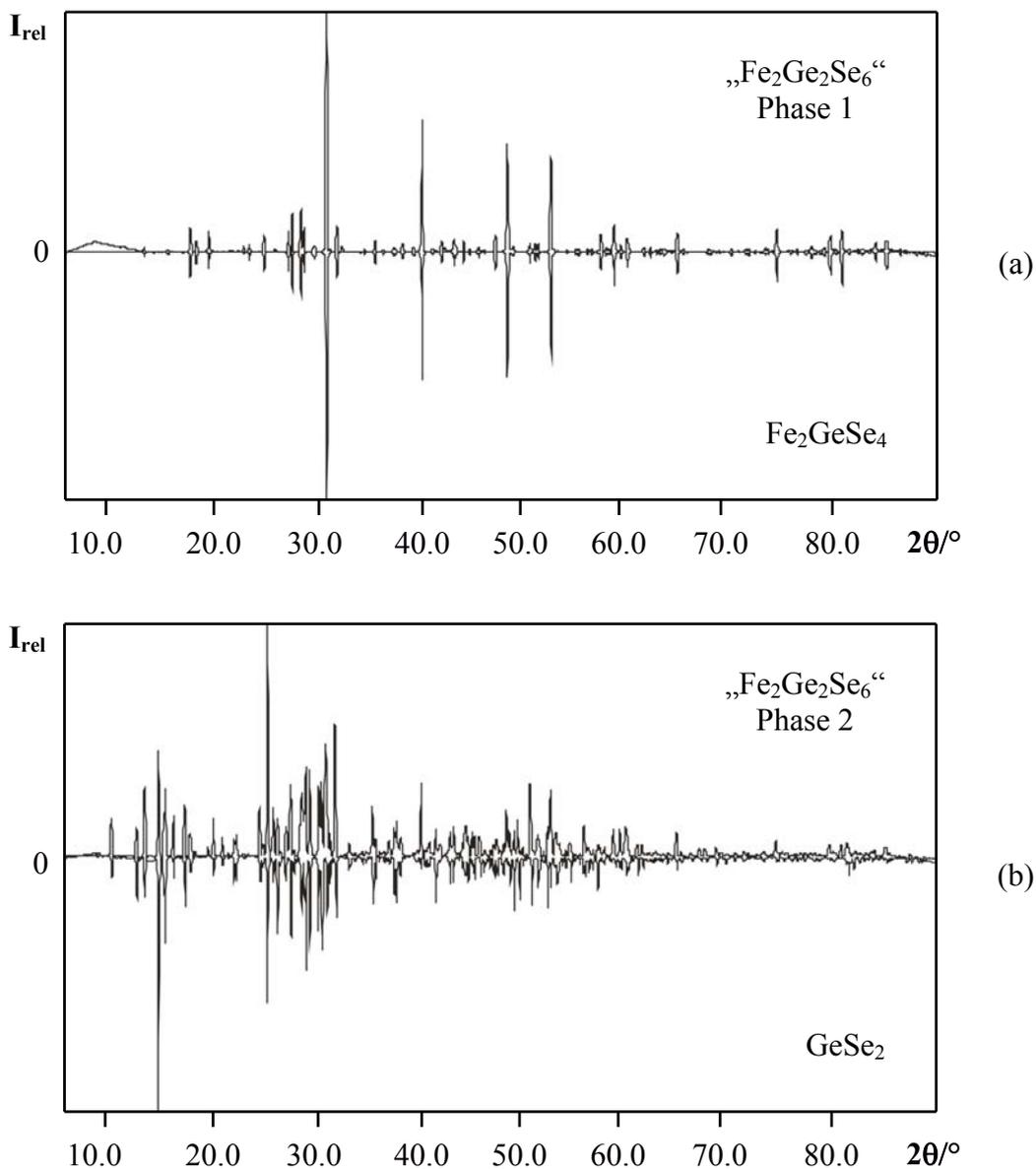
Fig. 8.2: Comparison between the measured powder patterns of phases 1 and 2 of "Fe$_2$Ge$_2$Se$_6$" synthesised at 600°C, and the calculated patterns of Fe$_2$GeSe$_4$ (a), and GeSe$_2$ (b)

8.3 Research on M_3BX_2 compounds

(M = transition metal, B = Si, Ge, Sn, X = Se, Te)

The successful synthesis of Fe_3GeTe_2 and Ni_3GeTe_2 gave rise to a series of investigations whose theme was the synthesis of new M_3BX_2 compounds of different compositions containing the first row transition metals Mn, Fe, Co, Cu and Zn. Except for one composition containing Se, all other experiments were carried out with Te as a chalcogen element (Tab. 8.3).

Table 8.3: Investigated M_3BX_2 compositions

Chemical content	Reaction temperature / °C	Reaction product
Mn_3GeTe_2	625; 700	MnTe + Ge + ?
Fe_3SiTe_2	625; 700; 800	$FeTe_2$ + Si + ?
Fe_3GeSe_2	625; 700	FeSe + $GeSe_2$ + ?
Fe_3SnTe_2	625; 700	FeTe + SnTe + ?
Co_3GeTe_2	625; 700	CoTe + GeTe + ?
Cu_3GeTe_2	700	Cu_2Te + GeTe + ?
Zn_3GeTe_2	625; 700; 800	ZnTe + GeTe + ?

In an attempt to synthesise new M_3BX_2 compounds, solid state reactions at temperatures of 625°C to 800°C were performed. Stoichiometric mixtures of the pure elements were filled in quartz glass ampoules, which after evacuation and sealing were annealed in a furnace for 14 days. The reaction products were characterized by X – ray powder diffraction.

Regardless of the temperature of the solid state reaction the experiments for the synthesis of new compounds with the general formula M_2BTe_3 ended with the formation of dark – grey to black powders, which are mixtures of the corresponding binary, transition metal telluride, MTe and the telluride of the fourth main group element, respectively.

The solid state reaction for the synthesis of Cu_3GeTe_2 was carried out only at a temperature of 700°C. The product contained Cu_2Te and GeTe.

A series of trials for the synthesis of Mn_3GeTe_2 ended with the formation of a product, which contained MnTe and unreacted Ge (Fig. 8.3).

Attempts to synthesise Fe_3SiTe_2 were unsuccessful too. For all temperatures, the product was a mixture of $FeTe_2$ and unreacted silicon.

Only one selenide, Fe_3GeSe_2, was attempted in the series of experiments reported here. After annealing at temperatures of 625°C and 700°C, respectively, the product contained two separate phases. The first, black one was FeSe. The second, orange in colour was characterized as $GeSe_2$.
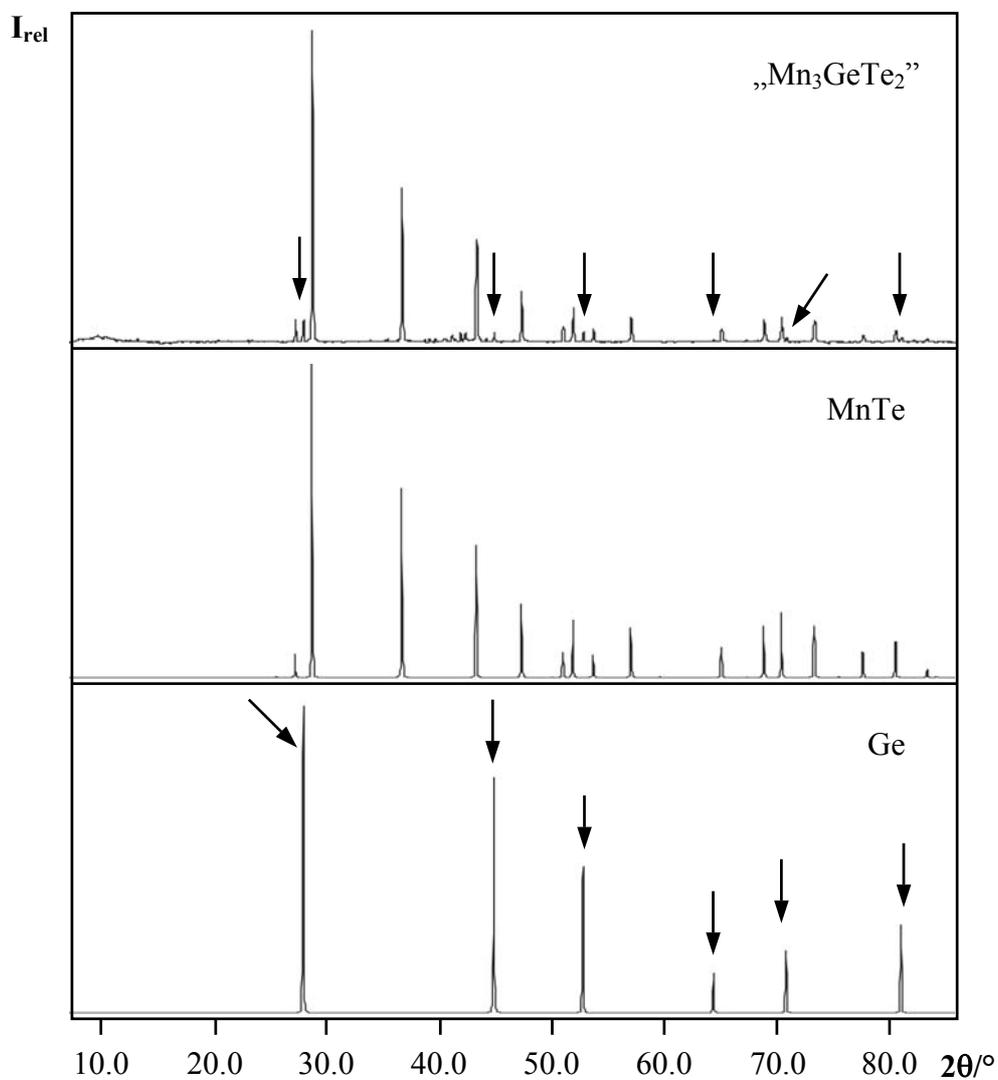
Fig. 8.3: Comparison between the measured powder pattern of "Mn3GeTe" synthesised at 700°C (top) and the calculated patterns of MnTe and Ge

9 Summary

This thesis is devoted to the synthesis, structure determination and investigation of the properties of new ternary compounds of the transition metals from the first transition series, Cr, Mn, Fe and Ni, and members of several structural families. The structural details of each of the structure types presented were thoroughly discussed in the corresponding chapters.

Mn_2GeSe_4 is a new compound, one of the rare transition metal selenides, which crystallizes in the olivine structure – type (orthorhombic, SG: *Pnma*) with lattice constants *a=1335.0(3) pm, b=776.5(2) pm, c=630.7(1) pm*. Its structure consists of a hexagonal close packing of selenium atoms, in which Mn occupies half of the octahedral sites and Ge occupies 1/8 of the tetrahedral holes. Analysis of the observed chemical bonds shows, that the Mn – Se distances are significantly shorter in comparison with the sum of the effective ionic radii. This is ascribed to the more covalent character of the Mn – Se bonds. In contrast, the Ge – Se distances are in a fairly good agreement with the sum of the ionic radii. Further study of the geometrical aspects of the structure revealed, that Mn_2GeSe_4 lies at the border between olivine and spinel structure – types. Therefore, a possible olivine – spinel transition for Mn_2GeSe_4 at high temperatures and pressures is presumable.

Magnetic measurements showed an antifferomagnetic behaviour of Mn_2GeSe_4 with a paramagnetic Curie temperature $\Theta = -240(5)$ K. At high temperatures, the inverse magnetic susceptibility curve follows the Curie – Weiss law. At lower temperatures, a deviation form the Curie – Weiss law accompanied by an abrupt drop in the curve is observed. This probably corresponds to a weak ferromagnetically ordered compound, saturated at high fields.

Investigations of transition metal chalcogenides with the general formula $M_2X_2Y_6$ (M = transition metal, X = Ge, Si, Y = chalcogen) ended with the synthesis of a new compound with the stoichiometric formula $Cr_2Ge_2Se_6$. Since the synthesis yields only powder samples, its structure is not yet determined. Thermoanalytical and X – ray powder diffraction characterization show an incongruently melting compound (melting point 646°C) with a hexagonal symmetry and lattice constants *a = b = 629.3(3) pm, c = 1942.1(6) pm, $\gamma = 120°$, V=666.1(5) $\times 10^6$ pm^3*. At high temperatures, it suffers only thermal expansion, but no phase transition.

Fe_3GeTe_2 and Ni_3GeTe_2 are the first ternary germanides belonging to the filled NiAs – structures. Both crystallize hexagonally in the space group *P6₃/mmc* and lattice constants *a=b=399.1(1) pm, c=1633.6(3) pm* for Fe_3GeTe_2 and *a=b=319.1(1) pm, c=1602.2(3) pm* for Ni_3GeTe_2, respectively. Their crystal structure is defined by alternating layer packages separated with a van der Waals gap. Every layer package consists of five layers: 1. Te layer, 2. Fe (Ni) layer, 3. mixed Fe(Ni) – Ge layer, 4. Fe(Ni) layer. 5. Te layer. A very special feature of the structure is, that the positions of the transition metal atom within the mixed Fe(Ni) – Ge layer is not fully occupied. This is a common feature of the filled NiAs – phases. Only binary compounds, among them $Fe_{1,67}Ge$ and $Ni_{1,67}Ge$ with this structure type are known so far. Ni_3GeTe_2 can be considered as a compound with a modified filled NiAs – structure, because of the additional electron density maximum, which appears in the van der Waals gap. It is assumed to be an octahedrally coordinated Ni atom. Its position is also not fully occupied (*sof.* = 0.3). The sum of both partly occupied Ni positions is equal to unity and this makes the agreement between the results of the structure refinement and the WDX investigation excellent.

The influence of the not fully occupied iron position in Fe_3GeTe_2 is not yet clarified. Simulated precession images of sections of its structure revealed appearance of weak interstitial reflections ordered in a row – like manner between the main reflections. This was first ascribed to the presence of a superstructure or to a stacking fault as a result of the partly occupied iron position in the mixed Fe – Ge layer. Thorough inspection of the simulated precession pictures showed a strong and troublesome $\lambda/2$ effect, a mosaic structure and the existence of powder regions inside the investigated crystal.

Despite the close relationship between structures, the magnetic properties of Fe_3GeTe_2 and Ni_3GeTe_2 are quite different. The first one is characterized by a predominance of ferromagnetic interactions with a Curie temperature T_c= 231 K. At temperatures above 250K, the inverse magnetic susceptibility curve follows the Curie – Weiss law, but after 300K a deviation from is observed. This is ascribed to the domain structure of the ferromagnetic materials and is a trend, which is observed in many ferromagnetic compounds.

In contrast, Ni_3GeTe_2 possesses very weak, temperature independent paramagnetism.

The simple titration method used for the preparation of hydroxylapatite ($Ca_{10}(PO_4)_6(OH)_2$) particles with expected nanoscale size leads to the formation of hydroxylapatite powders with a particle size in the range 180 – 300 nm. A certain number of crystals with sizes between 60 nm and 90 nm (i. e. in the nanorange) are also found in the products, but their amount

compared to the amount of the bulk is very small. Increasing of the concentration of the initial water solutions used for the titration ((NH_4)$_2$$HPO_4$ and $CaCl_2$, respectively) results in the formation of brushite ($CaHPO_4 \cdot 2H_2O$) crystals which are 1 μm in size, instead of hydroxylapatite nanocrystals. The temperature treatment of the hydroxylapatite powders causes their transformation into calcium orthophosphate, but no reduction of the crystal size.

The ternary transition metal compounds Mn_2GeSe_4, $Cr_2Ge_2Se_6$, Fe_3GeTe_2 and Ni_3GeTe_2, as well as the hydroxylapatite particles prepared and characterized in the course of this work open a new field for experimental studies and investigations of the properties of these compounds, which can play an important role in science and technology in the future.

10 References

[1]   Miller, O., Roy, R.:

"The Major Ternary Structural Families"

Springer – Verlag Berlin Heidelberg New York (1974) 17

[2]   Bragg, W. L., Brown, G. B.:

"Die Struktur des Olivins"

Z. Kristallogr. **63** (1926) 538 – 556

[3]   West, A. R.:

"Solid State Chemistry and Its Applications"

John Wiley & Sons Ltd., New York (1984)

[4]   Ouvrard, G., Sandre, E., Brec, R.:

"Synthesis and Crystal Structure of a New Layered Phase: The Chromium

Hexatellurosilicate $Cr_2Si_2Te_6$"

J. Solid State Chem. **73** (1988) 27 – 32

[5]   Siberchicot, B., Jobic, S., Carteaux, V., Gressier, P., Ouvrard, G.:

"Band Structure Calculations of Ferromagnetic Chromium Tellurides $CrSiTe_3$ and

$CrGeTe_3$"

J. Phys. Chem. **100** (1996) 5863 – 5867

[6]   Sandre, E., Carteaux, V., Marie, A. M., Ouvrard, G.:

"Structural determination of a new lamellar tellurosilicate, $AlSiTe_3$"

J. Alloys Compd. **204** (1994) 145 – 149

[7]   Vincent, H., Leroux, D., Bijaoui, D., Rimet, R., Schlenker, C.:

"Crystal Structure of $Mn_3Si_2Te_6$"

J. Solid State Chem. **63** (1986) 349 – 352

[8]   Carteaux, V., Brunet, D., Ouvrard, G., Andre, G.:

"Crystallographic, magnetic and electronic structures of a new layered ferromagnetic compound $Cr_2Ge_2Te_6$"

J. Phys.: Condens. Matter **7** (1995) 69 – 87

[9]   Abrikosov, N. Kh., Bagaeva, L. A., Dudkin, L. D., Petrova, L. I., Sokolova, V. M.:

"Phase Equilibria in the Fe – Ge – Te System"

Izvestiya Akad. Nauk. Neorg. Mat. **21(10)** (1985) 1680 – 1686

[10]   Nuffield, E. W.:

"X – ray Diffraction Methods"

John Wiley & Sons, Inc., New York (1966) 53

[11]   Woolfson, M. M.:

"An Introduction to X – ray Crystallography"

Cambridge University Press, London (1970) 63

[12]   Massa, W.:

"Crystal Structure Determination"

Springer – Verlag, Berlin Heidelberg (2000)

[13]   STOE WinXPOW Version 1.08

"Stoe Powder Diffraction Software"

STOE & Cie GmbH, Darmstadt, 2000

[14]   X – AREA

"Software Package for Data Collection and Evaluation"

STOE & Cie GmbH, Darmstadt, 2000

[15]   X – PREP

"Reciprocal Space Exploration" Version 4.0 for MSDOS

Siemens, Karlsruhe, 1989

[16]   STOE X – RED Version 1.19
        "Data Reduction Program"
        STOE & Cie GmbH, Darmstadt, 1999

[17]   STOE X – SHAPE Version 1.06
        "Crystal Optimisation for Numerical Absorption Correction"
        STOE & Cie GmbH, Darmstadt, 1999

[18]   SHELXS – 97
        "Program for the Solution of Crystal Structures"
        Sheldrick, G. M., University of Göttingen, 1997

[19]   SHELXL – 97
        "Program for Structures Refinement"
        Sheldrick, G. M., University of Göttingen, 1997

[20]   DIAMOND Version 2.1e
        "Informationssystem für Kristallstrukturen"
        Crystal Impact GbR, Bonn, 2001

[21]   LINSEIS Version 2.18
        "Datenauswertung für Windows"
        Selb, 1991 – 1993

[22]   Weidlein, J., Müller, U., Dehnicke, K.:
        "Schwingungsspektroskopie", 2 überarbeitete Auflage
        Georg Thieme Verlag, Stuttgart – New York (1988) 12

[23]   OPUS/IR Version 2.2
        "Spektroskopiesoftware"
        Bruker Analytische Messtechnik GmbH, Karlsruhe, 1991

[24] Tranqui, D., Vincent, H., Beratut, E. F., Qui, V. V.:

"Etude par Diffraction Neutronique de la Structure Nucleaire Magnetique de

L'orthothiogermanate de Manganese"

Solid State Communications **7** (1969) 641 – 645

[25] Creer, J. G., Troup, G. J. F.:

"The Crystal and Magnetic Structure of Mn_2GeO_4"

Solid State Communications **8** (1970) 1183 – 1188

[26] Fuhrmann, J., Pickardt, J.:

"Structure of Mn_2SiS_4"

Acta Cryst. **C45** (1989) 1808 – 1809

[27] Santoro, R. P., Newnham, R. E., Nomura, S.:

"Magnetic Properties of Mn_2SiO_4 and Fe_2SiO_4"

J. Phys. Chem. Solids **27** (1966) 655 – 666

[28] Lamarche, A. M., Lamarche, G., Church, C., Woolley, J. C., Swainson, I. P., Holden, T. M.:

"Neutron diffraction study of magnetic phases in polycrystalline Mn_2SiS_4"

J. Magn. Mag. Mat. **137** (1994) 305 – 312

[29] Henao, J. A., Delgado, J. M.:

"X – ray powder diffraction data and structural study of Fe_2GeSe_4"

Powder Diffraction **13(4)** (1998) 196 – 201

[30] Jobic, S., Bodenan, F., Le Boterf, P., Ouvrard, G.:

"Structure refinement and magnetic behaviour of the only selenide in the olivine group

family: Mn_2SiSe_4"

J. Alloys Compd. **230** (1995) 16 – 22

[31] Bodenan, F., Cajipe, V. B., Ouvrard, G., Andre, G.:

"Low – temperature magnetic structure of olivine Mn_2SiSe_4"

J. Magn. Mag. Mat. **164** (1996) 233 – 240

[32] Elliott, N.:

      "The Crystal Structure of Manganese Diselenide and Manganese Ditelluride"

      J. Am. Chem. Soc. **59** (1937) 1958 – 1962

[33] Shannon, R. D.:

      "Revised Effective Ionic Radii and Systematic Studies of Interatomic Distances in

      Halides and Chalcogenides"

      Acta Cryst. **A32** (1976) 751 – 767

[34] Vincent, H., Bertaut, E. F., Baur, W. H., Shannon, R. D.:

      "Polyhedral Deformations in Olivine – Type Compounds and the Crystal Structure of

      Fe_2SiS_4 and Fe_2GeS_4"

      Acta Cryst. **B32** (1976) 1749 – 1755

[35] Dittmar, G., Schäfer, H.:

      "Die Kristallstruktur von Germaniumdiselenide"

      Acta Cryst. **B32** (1976) 2726 – 2728

[36] Dutta, S. N., Jeffrey, G. A.:

      "On the Structure of Germanium Selenide and Related Binary IV/VI Compounds"

      Inorganic Chemistry **4(9)** (1965) 1363 – 1366

[37] Baroni, A.:

      "Sul polimorfismo di MnSe"

      Z. Kristallogr. **99** (1938) 336 – 339

[38] Hoppe, R.:

      "On the Madelung Part of Lattice Energy"

      Z. Naturforsch. **50a** (1995) 555 – 567

[39] Hoppe, R.:

      "Über Madelungfaktoren"

      Angew. Chem. **78(1)** (1966) 52 – 63

[40]   MAP 4

"Program for Calculation of the Madelung Part of the Lattice Energy"

[41]   Rooymans, C. J. M., Rabenau, A.:

"Crystal Chemistry"

North − Holland Publishing Company, Amsterdam − Oxford (1975) 127

[42]   Johnston, W. D., Heikes, R. R.:

"A Study of the System $Li_xMn_{(1-x)}Se$"

J. Am. Chem. Soc. **80** (1958) 5904 − 5907

[43]   Vincent, H., Bertaut, E. F.:

"Etude Cristallographique et Magnetique de Fe_2GeS_4 Structures Magnetiques a 85 et 4,2°K"

J. Phys. Chem. Solids **34** (1973) 151 − 158

[44]   Cox, D. E., Frazer, B. C., Newnham, R. E., Santoro, R. P.:

"Neutron Diffraction Investigation of the Spiral Magnetic Structure in Cr_2BeO_4"

J. Appl. Phys. **40(3)** (1969) 1124 − 1125

[45]   Santoro, R. P., Newnham, R. E.:

"Magnetic Properties of Chromium Chrysoberyl"

J. Am. Ceram. Soc. **47(10)** (1964) 491 − 492

[46]   Santoro, R,. P., Newnham, R. E.:

"Antiferromagnetism in $LiFePO_4$"

Acta Cryst. **22** (1967) 344 − 347

[47]   Kondo, H., Miyahara, S.:

"Magnetic Properties of Some Synthetic Olivines"

J. Phys. Soc. Japan **18** (1963) 305

[48]   Hagemann, I. S., Khalifah, P. G., Ramirez, A. P., Cava, R. J.:
        "Geometric magnetic frustration in olivines"
        Phys. Rev. B **62(2)** (2000) R771 – R774

[49]   Cococcioni, M., Dal Corso, A., de Gironcoli, S.:
        "Structural, electronic and magnetic properties of Fe_2SiO_4 fayalite: Comparison of
        LDA and GGA results"
        Phys. Rev. B **67** (2003) 094106-1 – 094106-7

[50]   Rousse, G., Rodriguez – Carvajal, J., Patoux, S., Masquelier, C.:
        "Magnetic Structures of the Triphylite $LiFePO_4$ and of Its Delithiated Form $FePO_4$"
        Chem. Mater. **15** (2003) 4082 – 4090

[51]   Silvera, I. F., Thornley, J. H. M., Tinkham, M.:
        "Magnetic Properties of the Canted Antiferromagnet $\alpha – CoSO_4$"
        Phys. Rev **136(3A)** (1964) A695 – A710

[52]   Heeger, A. J., Beckman, O., Portis, A. M.:
        "Magnetic Properties of $KMnF_3$. II. Weak Ferromagnetism"
        Phys. Rev. **123(5)** (1961) 1652 – 1660

[53]   Klingen, W., Ott, R., Hahn, H.:
        "Über die Darstellung und Eigenschaften von Hexathio- und
        Hexaselenohypodiphosphaten"
        Z. Anorg. Allg. Chem. **396** (1973) 271 – 278

[54]   Klingen, W., Eulenberger, G., Hahn, H.:
        "Über die Kristallstrukturen von $Fe_2P_2Se_6$ und $Fe_2P_2S_6$"
        Z. Anorg. Allg. Chem. **401** (1973) 97 – 112

[55]   Ouvrard, G., Brec, R., Rouxel, J.:
        "Structural Determination of Some MPS_3 Layered Phases (M = Mn, Fe, Co, Ni and
        Cd)"
        Mat. Res. Bull. **20** (1985) 1181 – 1189

[56]   Brec, R., Ouvrard, G., Rouxel., J.:

"Relationship Between Structure Parameters and Chemical Properties in Some MPS_3

Layered Phases"

Mat. Res. Bull. **20** (1985) 1257 – 1263

[57]   Brec, R., Ouvrard, G., Louisy, A., Rouxel, J.:

"Proprietes Structurales de Phases $M^{II}PX_3$ (X = S, Se)"

Ann. Chim. Fr. **5** (1980) 499 – 512

[58]   Jandali, M. Z., Eulenberger, G., Hahn, H.:

"Die Kristallstrukturen von $Hg_2P_2S_6$ und $Hg_2P_2Se_6$"

Z. Anorg. Allg. Chem. **447** (1978) 105 – 118

[59]   Ouvrard, G., Freour, R., Brec, R., Rouxel, J.:

"A Mixed Valence Compound in the Two Dimensional MPS_3 Family: $V_{0.78}PS_3$.

Structure and Physical Properties"

Mat. Res. Bull. **20** (1985) 1053 – 1062

[60]   Prouzet, E., Ouvrard, G., Brec, R.:

"Structure Determination of $ZnPS_3$"

Mat. Res. Bull. **21** (1986) 195 – 200

[61]   Wiedenmann, A., Rossat – Mignod, J., Louisy, A., Brec, R., Rouxel, J.:

"Neutron Diffraction Study of the Layered Compounds $MnPSe_3$ and $FePSe_3$"

Solid State Communications **40(12)** (1981) 1067 – 1072

[62]   Boucher, F., Evain, M., Brec, R.:

"Second – order Jahn – Teller effect in $CdPS_3$ and $ZnPS_3$ demonstrated by a non –

harmonic behaviour of Cd^{2+} and Zn^{2+} d^{10} ions"

J. Alloys. Compd. **215** (1994) 63 – 70

[63]   Kanematsu, K., Yasukochi, K, Ohoyama, T.:

"Magnetic Properties of $(Fe, Co)_{1.67}Ge$ and $(Fe, Ni)_{1.67}Ge$

J. Phys. Soc. Japan **18(10)** (1963) 1429 – 1436

[64]   Yasukochi, K., Kanematsu, K, Ohoyama, T.:

       "Magnetic Properties of Intermetallic Compounds in Iron – Germanium System:

       $Fe_{1.67}Ge$ and $FeGe_2$"

       J. Phys. Soc. Japan **16(3)** (1961) 429 – 433

[65]   Kanematsu, K., Ohoyama, T.:

       "Magnetic and X – Ray Studies of Iron – Germanium System. II. Phase Diagram and

       Magnetism of Each Phase"

       J. Phys. Soc. Japan **20(2)** (1965) 236 – 242

[66]   Maier, J., Wachtel, E.:

       "Konstitution und magnetische Eigenschaften von B–B–Metall– und Eisen–B–Metal–

       Legierungen"

       Z. Metallkde. **63(7)** (1972) 411 – 418

[67]   Wiedemeier, H., Siemers, P. A.:

       "The Thermal Expansion of GeS and GeTe"

       Z. Anorg. Allg. Chem. **431** (1977) 299 – 304

[68]   Richardson, M.:

       "Crystal Structure Refinements of the B 20 and Monoclinic (CoGe – type)

       Polymorphs of FeGe"

       Acta Chem. Scand. **21** (1967) 753 – 760

[69]   Havinga, E. E., Damsma, H., Hokkeling, P.:

       "Compound and Pseudo – Binary Alloys with the $CuAl_2$ (C16) – Type Structure. I.

       Preparation and X – ray Results"

       J. Less – Common Metals **27** (1972) 169 – 186

[70]   Havinga, E. E.:

       "Compound and Pseudo – Binary Alloys with the $CuAl_2$ (C16) – Type Structure. II.

       Theoretical Discussion of Crystallographic Parameters"

       J. Less – Common Metals **27** (1972) 187 – 193

[71]   Ellner, M.:

"Über die Kristallchemischen Parameter der Ni- , Co-, und Fe – Haltigen Phasen vom

NiAs – Typ"

J. Less – Common Metals **48** (1976) 21 – 52

[72]   Brostigen, G., Kjekshus, A.:

"Compounds with the Marcasite Type Crystal Structure"

Acta Chem. Scand. **24** (1970) 1925 – 1940

[73]   Oftedal, I.:

"Röntgenographische Untersuchungen von Manganarsenid, Eisentellurid,

Nicklestannid und Platinstannid"

Z. Phys. Chemie **132** (1927) 208 – 216

[74]   Laves, F., Wallbaum, H. J.:

"Über einige neue Vetreter des NiAs – Typs und ihre kristallchemische Bedeutung"

Z. Angew. Miner. **4** (1942) 17 – 46

[75]   Ellner, M., Gödecke, T., Schubert, K.:

"Zur Struktur der Mischung Nickel – Germanium"

J. Less – Common Metals **24** (1971) 23 – 40

[76]   Furuseth, S., Selte, K., Kjekshus, A.:

"Redetermined Crystal Structures of $NiTe_2$, $PdTe_2$, PtS_2, $PtSe_2$ and $PtTe_2$"

Acta Chem. Scand. **19(1)** (1965) 257 – 258

[77]   Röst, E., Vestersjö, E.:

"On the System Ni – Se – Te"

Acta Chem. Scand. **22(7)** (1968) 2118 – 2134

[78]   Kjekshus, A., Rakke, T.:

"Compounds with the Marcasite Type Crystal Structure. XI. High Temperature

Studies of Chalcogenides

Acta Chem. Scand. **A29** (1975) 443 – 452

[87]   Utamapanya, S., Klabunde, K. J., Schlup, J. R.:
       "Nanoscale Metal Oxide Particles/Clusters as Chemical Reagents. Synthesis and
       Properties of Ultrahigh Surface Area Magnesium Hydroxide and Magnesium Oxide"
       Chem. Mater. **3** (1991) 175 – 181

[88]   Liu, X., Wang, X., Zhang, J., Hu, X., Lu, L.:
       "A study of nanocrystalline TiO_2 preparation with inorganotitanates and gelatin
       dispersant: thermal analysis of complex gel"
       Thermochimica Acta **342** (1999) 67 – 72

[89]   Liu, X., Wang, H., Chen, D., Wang, Y Lu, L., Wang, X.:
       "Study of Nanocrystalline TiO_2 Prepared with Raw and Modified Gelatin Dispersants"
       J. Appl. Polymer Sci. **73(13)** (1999) 2569 – 2574

[90]   Fröba, M., Reller, A.:
       "Synthesis and Reactivity of Functional Metal Oxides in Nanoscopic Systems"
       Prog. Solid St. Chem. **27** (1999) 1 – 27

[91]   Xiong, G., Wang, X., Lu, L., Yang, X., Xu, Y.:
       "Preparation and Characterization of $Al_2O_3 - TiO_2$ Composite Oxide Nanocrystals"
       J. Solid State Chem. **141** (1998) 70 – 77

[92]   Rao. C. N. R., Kulkarni, G. U., Thomas, P. J., Edwards, P. P.:
       "Size – Dependent Chemistry: Properties of Nanocrystals"
       Chem. Eur. J. **8(1)** (2002) 29 – 35

[93]   Sprycha, R., Matijevic, E.:
       "Electrokinetics of Uniform Colloidal Dispersions of Chromium Hydroxide"
       Langmuir **5** (1989) 479 – 485

[94]   Lu, K., Zhang, H. Y.:
       "Grain size dependence of mechanical properties in nanocrystalline selenium"
       J. Mater. Res. **12(4)** (1997) 923 – 930

[95]   Talapin, D. V., Rogach, A. L., Kornowski, A., Haase, M., Weller, H.:
"High Luminescent Monodisperse CdSe and CdSe/ZnS Nanocrystals Synthesized in a
Hexadecacylamine – Trioctylphosphine Oxide – Trioctylphosphine Mixture"
Nanoletters **4(1)** (2001) 207 – 211

[96]   Ducamp – Sanguesa, Herrera – Urbina, R., Figlarz, M.:
"Synthesis and Characterisation of Fine and Monodisperse Silver Particles of Uniform
Shape"
J. Solid State Chem. **100** (1992) 272 – 280

[97]   Huang, C. Y., Sheen, S. R.:
"Synthesis of nanocrystalline and monodisperse copper particles of uniform spherical
shape"
Mat. Letters **30** (1997) 357 – 361

[98]   Rao, C. N. R., Kulkarni, G. U., Thomas, P. J., Edwards, P. P.:
"Metal nanoparticles and their assemblies"
Chem. Soc. Rev. **29** (2000) 27 – 35

[99]   Finnel, A. J., Bonner, C. E.:
"Synthesis and Spectroscopic Characterization of Cadmium Sulfide Nanocrystals"
Proceedings NOBCChE **24** (1997) 119 – 125

[100]   Ekimov, A.:
"Growth and optical properties of semiconductor nanocrystals in a glass matrix"
J. Luminescence **70** (1996) 1 – 20

[101]   Peytcheva, A., Antonietti, M.:
"Ortsspezifische Auflösung von Calciumphosphat mit Polymeren: Schnitzen auf der
Nanoscala"
Angew. Chem. **113(18)** (2001) 3484 – 3488

[102]   Sedlak, M., Antonietti, M., Cölfen, H.:
        "Synthesis of a new class of double – hydrophilic block copolymers with calcium
        binding capacity as builders biomimetic structure control of minerals"
        Macromol. Chem. Phys. **199** (1998) 247 – 254

[103]   Lim, G. K., Wang, J., Ng, S. C., Gan, L. M.:
        "Formation of Nanocrystalline Hydroxyapatite in Nonionic Surfactant Emulsions"
        Langmuir **15** (1999) 7472 – 7477

[104]   Lim, G. K., Wang, J., Ng, S. C., Gan, L. M.:
        "Processing of fine hydroxyapatite powders via an inverse microemulsion route"
        Mat. Letters **28** (1996) 431 – 436

[105]   Lim, G. K., Wang, J., Ng, S. C., Chew, C. H., Gan, L. M.:
        "Processing of hydroxyapatite via microemulsion and emulsion routes"
        Biomaterials, **18(21)** (1997) 1433 – 1439

[106]   Geesink, R. G. T., Manley, M. T.:
        "Hydroxyapatite Coatings in Orthopaedic Surgery"
        Raven Press, New York (1995)

[107]   Takaoka, T., Okumura, M., Ohgushi, H., Inone, K., Takakura, Y., Tamai, S.:
        "Histological and biochemical evaluation of osteogenic response in porous
        hydroxyapatite coated alumina ceramics"
        Biomaterials, **17(15)** (1996), 1499 – 1505

[108]   Reichert, J., Binner, J. G. P.:
        "An evaluation of hydroxyapatite – based filters for removal of heavy metal ions from
        agueous solutions"
        J. Mater. Sci. **31(5)** (1996) 1231 – 1241

[109]   Nviagu, J. O., Moore, P. B.:
        "Phosphate Minerals"
        Springer – Verlag, Berlin – Heidelberg (1984) Chapter 11

[110] Kanazs, T.:

"Materials Science Monographs: Inorganic Phosphate Materials"

Elsevier, New York (1989) Chapter 2

[111] Schellenschläger, V.:

"Schwingungsspektroskopische Untersuchungen an festen Hydraten"

PhD Dissertation, Siegen (2001)

[112] Nyquist, R. A., Kagel, R. O.:

"The Handbook of Infrared and Raman Spectra of Inorganic Compounds and Organic

Salts (a 4 – volume set)"

Academic Press Inc., San Diego (1997) 492

[113] Ikoma, T., Yamazaki, A., Nakamura, S., Akao, M.:

"Preparation and Structure Refinement of Monoclinic Hydroxyapatite"

J. Solid State Chem. **144** (1999) 272 – 276

[114] Jost, K. –H.:

"Röntgenbeugung an Kristallen"

Heyden & Son GmbH, Rheine (1975) 390

[115] Neff, H.:

"Grundlagen und Anwendung der Röntgen – Feinstruktur – Analyse"

R. Oldenburg, München (1962) 294

[116] El Hichou, A., Bougrine, A., Bubendorff, J. L., Ebothe, J., Addou, M., Troyon, M.:

"Structural, optical and cathodoluminescence characteristics of sprayed undoped and

fluorine – doped ZnO thin films"

Semicond. Sci. Technol. **17** (2002) 607 – 613

[117] Bardet, E., Bouree, J. E., Cuniot, M., Dixmier, J., Elkaim, P., Le Duigou, J., Middya, A. R., Perrin, J.:
"The grain size in microcrystalline silicon: correlation between atomic force microscopy, UV reflectometry, ellipsometry, and X – ray diffractometry"
J. Non – Cryst. Solids **198 – 200** (1996) 867 – 870

[118] Kay, M. I., Young, R. A., Posner, A. S.:
"Crystal Structure of Hydroxyapatite"
Nature **204(12)** (1964) 1050 – 1052

[119] Posner, A. S., Perloff, A., Diorio, A. F.:
"Refinement of the hydroxyapatite structure"
Acta Cryst. **11** (1958) 308 – 309

[120] Aslanian, S., Stoilova, D., Petrova, R.:
"Isodimorphe Substitution im $CaSO_4 - CaHPO_4 - H_2O$ System"
Z. Anorg. Allg. Chem. **465** (1980) 209 – 220

[121] Jones, D. W., Smith, J. A. S.:
"The Structure of Brushite, $CaHPO_4, 2H_2O$"
J. Chem. Soc., Abstracts (1962) 1414 – 1420

[122] Beevers, C. A.:
"The Crystal structure of Dicalcium Phosphate Dihydrate, $CaHPO_4 \cdot 2H_2O$"
Acta Cryst. **11** (1958) 273 – 277

[123] LeGeros, R. Z., LeGeros, J. P.:
"Brushite Crystals Grown by Diffusion in Silica Gel and in Solution"
J. Cryst. Growth **13/14** (1972) 476 – 480

[124] Ohta, M., Tsutsumi, M., Ueno, S.:
"Observations of Etch Pits on As – Grown Faces of Brushite Crystals"
J. Cryst. Growth **47** (1979) 135 – 136

[125]   Ohta, M., Tsutsumi, M.:

"The Relationship Between the Morphology of Brushite Crystals Grown Rapidly in Silica Gel and Its Structure"

J. Cryst. Growth **56** (1982) 652 – 658

[126]   Aleksandrov, K. I.:

Personal investigations

Siegen (2002 – 2003)

Publications

Deiseroth, H. J., Aleksandrov, K., Kremer, R. K.:

Structural and Magnetic Properties of Mn_2GeSe_4

Z. anorg. allg. Chem. **631** (2005) 448 – 450

Posters

9th European Conference on Solid State Chemistry

The crystal structure of Mn_2GeSe_4, Stuttgart 2003

12 Vortragstagung Wöhler – Vereinigung für Anorganische Chemie der GDCh

Structure, real structure and properties of Fe_3GeTe_2 and Ni_3GeTe_2, Marburg 2004

11 Appendix

11.1 Data for Mn$_2$GeSe$_4$

Table 11.1: List of the observed reflections for Mn$_2$GeSe$_4$ (indexed orthorhombic, see 4.3)

h	k	l	Int. / %	d$_{obs}$ / Å	d$_{calc}$ / Å	h	k	l	Int. / %	d$_{obs}$ / Å	d$_{calc}$ / Å
2	0	0	17.3	6.7050	6.6995	3	0	3	10.3	1.9076	1.9074
2	1	0	29.5	5.0802	5.0808	3	1	3	11.8	1.8527	1.8528
0	1	1	20.9	4.9130	4.9131	7	0	1	11.0	1.8323	1.8322
1	1	1	19.2	4.6091	4.6128	2	2	3	46.7	1.7878	1.7879
2	1	1	14.2	3.9634	3.9619	4	1	3	10.0	1.7400	1.7400
0	2	0	15.7	3.8974	3.8975	6	2	2	15.5	1.6525	1.6524
3	0	1	19.4	3.6488	3.6490	7	0	2	11.8	1.6375	1.6378
2	2	0	18.9	3.3684	3.3689	4	4	1	19.8	1.6278	1.6278
3	1	1	32.1	3.3047	3.3049	8	0	1	12.4	1.6192	1.6191
1	2	1	35.0	3.2213	3.2213	0	0	4	15.6	1.5822	1.5821
0	0	2	25.7	3.1640	3.1642	4	4	2	15.1	1.4869	1.4869
1	0	2	13.4	3.0783	3.0795	8	0	2	12.0	1.4804	1.4803
2	2	1	100.0	2.9734	2.9738	7	4	1	9.6	1.3349	1.3349
1	1	2	20.3	2.8644	2.8641	4	4	3	17.1	1.3163	1.3163
3	0	2	13.0	2.5819	2.5819	8	0	3	12.4	1.3117	1.3117
5	0	1	11.4	2.4674	2.4677	2	6	1	11.7	1.2503	1.2503
1	2	2	11.5	2.4164	2.4163	8	2	3	11.6	1.2429	1.2432
2	2	2	62.2	2.3064	2.3064	0	4	4	12.3	1.2283	1.2283
2	3	1	11.4	2.2624	2.2624	6	2	4	15.0	1.2255	1.2255
4	1	2	14.2	2.2063	2.2062	3	4	4	12.5	1.1845	1.1843
3	2	2	14.1	2.1524	2.1525	8	4	2	11.4	1.1788	1.1788
3	3	1	14.3	2.1165	2.1166	8	5	1	12.7	1.1229	1.1230
4	3	0	11.6	2.0532	2.0531	5	2	5	9.9	1.0980	1.0981
1	3	2	12.3	1.9855	1.9859						
5	1	2	13.1	1.9782	1.9780						
0	4	0	32.5	1.9487	1.9488						
6	2	0	50.3	1.9377	1.9376						

Table 11.2: List of the observed reflections for Mn_2GeSe_4 at temperature 600°C (indexed

orthorhombic. see 4.3)

h	k	l	Int. / %	d_{obs} / Å	d_{calc} / Å
2	1	0	26.0	5.1248	5.1238
0	1	1	13.0	4.9512	4.9495
1	1	1	12.7	4.6437	4.6472
0	2	0	9.4	3.9343	3.9335
3	0	1	12.9	3.6746	3.6758
2	2	0	13.5	3.3965	3.3989
3	1	1	34.1	3.3306	3.3302
1	2	1	35.5	3.2476	3.2483
0	0	2	23.0	3.1821	3.1839
2	2	1	100.0	2.9985	2.9985
1	1	2	20.5	2.8863	2.8833
2	2	2	62.5	2.3232	2.3236
4	1	2	9.3	2.2218	2.2220
3	2	2	11.3	2.1669	2.1686
3	3	1	8.1	2.1346	2.1348
5	1	2	9.5	1.9919	1.9925
0	4	0	30.3	1.9668	1.9668
6	2	0	80.7	1.9545	1.9536
3	1	3	7.1	1.8653	1.8651
2	2	3	57.6	1.7998	1.8003
4	1	3	6.3	1.7527	1.7518
3	2	3	13.8	1.7269	1.7253
6	2	2	17.0	1.6655	1.6651
4	4	1	21.4	1.6421	1.6420
5	1	3	16.3	1.6327	1.6326
8	1	1	6.6	1.5972	1.5977
0	0	4	12.6	1.5916	1.5919

Table 11.3: List of the observed reflections for Mn_2GeSe_4 at temperature 700°C (indexed orthorhombic. see 4.3)

h	k	l	Int. / %	d_{obs} / Å	d_{calc} / Å
2	1	0	27.3	5.1284	5.1338
0	1	1	13.9	4.9560	4.9552
1	1	1	16.4	4.6449	4.6529
2	2	0	14.5	3.4046	3.4058
3	1	1	39.7	3.3357	3.3353
1	2	1	31.2	3.2535	3.2537
0	0	2	16.2	3.1849	3.1855
2	2	1	100.0	3.0033	3.0035
4	0	1	85.7	2.9872	2.9875
1	1	2	32.3	2.8890	2.8855
2	2	2	56.8	2.3264	2.3265
0	4	0	36.5	1.9705	1.9709
6	2	0	81.4	1.9585	1.9573
2	2	3	52.4	1.8022	1.8020
4	1	3	12.2	1.7530	1.7535
3	2	3	16.5	1.72671	1.7271
6	2	2	16.7	1.6677	1.6677
4	4	1	21.8	1.6454	1.6451
8	0	1	14.3	1.6343	1.6346
8	1	1	25.0	1.6002	1.6006

Table 11.4: List of the observed reflections for Mn_2GeSe_4 at temperature 750°C (indexed orthorhombic. see 4.3)

h	k	l	Int. / %	d_{obs} / Å	d_{calc} / Å
2	1	0	20.5	5.1350	5.1355
0	1	1	11.3	4.9531	4.9563
3	0	1	15.9	3.6807	3.6831
2	2	0	17.9	3.4069	3.4061
3	1	1	29.3	3.3371	3.3368
1	2	1	38.7	3.2554	3.2539
2	2	1	100.0	3.0046	3.0040
1	1	2	28.6	2.8888	2.8866
2	2	2	68.6	2.3270	2.3271
3	2	2	15.8	2.1712	2.1722
3	3	1	12.1	2.1387	2.1390
0	4	0	37.6	1.9706	1.9707
6	2	0	53.2	1.9582	1.9582
2	2	3	65.2	1.8028	1.8026
3	2	3	16.5	1.7273	1.7277
6	2	2	13.5	1.6688	1.6684

Table 11.5: Anisotropic thermal displacement parameters $U_{ij} \times 10^4$ / pm^2 for Mn_2GeSe_4

Atom	U_{11}	U_{22}	U_{33}	U_{23}	U_{13}	U_{12}
Mn1	0.0111(2)	0.0066(2)	0.0076(2)	-0.0036(2)	-0.0009(2)	-0.0032(2)
Mn2	0.0061(2)	0.0100(2)	0.0072(2)	0	0.0003(2)	0
Ge	0.0034(1)	0.0035(1)	0.0006(1)	0	0.0001(1)	0
Se1	0.0052(1)	0.0059(1)	0.0001(1)	0	-0.0001(1)	0
Se2	0.0018(1)	0.0065(1)	0.0038(1)	0	0.0008(1)	0
Se3	0.0056(1)	0.0031(1)	0.0032(1)	0.00075(8)	0.00033(7)	0.00217(7)

The anisotropic displacement factor is defined as: exp $\{-2\pi^2[U_{11}(ha^*)^2 + ... + 2U_{12}hka^*b^*]\}$.

11.2 Data for Cr$_2$Ge$_2$Se$_6$

Table 11.6: List of the observed reflections for Cr$_2$Ge$_2$Se$_6$ (indexed hexagonal. see 5.3)

h	k	l	Int. / %	d$_{obs}$ / Å	d$_{calc}$ / Å
0	0	3	35.0	6.4803	6.4738
1	0	1	0.6	5.2354	52473
0	0	6	68.0	3.2379	3.2369
1	1	3	100.0	2.8306	2.8300
2	0	1	6.3	2.6992	2.6986
2	0	2	1.9	2.6256	2.6237
1	0	7	1.2	2.4732	2.4725
1	1	6	18.3	2.2562	2.2562
2	0	5	2.5	2.2298	2.2308
2	1	1	2.5	2.0485	2.0484
2	1	2	2.4	2.0152	2.0151
0	0	10	2.1	1.9431	1.9421
2	1	4	1.1	1.8957	1.8963
3	0	0	46.8	1.8165	1.8167
1	1	9	30.4	1.7794	1.7796
3	0	3	4.7	1.7490	1.7491
1	0	10	1.6	1.6526	1.6527
0	0	12	15.5	1.6181	1.6184
3	0	6	15.5	1.5840	1.5842
2	1	8	1.1	1.5714	1.5707
1	1	12	2.2	1.4390	1.4385
2	2	6	2.9	1.4142	1.4143
2	2	9	3.8	1.2707	1.2707
3	2	1	2.9	1.2473	1.2472
3	0	12	4.6	1.2079	1.2078
1	1	15	4.0	1.1967	1.1967
3	2	5	2.3	1.1897	1.1896
4	1	3	5.7	1.1693	1.1692
3	2	7	2.1	1.1390	1.1394
4	1	6	2.5	1.1159	1.1158

Table 11.7: List of the observed reflections for $Cr_2Ge_2Se_6$ at temperature 400°C (indexed hexagonal. see 5.3)

h	k	l	Int. / %	d_{obs} / Å	d_{calc} / Å
0	0	3	93.0	6.4929	6.4949
0	0	6	100.0	3.2488	3.2475
1	1	3	94.0	2.8352	2.8361
2	0	1	21.9	2.7037	2.7038
1	1	6	27.6	2.2627	2.2620
3	0	0	37.1	1.8196	1.8201
1	1	9	30.0	1.7847	1.7847
3	0	5	25.5	1.6496	1.6491
0	0	12	25.4	1.6234	1.6237
2	0	10	23.0	1.5860	1.586

Table 11.8: List of the observed reflections for $Cr_2Ge_2Se_6$ at temperature 500°C (indexed hexagonal. see 5.3)

h	k	l	Int. / %	d_{obs} / Å	d_{calc} / Å
0	0	3	34.8	6.5282	6.5265
0	0	6	51.5	3.2623	3.2632
1	1	3	100.0	2.8435	2.8433
2	0	1	10.5	2.7096	2.7093
1	1	6	18.1	2.2695	2.2696
2	1	1	6.0	2.0563	2.0565
2	1	2	6.1	2.0236	2.0233
2	0	8	36.8	1.8241	1.8240
1	1	9	19.1	1.7916	1.7917
3	0	3	7.7	1.7563	1.7565
0	0	12	8.8	1.6318	1.6316
2	0	10	10.9	1.5922	1.5922

11.3 Data for Fe$_3$GeTe$_2$

Table 11.9: List of the observed reflections for Fe$_3$GeTe$_2$ (indexed hexagonal. see 6.2.2)

h	k	l	Int. / %	d_{obs} / Å	d_{calc} / Å
0	0	2	33.4	8.1729	8.1652
0	0	4	19.4	4.0837	4.0826
1	0	0	23.6	3.4781	3.4779
1	0	1	44.4	3.4020	3.4016
1	0	2	21.2	3.1996	3.1997
1	0	3	100.0	2.9309	2.9308
0	0	6	25.5	2.7215	2.7217
1	0	6	56.7	2.1432	2.1434
1	1	0	95.0	2.0080	2.0079
1	0	7	21.0	1.9373	1.9374
1	1	4	17.6	1.8015	1.8018
1	0	8	18.2	1.7603	1.7605
2	0	1	18.8	1.7288	1.7292
2	0	3	29.2	1.6565	1.6565
1	1	6	27.0	1.6156	1.6158
1	0	9	23.5	1.6088	1.6087
2	0	6	25.6	1.4654	1.4654
2	0	7	18.1	1.3942	1.3942
0	0	12	18.5	1.3608	1.3609
2	1	3	23.9	1.2778	1.2778
2	0	9	19.0	1.2555	1.2555
2	1	6	23.7	1.1836	1.1837
3	0	0	22.9	1.1593	1.1593
2	1	7	18.3	1.1454	1.1452
1	1	12	21.8	1.1266	1.1265

Table 11.10: Anisotropic thermal displacement parameters $U_{ij} \times 10^4$ / pm^2 for Fe_3GeTe_2

Atom	U_{11}	U_{22}	U_{33}	U_{23}	U_{13}	U_{12}
Fe1	0.009(1)	0.009(1)	0.008(2)	0	0	0.0044(6)
Fe2	0.008(2)	0.008(2)	0.007(2)	0	0	0.0041(9)
Ge	0.025(2)	0.025(2)	0.013(2)	0	0	0.0124(8)
Te	0.0105(7)	0.0105(7)	0.0078(8)	0	0	0.0052(4)

The anisotropic displacement factor is defined as: $\exp\{-2\pi^2[U_{11}(ha^*)^2 + \ldots + 2U_{12}hka^*b^*]\}$.

11.4 Data for Ni₃GeTe₂

Table 11.11: List of the observed reflections for Ni$_3$GeTe$_2$ (indexed hexagonal. see 6.3.2)

h	k	l	Int. / %	d_{obs} / Å	d_{calc} / Å
0	0	2	10.4	8.0210	8.0172
0	0	4	5.5	4.0090	4.0086
1	0	0	6.3	3.3767	3.3766
1	0	1	24.7	3.3041	3.3042
1	0	2	5.5	3.1119	3.1119
1	0	3	100.0	2.8548	2.8547
0	0	6	12.6	2.6725	2.6724
1	0	4	1.6	2.5821	2.5825
1	0	5	3.1	2.3252	2.3253
1	0	6	57.6	2.0953	2.0955
1	1	0	66.3	1.9494	1.9495
1	0	7	8.4	1.8955	1.8956
1	1	4	3.7	1.7532	1.7532
1	0	8	2.0	1.7235	1.7235
2	0	1	3.5	1.6790	1.6790
2	0	2	1.2	1.6521	1.6521
2	0	3	15.8	1.6099	1.6099
1	1	6	23.9	1.5753	1.5750
1	0	10	1.5	1.4484	1.4484
2	0	6	13.1	1.4273	1.4273
2	0	7	2.4	1.3590	1.3591
0	0	12	4.0	1.3362	1.3362
2	1	1	2.7	1.2721	1.2722
2	1	3	10.8	1.2413	1.2413
2	0	9	4.7	1.2255	1.2255
2	1	5	1.0	1.1859	1.1858
1	0	13	2.0	1.1586	1.1585
2	1	6	10.4	1.1517	1.1517
3	0	0	6.3	1.1255	1.1255
1	1	12	9.1	1.1022	1.1022

Table 11.12: List of the observed reflections for Ni_3GeTe_2 at temperature 400°C (indexed hexagonal. see 6.3.2)

h	k	l	Int. / %	d_{obs} / Å	d_{calc} / Å
0	0	2	58.2	8.0594	8.0591
0	0	4	62.9	4.0311	4.0296
1	0	1	47.0	3.3276	3.3281
1	0	3	100.0	2.8737	2.8739
0	0	6	61.3	2.6864	2.6864
1	0	6	81.6	2.1080	2.1082
1	1	0	41.4	1.9639	1.9638
1	0	7	22.3	1.9065	1.9068
2	0	3	20.2	1.6215	1.6214
1	0	9	41.5	1.5848	1.5847

Table 11.13: List of the observed reflections for Ni_3GeTe_2 at temperature 600°C (indexed hexagonal. see 6.3.2)

h	k	l	Int. / %	d_{obs} / Å	d_{calc} / Å
0	0	2	54.5	8.0894	8.0877
0	0	4	58.4	4.0447	4.0438
1	0	1	42.7	3.3378	3.3383
1	0	3	100.0	2.8828	2.8831
0	0	6	56.0	2.6960	2.6959
1	0	6	78.0	2.1152	2.1152
1	1	0	45.4	1.9697	1.9698
1	0	7	19.9	1.9130	1.9132
2	0	3	20.1	1.6266	1.6264
1	0	9	37.7	1.5901	1.5901

Table 11.14: List of the observed reflections for Ni_3GeTe_2 at temperature 800°C (indexed hexagonal. see 6.3.2)

h	k	l	Int. / %	d_{obs} / Å	d_{calc} / Å
0	0	2	71.4	8.1467	8.1295
0	0	4	81.1	4.0669	4.0647
1	0	1	54.1	3.3466	3.3493
1	0	3	100.0	2.8921	2.8939
0	0	6	73.2	2.7105	2.7098
1	0	6	84.6	2.1238	2.1246
1	1	0	36.6	1.9761	1.9761
1	0	7	25.0	1.9214	1.9220
2	0	3	23.5	1.6325	1.6319
1	0	9	43.3	1.5970	1.5977

Table 11.15: Anisotropic thermal displacement parameters $U_{ij} \times 10^4$ / pm^2 for Ni_3GeTe_2

Atom	U_{11}	U_{22}	U_{33}	U_{23}	U_{13}	U_{12}
Ni1	0.0094(4)	0.0094(4)	0.0130(6)	0	0	0.0047(2)
Ni2	0.008387)	0.0083(7)	0.014(1)	0	0	0.0041(3)
Ni3	0.027(2)	0.027(2)	0.018(3)	0	0	0.014(1)
Ge	0.0255(6)	0.02558(6)	0.0147(8)	0	0	0.0127(3)
Te	0.0069(2)	0.0069(2)	0.0116(3)	0	0	0.00346(9)

The anisotropic displacement factor is defined as: exp $\{-2\pi^2[U_{11}(ha^*)^2 + ... + 2U_{12}hka^*b^*]\}$.